A Practical Evaluation of the Multi-Scale CLEAN Deconvolution Algorithm for Interferometric Radio Measurements

Joshua William Rich

A thesis submitted for the degree of

Doctor of Philosophy

of The Australian National University

THE AUSTRALIAN NATIONAL UNIVERSITY

Research School of Astronomy and Astrophysics

The Australian National University

Canberra ACT 0200

Australia

October 2008

Dedicated to my family, for endless, unquestioning support and music, for getting me through.

Disclaimer

I hereby declare that the work in this thesis is that of the candidate alone, except where indicated below or in the text of the thesis.

The data used within this thesis comes from The H$_I$ Nearby Galaxy Survey (Walter et al., 2008).

Chapter 2 is in part a paper (in submission as of the publication date of this thesis) in the Astronomical Journal (Rich, J. W., de Blok, W. J. G., Cornwell, T. J. , Brinks, E., Walter, F., Bagetakos, I. & Kennicutt, R. C. Jr.). The majority of the work is that of the candidate, with Section 2.2.8 and the figures therein are mostly the work of W. J. G. de Blok.

Chapter 3 contains an new analysis of hole catalogs for the three galaxies NGC 2403, Holmberg II and IC 2574, created by the candidate, combined with existing hole catalogs for other galaxies published by other researchers. The galaxies and references are M31 (Brinks & Bajaja, 1986), M33 (Deul & den Hartog, 1990), M81 (Bagetakos, 2006) and NGC 6946 (Boomsma, 2007). The double blind test discussed in Section 3.3 was conducted with the help of Ioannis Bagetakos (Center for Astrophysics Research, University of Hertfordshire).

Joshua Rich

13th April 2009

i

Acknowledgments

First and foremost, many thanks go to my supervisor, Dr. Erwin de Blok, who graciously allowed me to complete my PhD under his supervision. From knowing nothing at all about radio astronomy to getting, dare I say, a solid grasp of many aspects of the field, was mostly due to his patience (often in explaining concepts multiple times), understanding (knowing that I did not know what I was doing and would need it explained again) and compassion (in not getting angry after having to explain the same thing several times). I have come out of the entire process with a greater appreciation of all aspects of radio astronomy, a keen interest in the future direction of the field, and knowledge of fine European beers.

I gratefully acknowledge the financial support provided by the Australian National University PhD Graduate Scholarship, and the Research School of Astronomy and Astrophysics PhD top-up scholarship. Additionally, I'd like to acknowledge the travel funding provided by the research school for the various trips to national and overseas institutions and conferences I was able to attend. Further thanks must be made to Peter Young, Bill Roberts, Kim Sebo and the rest of the computing section at Mount Stromlo for providing me with not just employment, but valuable hand-on experience with all aspects of computing and IT infrastructure/administration. I came to Mount Stromlo with very little knowledge outside of the proprietary world of Microsoft and will leave with enough knowledge to continue to get me in trouble with computers for many years to come. I'd like to thank Professor Brian Schmidt for both being my Honours supervisor, presenting an interesting and challenging Honours project as well as providing me with additional casual employment. Developing software for use in the Skymapper telescope data reduction pipeline was a great experience and I know the knowledge I have gained through this work will be very useful in my future career path.

I extend a big thank you to the students, past and present of the Research School of Astronomy and Astrophysics who provided excellent company and entertainment over the years from 2003 to 2008 during Honours and my PhD. Although only fifteen minutes away from main campus, Mount Stromlo is a world away from campus life and the students at Mount Stromlo make it such a special place to be. There are a few who deserve a special thank-you, in no particular order. José Robles, for being the best office-mate and creating a world full of constant amusement. Ewan Cameron, for hipster culture input and assessment. Leith Godfrey for the few jam sessions we managed to fit in. Nic Bonne for honest opinions and being a good friend.

There are two other people who were an integral part of getting me through my PhD. To Laura, for her empowering attitudes and opinions which guided me through many difficult decisions I could not make on my own, welcoming

ii

me with open arms into her life and creating happiness that never faltered. To Sayuri, whose powers as a muse are immeasurable, and for providing stability, warmth and companionship to the end.

1. `http://leda.univ-lyon1.fr`

2. `http://pdl.perl.org`

3. `http://plplot.sourceforge.net/`

4. `http://www.inkscape.org`

5. `http://www.gust.org.pl/projects/e-foundry/tex-gyre`

6. `http://tug.ctan.org/tex-archive/fonts/pxfonts`

Abstract

In the first part of this thesis, a comparison of the practical performance of the Multi-Scale CLEAN algorithm is presented. The data used in the comparisons is taken from The H I Nearby Galaxy Survey (THINGS). The implementation of Multi-Scale CLEAN in the CASA software package is used. It is compared against the (similar in design) Multi-Resolution CLEAN algorithm and classical CLEAN with and without windows applied, that are implemented in the AIPS software package. The results of this comparison show that several of the well-known characteristics and issues of using classical CLEAN are significantly lessened (or eliminated completely) when using Multi-Scale CLEAN. Importantly, Multi-Scale CLEAN reduces significantly the effects of the clean 'bowl' caused by missing short-spacings, and the 'pedestal' of low-level 'un-cleaned flux (which affects flux scales and resolution). Multi-Scale CLEAN can clean down to the noise level without the divergence suffered by classical CLEAN.

The second part of the thesis presents the process of generating catalogues of H I holes in the inter-stellar medium of the nearby galaxies NGC 2403, Holmberg II and IC 2574. Data from the THINGS study, processed with MSCLEAN has been used, providing high-quality, high-contrast data which greatly assists in finding and measuring H I holes and their properties. A comparative study of the hole catalogues of the three galaxies is made, including hole catalogues made for the galaxies M31, M33, M81 and NGC 6946 by other researchers, where the data is of a similar resolution and the catalogues have been constructed in a similar manner to those made in this thesis. The H I holes are shown to dominate the ISM of all galaxies studied and the measured properties of the H I holes show a strong link to both the Hubble type of the galaxy and the known dynamical properties of the H I disk.

CONTENTS

LIST OF FIGURES

LIST OF TABLES

CHAPTER 1

INTRODUCTION

Astronomy is a science which cannot be done without good quality observations. It is therefore imperative that the process of taking observations is well understood, and that the process of transforming the raw observations into a usable data-set from which astronomical results can be measured is performed with care and clarity. This is a crucial step in the astronomical scientific process, and the processes to use vary with the instrument used to take the observations.

Mostly, astronomical observations extract information about a measured object from the electromagnetic radiation it emits. It can be visualised to form an image (*imaging*), the strength of it measured (*photometry*), or the distribution over the wavelength range in which it is detected can be examined (*spectroscopy*), among other aspects of study. In the optical domain, where the energy of the electromagnetic radiation is high enough to detect individual photons, scientific measurements in these areas can be done directly from the observations (with some post-processing). Hence optical astronomy is a direct imaging technique. As an example, simple imaging in the optical domain with a single telescope is usually performed by filtering and focusing a certain band of electromagnetic radiation onto a CCD (or photographic plate *etc.*) to form a direct image of the object being examined.

In the radio domain, the energy of the electromagnetic radiation is much lower, the individual photons cannot be easily measured and other properties of the electromagnetic radiation must be used to infer the amount of radiation received. Direct imaging is much harder for radio astronomical imaging than it is for optical astronomical imaging. It is still possible using, for example, a bolometer, but at a significant loss of sensitivity. Radio astronomers therefore generally rely on indirect imaging techniques to gain equivalent sensitivities to their optical counterparts. An example of indirect imaging in radio astronomy would be a basic radio instrument, an antenna, which measures the electromagnetic field

of incoming radiation through induction as it passes through conductors in the antenna.

This thesis deals exclusively in the domain of radio astronomy. We are primarily interested in radio *imaging*, forming a picture of a distant object of interest in radio wavelengths. The formation of an image can be thought of as a combination of two steps (Shore, 2002). First, the emission from the source or object is collected by a telescope or receiver. Second, the emission is transferred and processed through the telescope and instrument apparatus to form the final image. This image is not a *true image* of the source. Besides sources of noise both physical (*e.g.,* atmosphere) and instrumental, the instrument itself also affects the transfer of information from the object to the image taken. It is best then to think of an astronomical image used for science as a *model image* of the object which, given the variable constraints, presents an optimum representation of the object.

For a radio interferometer, of which the data for this thesis is sourced from, the process is a little more complicated. Essentially, astronomical interferometric radio imaging is a Fourier transform. The observations are a convolution of the true image (plus the noise) with the instrumental response of the telescope (the Point Spread Function, PSF). Put simply, the observations are a blurring of the true image (Briggs, 1995a). The noise, the instrument response and the observations are all known or can be calculated. The true image is not known and cannot be calculated, only a model of it can be made from the other three components. Imaging is then a process of constructing a model image of the object by reducing the effect of the instrumental response on the observations while minimising the noise.

Deconvolution is the technique which is applied to this problem. As the name suggests, deconvolution attempts to separate the PSF from the true image (*i.e.,* de-convolve the two). In radio astronomy, well established deconvolution algorithms are used for this purpose. The most widely used, the CLEAN algorithm (Högbom, 1974), attempts to construct a model of the true image via an iterative procedure. It assumes the observations consist of an empty sky filled with point sources that make up the object (or objects) of interest. It searches the observations for the location of these point sources, subtracting them out of the observational data until eventually just the noise remains, after which it reconstructs a model image of the object using an ideal PSF for the instrument, the subtracted component strengths and the noise left after the iterative procedure.

Deconvolution is particularly important for radio interferometers, where the PSF can be extremely complicated. For a single dish radio telescope, to first order, the calculation of the size of the PSF depends on the diameter of the dish D and the wavelength λ used through λ/D. For radio interferometers, the size of the PSF to first order depends on the length of the longest baseline d (the spacing between two dishes in the array) through λ/d. The precise shape of the PSF and the surface brightness sensitivity depend, however, on the configuration of the array

and its filling factor (*i.e.*, where and how the individual dishes are positioned). The incompletely sampled size-scale distribution inherent to an instrument like a radio interferometer leads to a complicated PSF and consequently to an image with many artifacts that need to be compensated for (we refer the reader to Thompson et al., 2001 for more details).

The CLEAN algorithm does its best to compensate for such issues, but it does have its limitations. Particularly, when imaging extended objects such as galaxies (*i.e.*, the data used in this thesis), the simple approach of building a complex object up from many point sources can lead to several issues, most notably a speed problem as the object is built from many point source components, among other issues that will be discussed in the next chapter. As such, newer algorithms have been developed that attempt to overcome many of its short-comings. One promising algorithm, multi-scale CLEAN, is based on the classical CLEAN algorithm but is adapted to be *scale-sensitive*. That is, instead of searching for point sources, it searches for emission of different sizes (or scales), subtracting out a 'blob' of emission in each iteration. Its operation is therefore similar to classical CLEAN, but as will be shown within this thesis, it appears to not suffer as much as the latter when dealing with imaging of extended sources from radio interferometers.

The big advantage of these instruments, however, is the huge gain in resolution. Size does matter in radio astronomy. The diffraction limit of a telescope defines the angular resolution you can achieve and the diffraction limit is proportional to the diameter of the telescope. The bigger the collecting area of the dish, the higher the resolution you can achieve in your observations. Building an array of many smaller dishes is also much more cost effective and simpler in engineering effort than building the gigantic dishes needed to achieve the same resolution. Combined with the added contrast accomplished through the application of a clever deconvolution technique such as multi-scale CLEAN, the finest structure present in the observations will, as a result, be much more visible in the data.

In particular, radio interferometer observations of neutral hydrogen (H$_I$) at 21 cm benefit from increased contrast and/or resolution. The Inter-Stellar Medium (ISM) largely is H$_I$, and better contrast, resolution or both allows the resolving of the fine-scale structure that H$_I$ traces throughout it. Optical studies of the ISM are limited by the absorption of visible light from intervening clouds and gas, which can be high, leading to weak emission lines and thus restricting the range of observations in this domain. H$_I$ on the other hand is optically thin despite its dominant abundance, resulting in emission lines from which many spatial properties of the H$_I$ distribution can be measured, leading to estimates of the dynamical effects that are occurring in the disk of a galaxy. And because it is the building block of objects such as stars and molecular clouds, many properties of these objects can be inferred from these simple measurements of H$_I$ in the ISM.

After hydrogen in its various forms (neutral, ionised, molecular), the next most abundant element in the ISM is helium, followed by other heavier elements and

finally dust and grain particles of complex molecules and cosmic rays (Spitzer, 1956). This component mix and structure is believed to be in part caused by large-scale star-formation throughout the ISM, leading it to be called the 'violent inter-stellar medium' (McCray & Snow, 1979). Strong stellar winds from massive star clusters as well as supernova (and possibly gamma-ray burst) explosions define the structure, heat the ambient gas and distribute material throughout the ISM. This results in a complex environment of tunnels, networks and cavities of under-densities (*e.g.*, Brand & Zealey, 1975; Heiles, 1979; McCray & Snow, 1979; Brinks & Bajaja, 1986; Deul & den Hartog, 1990; Kim et al., 1999; Stanimirovic et al., 1999; Walter & Brinks, 1999). The size of these objects ranges from the resolution of the data (a few hundred parsecs) to sizes of a few scale heights of the H I disk (a few kiloparsecs). They blanket and permeate the disk, making it look much like swiss-cheese.

These so-called 'holes' are therefore important locations within the ISM. Not only is there an apparent intimate link between star-formation and hole-formation, but these objects literally define the structure of the ISM and so may be the key to studying its dynamics. The small sizes of these holes demand the best resolution and contrast possible from the observations.

This thesis has two main goals. The first goal is to explore a new and promising deconvolution algorithm, multi-scale CLEAN, that may contribute to improving the state of imaging techniques and astronomical software processing, particularly in light of the next-generation radio astronomical facilities which will be producing a huge amount of data that current techniques and software may not adequately handle. The second goal, using high-resolution data taken with the Very Large Array, is to probe the fine-scale structure in the ISM, making a first step to understanding the events that lead to star-formation in nearby galaxies.

1.1. Data Sources

The H I data used in this thesis comes from The HI Nearby Galaxy Survey (THINGS; Walter et al., 2008)[1]. THINGS is a sample of 34 nearby galaxies (within 15 Mpc) observed with the National Radio Astronomy Observatory (NRAO) Very Large Array (VLA) in its B, C and D array configurations. The observations provide a high resolution ($\sim 6''$, $\sim 2.6 - 5$ km s^{-1}) data-set for H I studies. Integrated intensity maps of all 34 galaxies are shown in Figures 1.1 and 1.2. The galaxies analysed in this thesis which are in the THINGS sample are marked with an asterisk. Chapters 2 and 3 make use of amplitude/phase calibrated, flagged and continuum subtracted *uv* data-sets from this survey. More details and a summary of the observations can be found in Walter et al. (2008).

(a) DDO 154   **(b)** DDO 53   **(c)** Holmberg I   **(d)** Holmberg II*

(e) IC 2574*   **(f)** M81 DwA   **(g)** M81 DwB   **(h)** NGC 1569

(i) NGC 2366   **(j)** NGC 2403*   **(k)** NGC 2841   **(l)** NGC 2903

(m) NGC 2976   **(n)** M81*   **(o)** NGC 3077   **(p)** NGC 3184

(q) NGC 3198   **(r)** NGC 3351   **(s)** NGC 3521   **(t)** NGC 3621
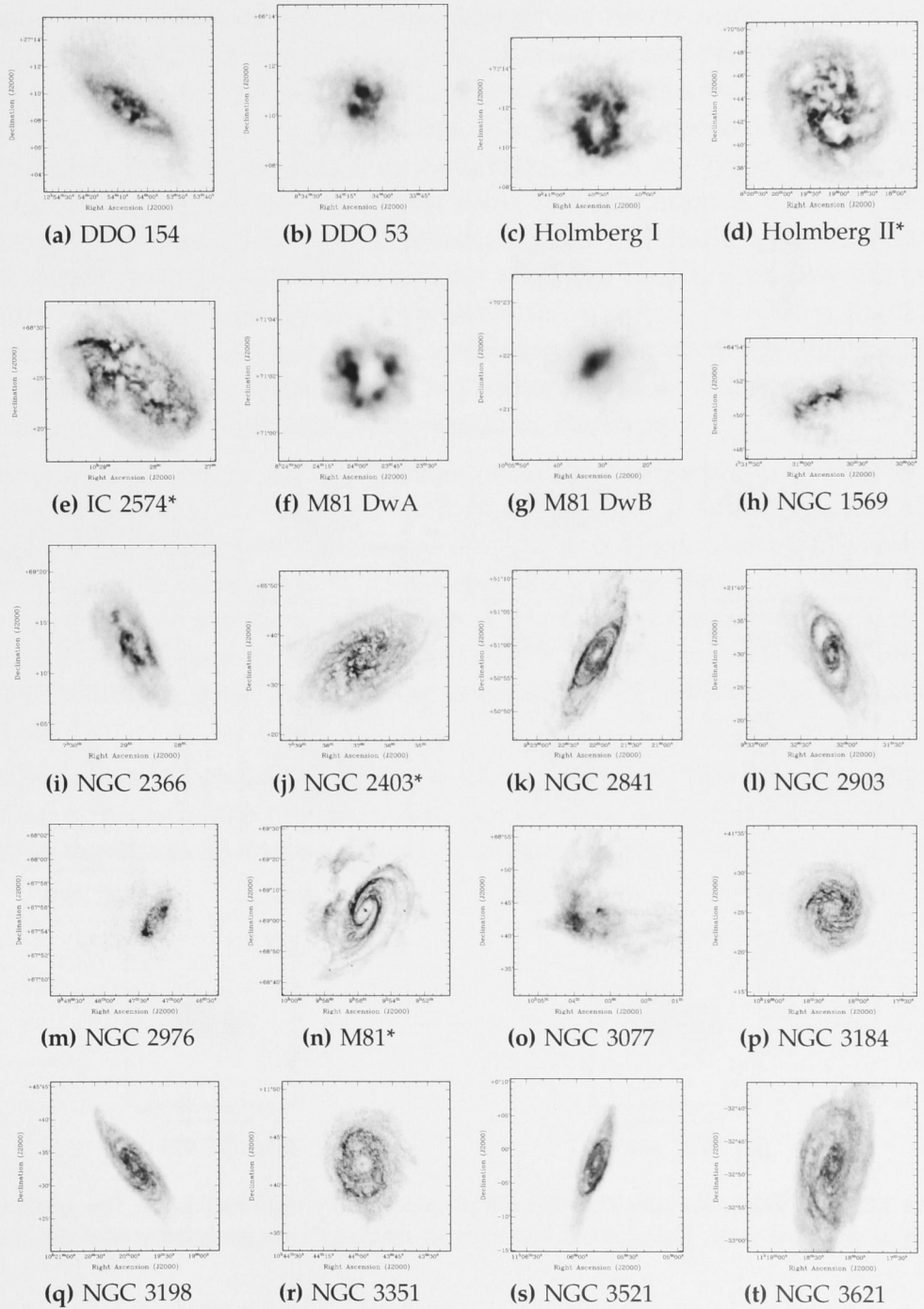
Figure 1.1   The galaxies in the THINGS sample, ordered by right ascension (Walter et al., 2008). The galaxies are not to the same scale. Galaxies marked with an asterisk (*) are analysed within this thesis.

(a) NGC 3627   **(b)** NGC 4214   **(c)** NGC 4449   **(d)** NGC 4736

(e) NGC 4826   **(f)** NGC 5055   **(g)** NGC 5194   **(h)** NGC 5236

(i) NGC 5457*   **(j)** NGC 628   **(k)** NGC 6946*   **(l)** NGC 7331

(m) NGC 7793   **(n)** NGC 925
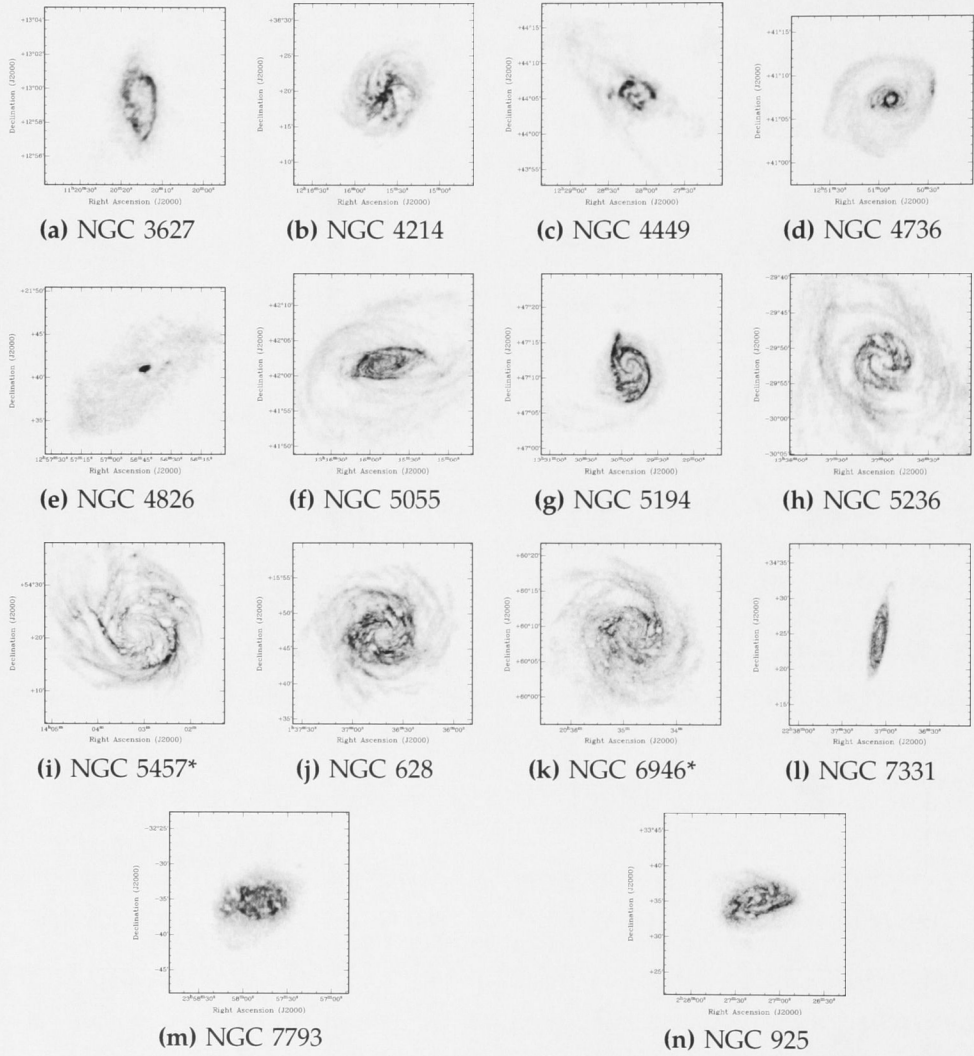
Figure 1.2   The galaxies in the THINGS sample, ordered by right ascension. The galaxies are not to the same scale. Galaxies marked with an asterisk (*) are analysed within this thesis.

1.2. Outline of the Thesis

Chapter 2 presents a detailed comparison of the newer multi-scale CLEAN deconvolution algorithm against the classical CLEAN deconvolution algorithm on a few galaxies from THINGS. There are few published articles that discuss in detail the multi-scale CLEAN algorithm. The analysis presented in Chapter 2 complements the detailed high-level explanation given in Cornwell (2008) with a practical comparison of the algorithms using real astronomical data. It attempts to demonstrate the limitations of classical CLEAN in handling data composed of extended sources such as galaxies by showing how the multi-scale CLEAN algorithm overcomes or outright eliminates these issues. As such, it highlights the issues that may be encountered by future radio facilities, whose imaging capabilities will produce high-volume, high-resolution data that current 'standard' deconvolution algorithms may have problems handling.

Chapter 3 then details an application of using multi-scale CLEAN for a real astronomy problem, holes in the H$_I$ disk of galaxies. A full discussion of the creation of such catalogues is presented along with a comparison across a number of galaxies with catalogued H$_I$ holes and spanning a range of Hubble types. The resulting hole catalogues should be of use to other researchers looking into the link between H$_I$ hole formation, H$_I$ disk dynamics and star-formation. The chapter discusses these links through comparison of holes across the galaxies studied.

A summary and conclusion of the work presented in this thesis is given in Chapter 4. A discussion of future work that could be carried out, using the work done in this thesis as a foundation, is also presented.

CHAPTER 2

MULTI-SCALE CLEAN VERSUS CLASSICAL CLEAN: A COMPARISON OF PERFORMANCE ON EXTENDED SOURCES

This chapter is mostly from a paper published in the Astronomical Journal, December 2008[2].

THE art of astronomical observations lies in reconstructing the highest fidelity representation of the sky, given the inherent limitations of the data, which are always to some degree affected by atmosphere, instrument, technique or telescope. Some kind of processing always needs to be applied to minimize these issues and produce the most accurate representation of the astronomical source of interest. This processing is particularly important for observations obtained with radio synthesis telescopes, *e.g.*, observations of the 21cm line of atomic hydrogen. Even though, in this domain, instrumental artifacts are generally small and the atmosphere is well-behaved, the noise and instrumental response (or Point Spread Function, PSF) are still a major problem in generating a true representation of a source. For radio interferometers, the full width at half maximum (FWHM) of the PSF to first order depends on the length of the longest baseline. The precise shape of the PSF and the surface brightness sensitivity depend, however, on the configuration of the array and its filling factor. The incompletely sampled size-scale distribution inherent to an unfilled aperture instrument leads to a complicated PSF and consequently to an image with significant artifacts (we refer the reader to Thompson et al., 2001 for more details).

Deconvolution is the technique of choice for attempting to remove these artifacts. It does so by interpolating and extrapolating the incompletely sampled *uv* plane,

thus attempting to correct for the effects of the complex PSF. Other factors that influence the observations, such as noise and atmospheric effects, cannot be corrected by deconvolution. Deconvolution can be thought of as a simple equation: $(F + G) * H = I$, where $(F + G) * H$ indicates the convolution of F plus G with H. F is the true image, G is the noise, H is the PSF and I represents the raw measurements or observations. Deconvolution is the process of solving for F, given G, H and I. A measure for the performance of any deconvolution algorithm thus lies in its effectiveness of reducing the effect of a PSF (H) on the image (F). Data that are not (or cannot be) recorded at the telescope, due to, for example, incomplete sampling of the uv-plane are not recovered through deconvolution, but have to be interpolated. This interpolation is at the heart of some of the complications with deconvolution described in this chapter.

The 'de-facto' standard of deconvolution algorithms for radio astronomy is the CLEAN algorithm (Högbom, 1974). This classical CLEAN is an iterative procedure. It assumes that the sky is only sparsely filled with a limited number of point sources superimposed on an otherwise empty background. It finds the location and strength of all these sources, and uses them to reconstruct a representation of the true image using an ideal PSF. Over the years several variants (*e.g.*, Schwab, 1984; Clark, 1980) have been proposed to overcome various limitations and nuances that are intrinsic to CLEAN (see also Schwarz, 1978; Brinks & Shane, 1984). However, there still remains a basic assumption that the sky is composed of point sources, which is adequate if the source being observed has limited extent. Extended structure is modeled by CLEAN as a large number of point sources and the iterative procedure becomes a time-consuming process involving a constantly increasing number of point sources. To partly compensate for this problem, CLEAN can be restricted to only work in regions where the source of interest is known to exist, through the use of CLEAN 'windows'. Such windows require prior knowledge of the source structure and extent, but are flexible and multiple windows can be used to bound a complicated source.

An obvious enhancement to CLEAN would be to make it more efficient at modeling extended structures. Many such 'scale-sensitive' algorithms have been proposed. These methods generally assume that the sky is not composed of only point-sources as CLEAN does, but of sources of many different sizes and scales. One of the first such methods, multi-resolution CLEAN, tackles the problem by smoothing and decimating the dirty image and PSF to emphasize the extended emission. The image resulting from cleaning this dirty image is then used as an initial model for cleaning the next higher resolution image, *etc.* (Wakker & Schwarz, 1988). Wavelet CLEAN uses the wavelet transform in the CLEAN process but basically operates in a similar manner to multi-resolution CLEAN (Starck et al., 1994). The more recently developed Adaptive Scale Pixel CLEAN uses scale sizes that can 'adapt' their size during processing (Bhatnagar & Cornwell, 2004). There is a wealth of literature explaining the inner workings of multi-resolution CLEAN and the other algorithms mentioned above in detail (see Bhatnagar & Cornwell, 2003;

Starck et al., 2002, in addition to the references above), including a considerable amount of modeling as well as some practical tests.

Multi-scale CLEAN (hereafter referred to as MSCLEAN) is a straight-forward extension of the classical CLEAN algorithm for handling extended sources (Cornwell, 2008). Just like the multi-resolution CLEAN defined by Wakker & Schwarz (1988), it works by assuming the sky is composed of emission at different spatial scales. However, whilst the Wakker & Schwarz multi-resolution CLEAN works on each scale sequentially, MSCLEAN works simultaneously on all scales that are being considered. This prevents potential errors made at a previous larger scale from being 'frozen in' and requiring many iterations at smaller scales to correct. MSCLEAN has been implemented in both CASA[3] (formerly AIPS++) and classical AIPS[4] (as part of the multi-resolution options of the IMAGR task). In this chapter, we compare the operation of MSCLEAN against classical CLEAN both with and without the use of CLEAN windows, using some real-world data and astronomical problems derived from high quality HI data obtained through the THINGS project. We refer to Cornwell (2008) for a more technical description of MSCLEAN, as well as a description of tests involving artificial data.

THINGS, The HI Nearby Galaxy Survey, consists of a sample of 34 nearby galaxies observed with the NRAO Very Large Array (VLA) B,C and D arrays (Walter et al., 2008). The high resolution ($\sim 6''$, ~ 5 km s^{-1}) achieved with THINGS pushes the VLA to the limits of its current performance for observations of a significant sample of galaxies. The THINGS observations, being combined multi-array data with a large range of spatial scales therefore present one of the most challenging data-sets with which to compare the efficiency of deconvolution algorithms. We emphasize that classical CLEAN works very well on the THINGS data sets, and that with a full knowledge of its intricacies excellent results can be achieved. However, CLEAN is not perfect, and our goal in this chapter is to describe some practical applications of the MSCLEAN algorithm. MSCLEAN seems to have fewer limitations than CLEAN does when it comes to handling data of extended sources. It is promising enough that it might point the way to an efficient exploration of the high-quality data, similar to the THINGS data set, that will be routinely produced by the next-generation radio and millimeter facilities such as ALMA[5], EVLA[6], LOFAR[7] and SKA[8]

This chapter begins with a brief description of the CLEAN and MSCLEAN algorithms in Section 2.1. In addition to summarizing the procedure each algorithm uses in Sections 2.1.1 and 2.1.2, the chapter discusses the limitations of the CLEAN algorithm and the advantages that MSCLEAN provides (Section 2.1.3). In Section 2.2, a detailed comparison of the performance of CLEAN and MSCLEAN on a sample of three galaxies from THINGS is presented. Section 2.3 then presents a practical comparison between MSCLEAN as implemented in CASA, the version implemented in AIPS and classical CLEAN as well as windowed-CLEAN. The chapter ends with a short summary of the key results of the tests and comparisons performed

(Section 2.4).

2.1. Deconvolution with CLEAN and MSCLEAN

Excellent detailed descriptions of the CLEAN algorithm can be found in Högbom (1974), Schwarz (1978) and Cornwell et al. (1999). For MSCLEAN, Cornwell (2008) contains a detailed description of this algorithm. For completeness, and to introduce some nomenclature, we briefly describe the classical CLEAN as well as the MSCLEAN procedure here.

Deconvolution algorithms attempt to create a model of the true 'sky brightness distribution' (the object) from the 'dirty map' (the observed image) using the 'dirty beam' (the observed PSF). This model is called the 'CLEAN map' (or 'restored map') and is created using the 'CLEAN beam', which represents an ideal PSF. It is typically a Gaussian function of the same FWHM as the central component of the dirty beam (Schwarz, 1978).

2.1.1. The CLEAN Procedure

The CLEAN algorithm is an iterative procedure operating on the dirty map. CLEAN can be described as follows:

1. Find the location of the maximum absolute brightness point source in the 'dirty map' and optionally within a user-defined window in the image.

2. Multiply the strength of this point source by a gain factor (usually 10%) to generate a 'CLEAN component' at this location.

3. Convolve the CLEAN component with the 'dirty beam', and subtract this from the dirty map, recording the position and strength of the CLEAN component subtracted.

4. Repeat the above three steps on the dirty map, until all emission is found, or a certain flux threshold is reached, or a number of iterations has been achieved.

After the procedure has stopped by meeting one of the conditions in Step 4, the result is a list of CLEAN components, and a residual image with all flux cleaned away to the specified conditions. The final image (the CLEAN map or restored image) is created by adding all of the CLEAN components convolved with the CLEAN beam onto the residual map. Adding the residual image left after the iterative subtraction procedure is in principle optional, but is usually always done in order to retain information on the noise and any remaining residual flux (Schwarz, 1978). We defer to Section 2.1.3 a discussion on the potential problem of combining cleaned and uncleaned data.

2.1.2. The Multi-Scale CLEAN Procedure

Multi-Scale CLEAN (in both its CASA and AIPS implementations) is a modification of the classical CLEAN algorithm. Instead of representing the sky as empty and containing a limited number of point sources as is done by CLEAN, MSCLEAN presumes that sources in the sky are actually extended structures of different scales (which can include point sources).

An important constraint is that the function used to define the shape of the scales has a finite extent, so that, for example, a CLEAN window can be applied. As such, a Gaussian function is not a good choice, unless some kind of truncating function is applied. Generally, a paraboloid with an appropriate tapering function is chosen, which becomes a delta-function in the limit of zero scale-size (Cornwell, 2008). By pre-computing the convolution of the dirty beam with each scale size, one can proceed with a parallel CLEAN-like procedure on a set of images generated for each of the scales. It is important to include a scale-size zero delta-function which enables proper fitting of point sources. The process is then as follows:

1. Convolve the dirty map with each scale size to create a set of convolved images.

2. Find the global peak among these images, *i.e.*, the scale that contains the maximum total flux and record the position, flux and scale size for the image in which this occurs.

3. Subtract the pre-computed scale (of the same size in which the peak was found) convolved by the dirty beam, multiplied by some gain factor, from all the images made in the first step.

4. Store the subtracted component and the scale size in a table.

5. Repeat the above steps on the current convolved images until all emission has been removed, a flux threshold is reached or an iteration limit has passed.

In other words, where CLEAN operates on a single residual image, MSCLEAN keeps a set of residual images, one image per scale size defined. The peak subtraction is performed on all of these images, but only the one subtracted component and its scale size are stored in the CLEAN component table. The restoration is then an addition of the appropriately scaled, positioned and convolved components subtracted at each iteration on top of the final residual image. We refer to Cornwell (2008) for a technical description of the algorithm.

2.1.3. The Limitations of CLEAN and MSCLEAN's Advantages

For purely practical reasons, any implementation of CLEAN will have an iteration limit built in (*e.g.*, Cornwell et al., 1999). The design of the algorithm is to iteratively find and remove the strongest point sources; the number of iterations is therefore one of the factors that defines how deep CLEAN will go in terms of the flux level. Eventually, noise peaks will start to be cleaned away as well, as the algorithm cannot distinguish them from faint real signals. The number of components will therefore start to increase dramatically. This can easily spiral out of control as CLEAN approaches the noise limit and leads to a diverging total flux (Cornwell et al., 1999). All of this illustrates the necessity of imposing a hard limit on the number of iterations, either directly or through a flux threshold.

However, despite its usefulness in placing a practical constraint on CLEAN, the iteration limit is not without its disadvantages. It is a compromise between cleaning as deeply as possible and avoiding most of the noise. As mentioned in the introduction, this is a particularly important point for extended sources (such as the THINGS galaxies), which CLEAN will attempt to model with a large number of point sources. In contrast, practical results show that MSCLEAN removes large-scale structure before finer details (Cornwell, 2008, and see Section 2.2.2). This provides a useful advantage over CLEAN in most cases: the prior removal of underlying extended emission will reduce the strength of small-scale emission peaks that will remain. This means that when MSCLEAN begins to remove the small-scale structure, it will require less iterations to do so. The lack of this scale-size advantage in classical CLEAN means it is required to slowly cut down sources. MSCLEAN, with its convergence from large to small scales, does not spend its final cycles slowly removing a large amount of extended emission in small increments.

Classical CLEAN must also use low loop gains (typically 10% or less) to improve the reconstruction of extended emission. Using a high loop gain would be more efficient, especially for extended sources, but can easily lead to instabilities (Cornwell et al., 1999). Furthermore the gain is one parameter of CLEAN that has a large effect on the final CLEAN solution (Schwarz, 1978; Tan, 1986). MSCLEAN is much less dependent on the gain and is able to use much higher values (Cornwell, 2008). This means that each MSCLEAN scale has the ability to remove a much larger portion of the flux in each individual iteration, again reducing the overall number of iterations required compared to CLEAN.

The problem whereby CLEAN poorly models extended emission is further compounded by the interpolation for the missing spacing information. Generally, in interferometric observations, the extremely short or zero spacings, which measure the largest structure on the sky, are missing. In other words, the innermost part of the *uv*-plane is not (well) sampled. In these cases the total flux of an *extended* source (*i.e.*, containing structures at scales larger than sampled by the shortest baseline) cannot be recovered. Together with the strong side-lobes present in

the dirty beam and the pedestal of uncleaned flux, this leads to a CLEAN 'bowl': the source sits in a region with a negative background. This CLEAN bowl will cause skewed noise and flux estimates. The higher efficiency of MSCLEAN in removing extended structures means it can approach the noise limit more easily than CLEAN, with the result that the presence of the CLEAN bowl is also greatly reduced yielding a noise-like residual background.

A subtle, but important limitation of CLEAN lies in the reconstruction of the CLEAN or restored image from the final residual image and the CLEAN components. The restored image is an addition of two separate flux scales, a residual map with the units Jy per dirty beam and a CLEAN component map with units Jy per clean beam. As the extent of the dirty beam is always larger than that of the best-fitting CLEAN beam, using the CLEAN beam to determine the flux of the residuals will always lead to an overestimate of this flux. As such a correction factor needs to be applied to determine the flux in regions with signal (Jörsäter & van Moorsel, 1995). This is described in Walter et al. (2008) for the THINGS galaxies. This scaling of the residuals, and therefore the noise, yields correct fluxes in areas with signal, however the noise properties are no longer representative. Residual-scaled cubes should thus be only used to measure fluxes in areas with significant signal. Any other applications which critically depend on noise properties (such as profile fitting) should use the unscaled cubes (see Walter et al., 2008, for a detailed discussion).

In order to illustrate the limitations of CLEAN and potential advantages that MSCLEAN could provide, the remainder of this chapter is devoted to a practical comparison between CLEAN and MSCLEAN (Section 2.2). We also compare the implementation of MSCLEAN in the CASA and AIPS software packages to classical CLEAN with the use of CLEAN windows (Section 2.3). We use a small sample of galaxies from THINGS to compare the results.

2.2. A Detailed CLEAN and MSCLEAN Comparison

2.2.1. Data Processing

We chose three galaxies from the THINGS survey to use for our comparison of MSCLEAN and CLEAN. These galaxies are NGC 2403, Holmberg II and IC 2574 and they cover a range of H I masses and morphologies (Walter et al., 2008). Each galaxy was observed with the VLA in B, C and D configurations. This study uses the calibrated and combined *uv* data-set from all arrays for each galaxy. More details on the observations and generation of the *uv* data-sets can be found in Walter et al. (2008). The MSCLEAN implementation in the CASA software package and the CLEAN implementation in the AIPS software package (based on the Clark CLEAN, see Clark, 1980) were used on the *uv* data-set for this comparison. For

each galaxy, two data cubes were generated with two different weightings; a 'natural' weighting and a 'robust' weighting with a robustness parameter of 0.5 (Briggs, 1995b). These weightings were the same as used in the creation of the original THINGS data cubes.

The data cubes were created with the same spatial and velocity pixel sizes as the original THINGS cubes (for details see Walter et al., 2008). The cubes were then 'MSCLEAN-ed' down to 2.5σ which was also the flux threshold used in THINGS. As mentioned in Section 2.1.3, MSCLEAN can usually use much higher gain factors than classical CLEAN. In this study, the MSCLEAN gain factor was set at 0.7 for all three galaxies (see Cornwell, 2008, for a discussion of the MSCLEAN loop gain). No CLEAN windows were used. A maximum number of MSCLEAN iterations of 1200 (NGC 2403), 700 (Holmberg II) and 1000 (IC 2574) were chosen for each galaxy per channel. In all cases the flux limit was reached well before the iteration limit. Unless mentioned otherwise below, the cubes were also corrected for primary beam attenuation using the LINMOS task of the MIRIAD[9] software package. Residual cubes were also created for the CLEAN and MSCLEAN data.

2.2.2. MSCLEAN Scale Choice

As discussed briefly in Section 2.1.2, CASA (and AIPS++) use paraboloids for the shape of the scale components. Extensive experimentation shows that the results did not depend significantly on the number of scales chosen nor their distribution. The most important choice is that of the largest size in the distribution. We found that optimum results were obtained when this was chosen to correspond roughly to the size of the largest coherent structures visible in individual channel maps. This choice does not have to be exact. We chose a total of six scales distributed where each scale is three times larger than the preceding scale. Again, this choice was not critical, but we found that this distribution was more efficient (in terms of number of iterations required) than a linear distribution. The largest scale for each galaxy was 130" (NGC 2403), 270" (Holmberg II) and 160" (IC 2574).

For comparison, Figure 2.1 shows how the range of scales chosen and structure size for a single channel map are related in the galaxy NGC 2403. It can be seen that for the largest scale size, the largest coherent structure visible in the channel map fits within its diameter. Choosing an even larger scale would have no effect, as the largest structure is already optimally contained within the scale distribution shown, and MSCLEAN would simply not choose these even larger scales. Choosing a smaller, largest scale would simply increase the number of iterations.

Figure 2.2 shows the choice of scales the algorithm made with iteration number for a single velocity channel of Holmberg II. In other words, the figure shows the MSCLEAN scale component used as the algorithm progressed to lower flux levels. A similar trend is observed across all channels of all three galaxies. It shows
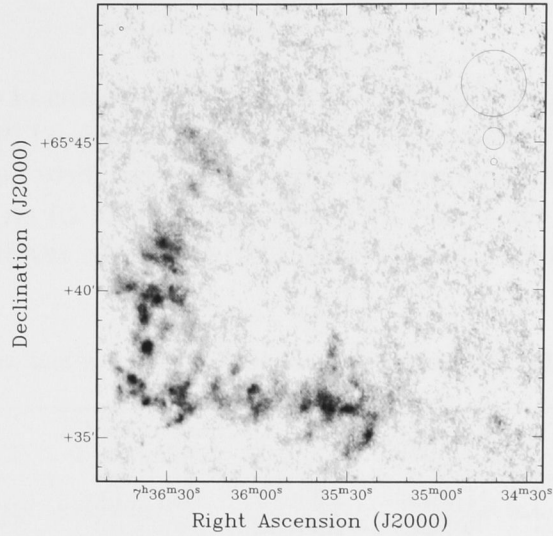
Figure 2.1 The relationship between the MSCLEAN scale sizes and structure in a single velocity channel of NGC 2403. The upper right corner shows the MSCLEAN scale sizes used in processing this galaxy (in red), from largest to smallest down the figure. All scales excluding the smallest scale (a delta peak) are shown. The diameters of the scales are 130″, 44″, 13″, 4″ and 1.3″. The beam is shown in the top left corner. The largest scale size (130″) roughly corresponds to the largest coherent structure visible in the channel map. This relation was used as the basis for choosing the MSCLEAN scales to be used for each galaxy.

that MSCLEAN indeed removes emission at larger scales before smaller scales (as explained in Section 2.1.3).
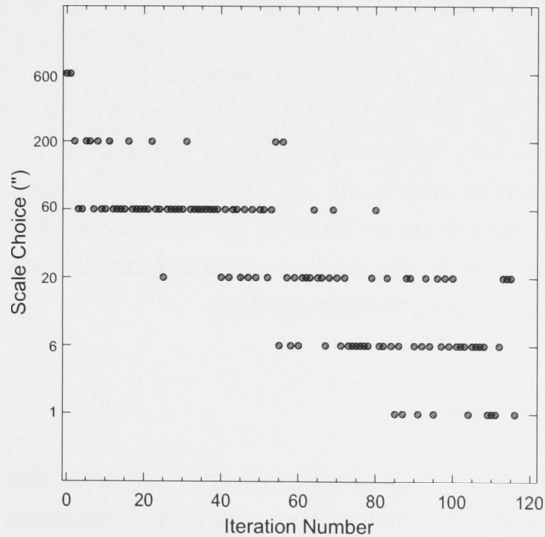
Figure 2.2 The choice of scale size with iteration number for a single velocity channel from Holmberg II in MSCLEAN . The x-axis shows the iteration number and the y-axis shows the scales (in arc-seconds). As shown, MSCLEAN uses the largest scales first, which corresponds to extended emission, before switching to smaller scales and cleaning finer structure.

17

2.2.3. Beams

In Table 2.1 we compare the sizes of the restoring beams of the AIPS CLEAN and the CASA/AIPS++ MSCLEAN. These are both determined by fitting a Gaussian function to the central component of the respective dirty beams. As their dirty beams are identical, the small differences seen in Table 2.1 are due to the different fitting procedures for a Gaussian function used in the restore processes of both software packages.

Table 2.1   FWHM Beam Size Comparison for CLEAN and MSCLEAN data.

| Source | Weighting | Beam Size (″) | | |
		NGC 2403	Holmberg II	IC 2574
CLEAN	Natural	8.8 × 7.7	13.7 × 12.6	12.8 × 11.9
	Robust	6.0 × 5.2	7.0 × 6.1	5.9 × 5.5
MSCLEAN	Natural	8.0 × 7.1	11.4 × 10.9	10.8 × 10.3
	Robust	5.7 × 4.9	6.6 × 5.8	6.3 × 5.9

In Figure 2.3 on Page 19 profiles of the restoring beams for both weightings and both data-sets are plotted against the respective dirty beam. It should be noted that natural weighting results in a beam that cannot be well approximated by a Gaussian function as shown in these figures. The natural dirty beam in Figure 2.3a has extended 'wings', while for a robust dirty beam (Figure 2.3b) these wings are much less pronounced and a Gaussian function is a much better fit.

Natural weighting is more sensitive to diffuse, extended emission. This is where CLEAN is at its weakest. The wings observed in the natural beam (Figure 2.3a) result in a large difference of the beam integral between the natural dirty and restoring beams. Robust weighting (Figure 2.3b) on the other hand is a much better fit to the actual dirty beam. So residual scaling for robust weighting is less important as there is less emphasis on extended structure. Therefore MSCLEAN and CLEAN results are much more similar for robust weighting in the case of the THINGS data. In the remainder of this comparison, the chapter focuses on the analysis based on the natural weighted data.

2.2.4. Channel Maps

A comparison of selected single channel maps for both the CLEAN and MSCLEAN natural-weighted cubes, including the respective residual channel maps, are shown in Figures 2.4 to 2.6 (on pages 20 to 22). The channel maps shown in these figures are from the non-residual scaled, unmasked THINGS cubes before correcting for primary-beam attenuation.

The CLEAN bowl is most noticeable in the NGC 2403 channel map (Figure 2.4 on Page 20), obscuring the noise in the inner region of the image. The CLEAN

(a) Natural **(b)** Robust
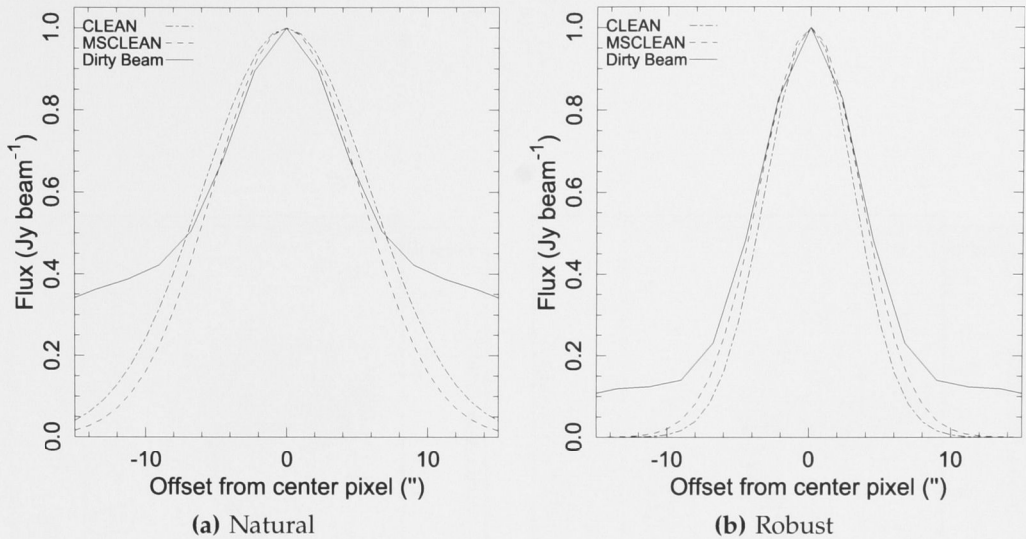
Figure 2.3 Profiles of the dirty beam (solid lines) and restoring or CLEAN beams for both CLEAN (dash-dot lines) and MSCLEAN (dashed lines) for the natural weighted (a) and robust weighted (with a robustness parameter of 0.5) data (b) of the galaxy IC 2574. The dirty beam for the natural weighted data on the left shows the significant wings which make it difficult to fit a Gaussian function to it. Nevertheless, the restoring beams of CLEAN and MSCLEAN are very similar for this weighting. On the other hand, The restoring beams for the robust weighted data are very similar and provide a good fit to the dirty beam, which is approximated well by a Gaussian function.

residuals also show a significant pedestal. This contributes to the difference in contrast between regions of low and high flux across the CLEAN and MSCLEAN data. For example, the extent of the high-contrast regions (black) are much larger in the channels from the CLEAN data. This pedestal also covers up the 'holes' in the flux in the CLEAN images, where in the MSCLEAN images one can see right down to the noise levels in these regions, as most readily seen in the channel map for Holmberg II (Figure 2.5 on Page 21).

(a) CLEAN

(b) MSCLEAN

(c) CLEAN Residual
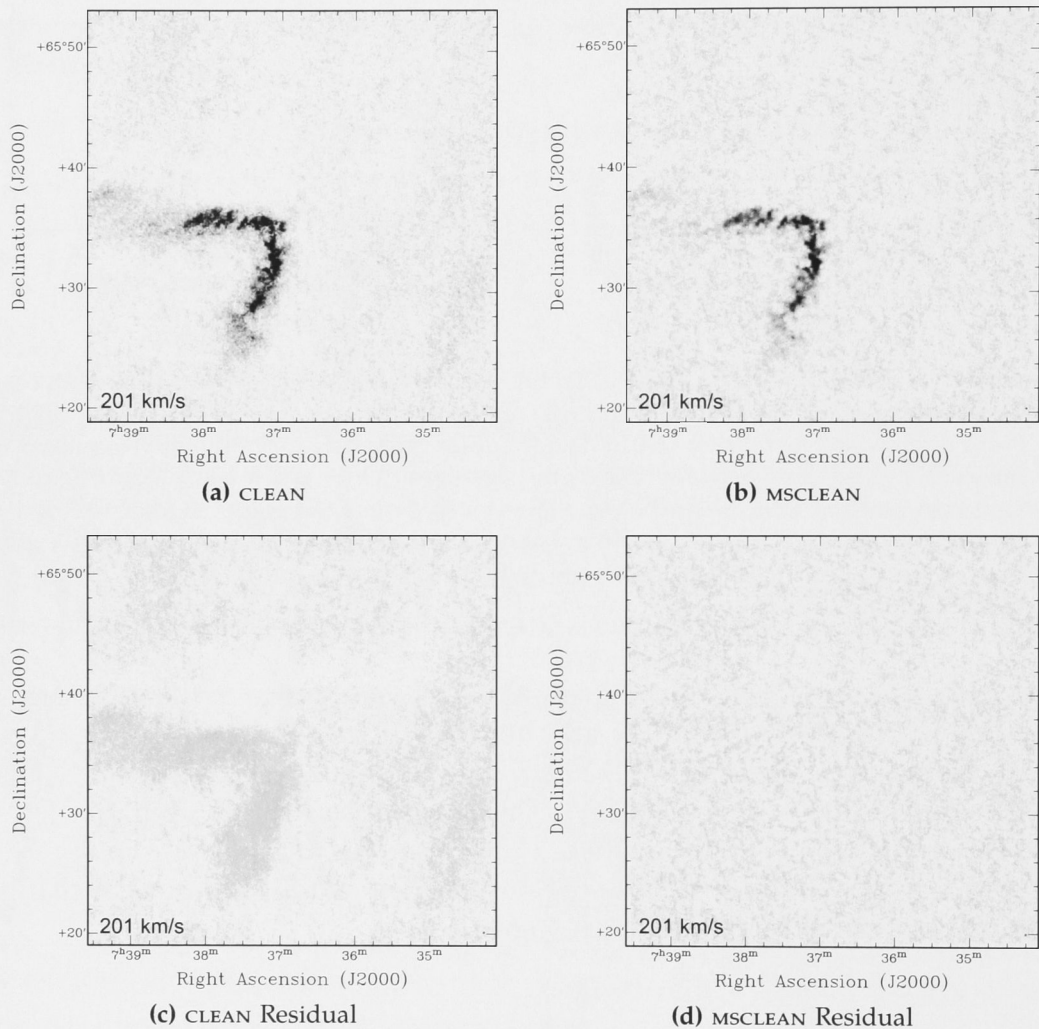
(d) MSCLEAN Residual

Figure 2.4 Comparison of a single channel map of NGC 2403 for the CLEAN (a) and MSCLEAN (b) data. Also shown is the respective residual channel map for the CLEAN (c) and MSCLEAN (d) data for NGC 2403, which is the, *e.g.*, MSCLEAN channel without adding in the convolved CLEAN components The channel maps were extracted from the natural-weighted, unmasked cubes. No primary beam correction has been applied. The CLEAN channel maps have not been residual corrected. The gray-scale levels run from 0 to 4 mJy beam^{-1}.
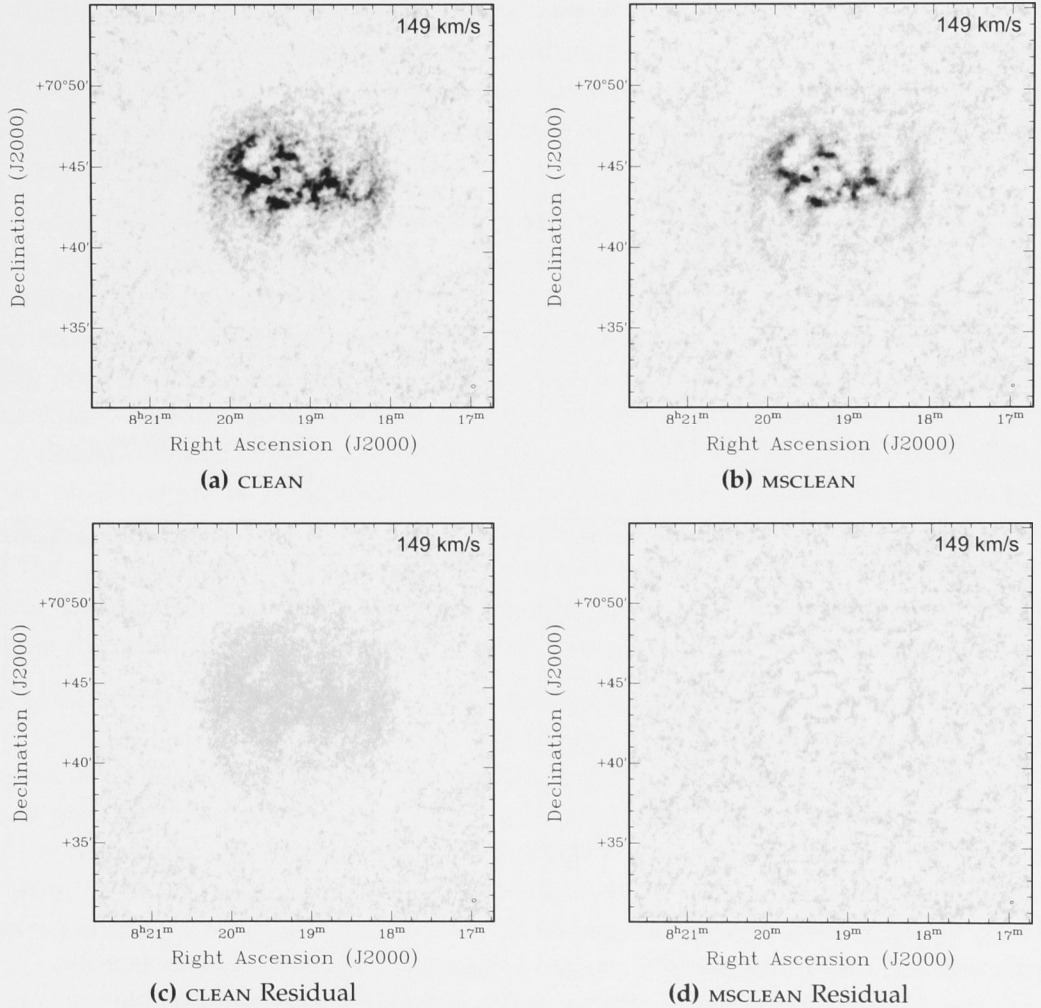
Figure 2.5 Comparison of a single channel map of Holmberg II for the CLEAN (a) and MSCLEAN (b) data. Also shown is the respective residual channel map for the CLEAN (c) and MSCLEAN (d) data for Holmberg II, which is the, *e.g.*, MSCLEAN channel without adding in the convolved CLEAN components The channel maps were extracted from the natural-weighted, unmasked cubes. No primary beam correction has been applied. The CLEAN channel maps have not been residual corrected. The gray-scale levels run from 0 to 10 mJy beam^{-1}.

(a) CLEAN

(b) MSCLEAN

(c) CLEAN Residual
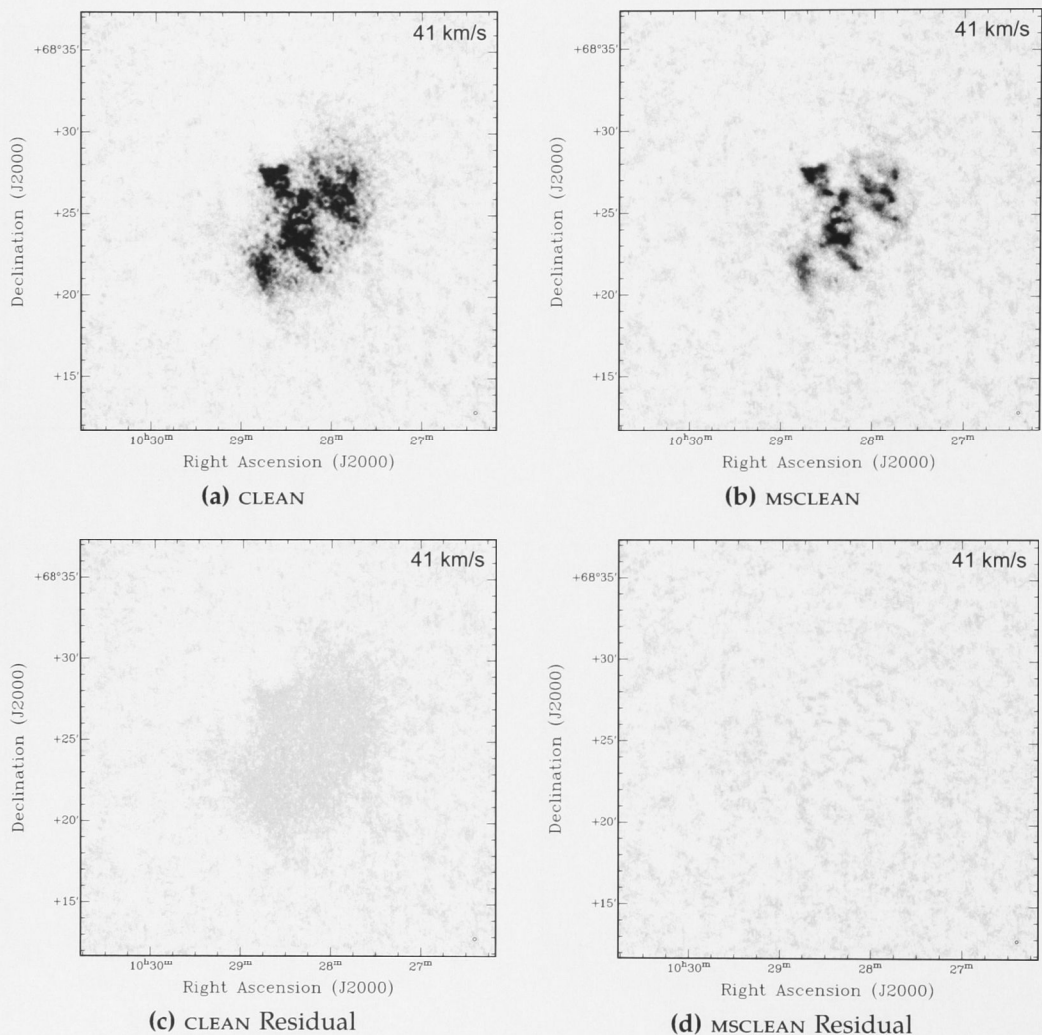
(d) MSCLEAN Residual

Figure 2.6 Comparison of a single channel map of IC 2574 for the CLEAN (a) and MSCLEAN (b) data. Also shown is the respective residual channel map for the CLEAN (c) and MSCLEAN (d) data for IC 2574, which is the, *e.g.*, MSCLEAN channel without adding in the convolved CLEAN components The channel maps were extracted from the natural-weighted, unmasked cubes. No primary beam correction has been applied. The CLEAN channel maps have not been residual corrected. The gray-scale levels run from 0 to 6 mJy beam^{-1}.

2.2.5. Integrated H I Maps

Integrated H I maps, as well as integrated residual maps for each galaxy are shown in Figures 2.7, 2.8 and 2.9 (pages 24, 25 and 26) for the MSCLEAN and CLEAN natural-weighted, primary-beam corrected (and for CLEAN, residual-scaled) data. The cubes were masked with the same masks applied to the CLEAN data (see Walter et al., 2008, for a description of the masking process). The residual integrated maps were generated from residual cubes, *i.e.*, cubes that were cleaned but did not have the CLEAN components added to them. These integrated maps have not been corrected for primary-beam attenuation and for the CLEAN data, no residual scaling has been applied.

The masking applied to the integrated maps hides the signature of the clean bowl seen in the channel maps of the CLEAN data in Figures 2.4 to 2.6. The residual integrated CLEAN maps in Figures 2.7 to 2.9 do show a significant pedestal of uncleaned flux, while the MSCLEAN residual maps have no such feature. There is trace source emission in the MSCLEAN residual integrated maps, but generally the residuals are much more 'noise-like'. Despite being on the same flux scale, there is a definite visual difference between the CLEAN and MSCLEAN data, most clearly seen where there is significant source flux (the darker regions) in Holmberg II and IC 2574. Conversely the low-level extended structure is more clearly seen in the MSCLEAN integrated maps and extends out to the mask boundary. The peak flux for compact features is therefore higher in the CLEAN integrated images, while the total flux of the underlying, extended structure is greater in MSCLEAN.

To compare the flux scales between the data-sets, contour lines of column density $1 \cdot 10^{21}$ and $2 \cdot 10^{21}$ cm^{-2} have been plotted on the (residual scaled) CLEAN and MSCLEAN data for each galaxy, shown in Figures 2.10, 2.11 and 2.12. Again, this data has been masked and corrected for primary-beam attenuation. The location of the contours match closely across the CLEAN and MSCLEAN data, but they appear much smoother in the CLEAN data. The contours in the MSCLEAN images for each galaxy appears to trace a much finer structure boundary. This is likely due to the pedestal of leftover flux in classical CLEAN. The pedestal still has the dirty beam as its PSF, the more extended wings of this beam will wash out structure more severely than a Gaussian beam, and the low-level, small-scale structure will be lost in the image. For low-level column densities the CLEAN resolution is thus worse than one would expect on the basis of the clean beam size, as we will show later. In MSCLEAN there is no pedestal, and all fine-scale structure is imaged at the full resolution of the clean beam, enhancing the detailed structures in the disk.

(a) CLEAN

(b) MSCLEAN

(c) CLEAN Residual
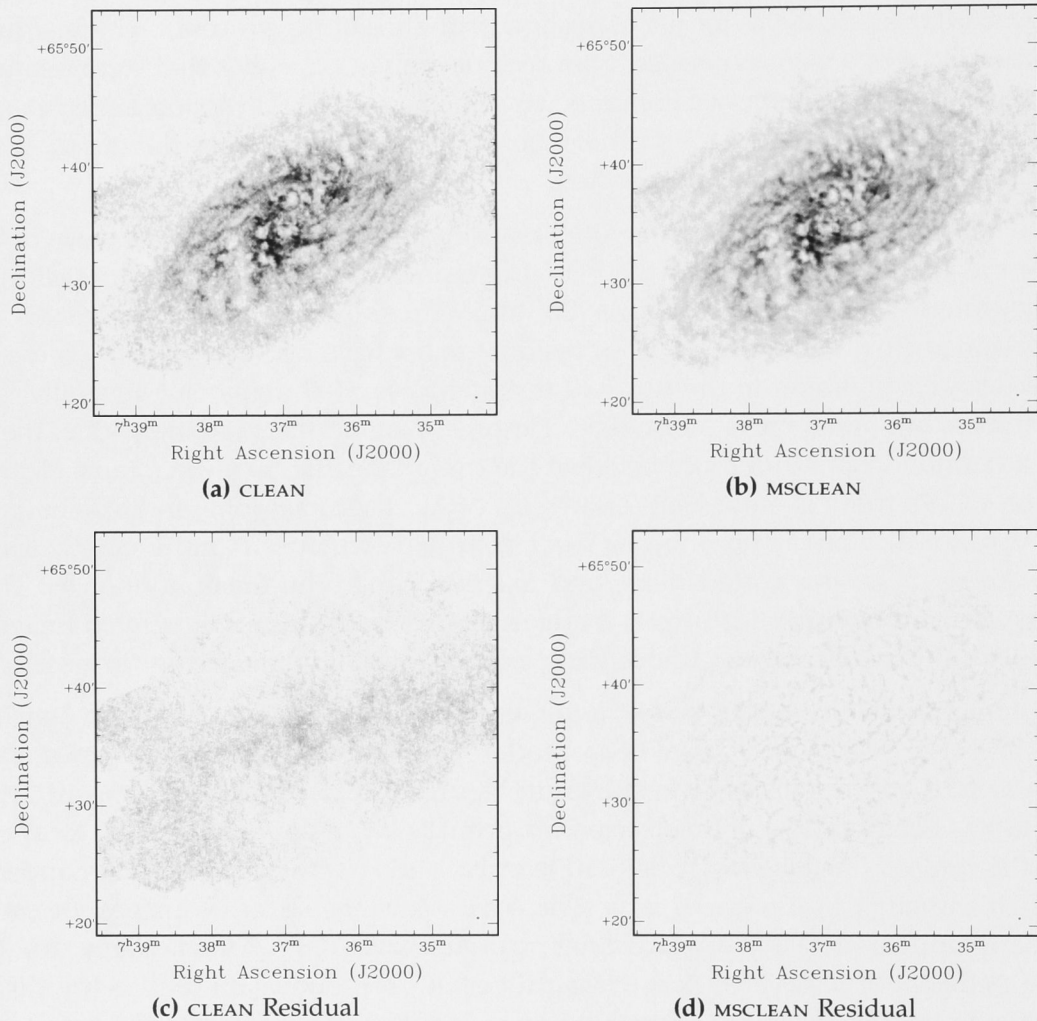
(d) MSCLEAN Residual

Figure 2.7 CLEAN (a) and MSCLEAN (b) integrated H I maps for NGC 2403. The maps were generated from the natural-weighted, masked, primary-beam corrected and for CLEAN, residual flux corrected cubes. The equivalent residual integrated H I maps are also shown in (c) and (d) respectively, generated as described in Sec. 2.2.5. No primary-beam corrections and for CLEAN, no residual flux corrections have been applied to these images. The gray-scale levels run from 0 to 200 mJy beam^{-1} km s^{-1}. Beams are marked in bottom right corner of images.

(a) CLEAN

(b) MSCLEAN

(c) CLEAN Residual
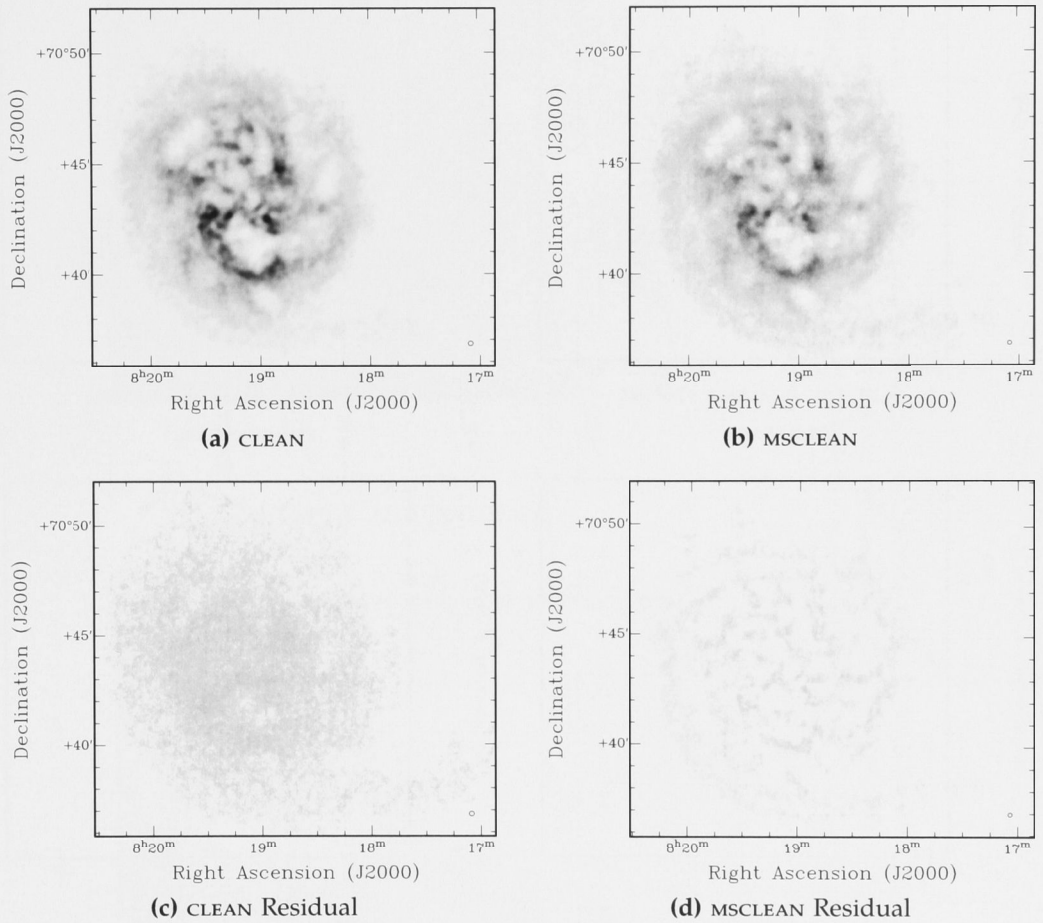
(d) MSCLEAN Residual

Figure 2.8 CLEAN (a) and MSCLEAN (b) integrated H I maps for Holmberg II. The maps were generated from the natural-weighted, masked, primary-beam corrected and for CLEAN, residual flux corrected cubes. The equivalent residual integrated H I maps are also shown in (c) and (d) respectively, generated as described in Sec. 2.2.5. No primary-beam corrections and for CLEAN, no residual flux corrections have been applied. The gray-scale levels run from 0 to 500 mJy beam^{-1} km s^{-1}. Beams are marked in bottom right corner of images.

(a) CLEAN

(b) MSCLEAN

(c) CLEAN Residual
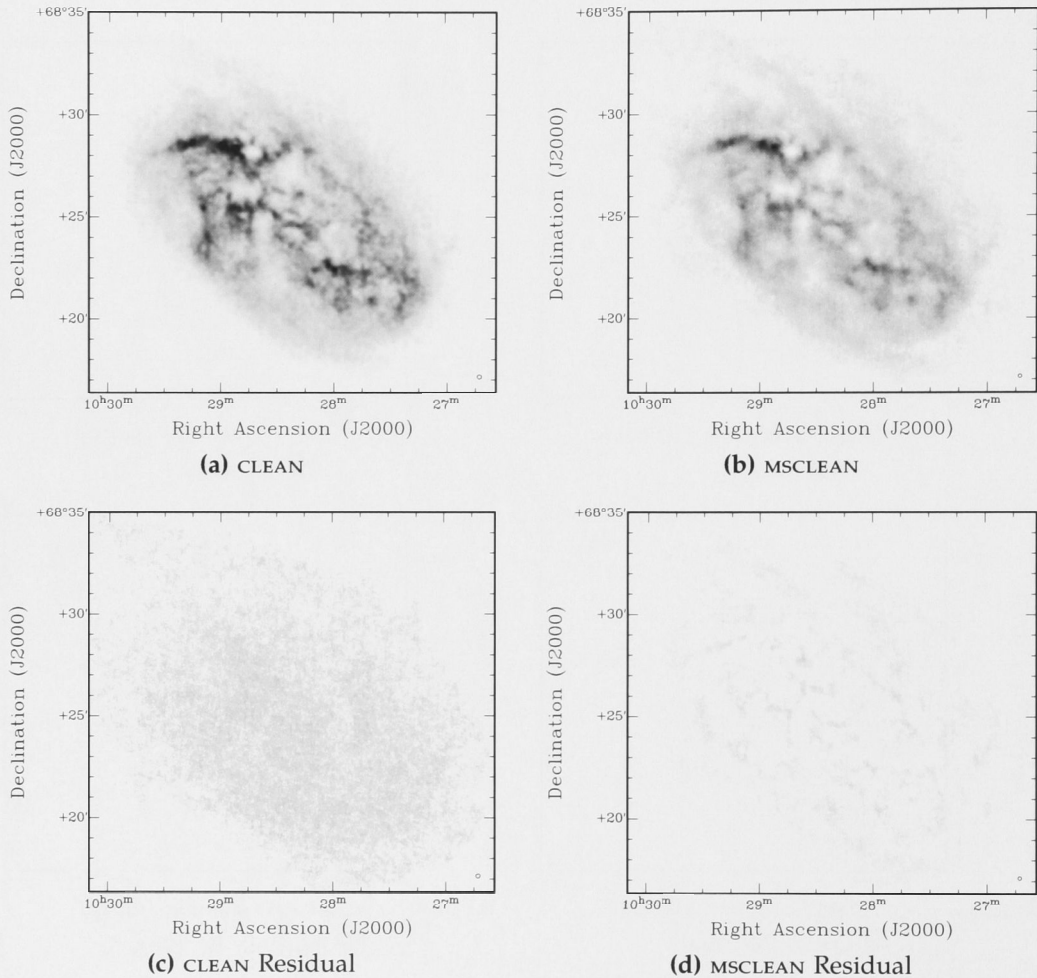
(d) MSCLEAN Residual

Figure 2.9 CLEAN (a) and MSCLEAN (b) integrated H I maps for IC 2574. The maps were generated from the natural-weighted, masked, primary-beam corrected and for CLEAN, residual flux corrected cubes. The equivalent residual integrated H I maps are also shown in (c) and (d) respectively, generated as described in Sec. 2.2.5. No primary-beam corrections and for CLEAN, no residual flux corrections have been applied. The gray-scale levels run from 0 to 450 mJy beam^{-1} km s^{-1}. Beams are marked in bottom right corner of images.
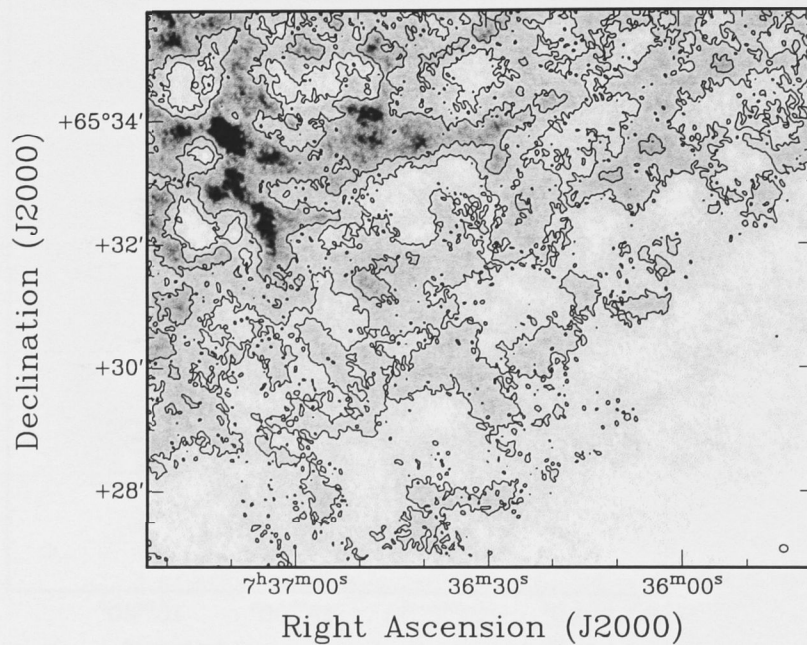
Figure 2.10 Comparison of flux levels for NGC 2403 on an integrated intensity map for CLEAN (a) and MSCLEAN (b). Images were generated from the natural-weighted, masked and primary-beam corrected data. The CLEAN image has been residual flux corrected. Contour levels of column density are plotted at $1 \cdot 10^{21}$ and $2 \cdot 10^{21}$ cm^{-2}. The gray-scale levels run from 0 to 200 mJy beam^{-1} km s^{-1}. Beams are marked in bottom right corner of images.
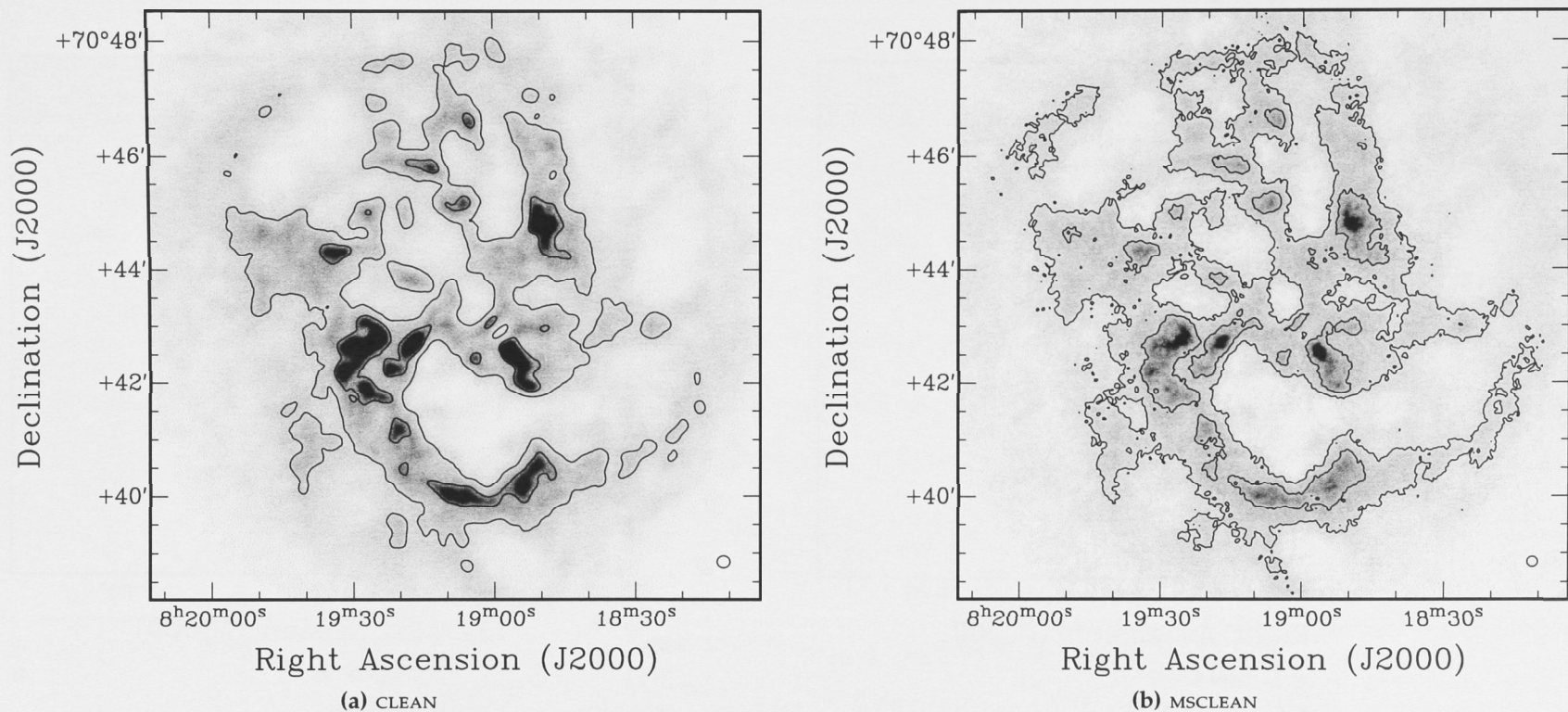
Figure 2.11 Comparison of flux levels for Holmberg II on an integrated intensity map for CLEAN (a) and MSCLEAN (b). Images were generated from the natural-weighted, masked and primary-beam corrected data. The CLEAN image has been residual flux corrected. Contour levels of column density are plotted at $1 \cdot 10^{21}$ and $2 \cdot 10^{21}$ cm^{-2}. The gray-scale levels run from 0 to 500 mJy beam^{-1} km s^{-1}. Beams are marked in bottom right corner of images.
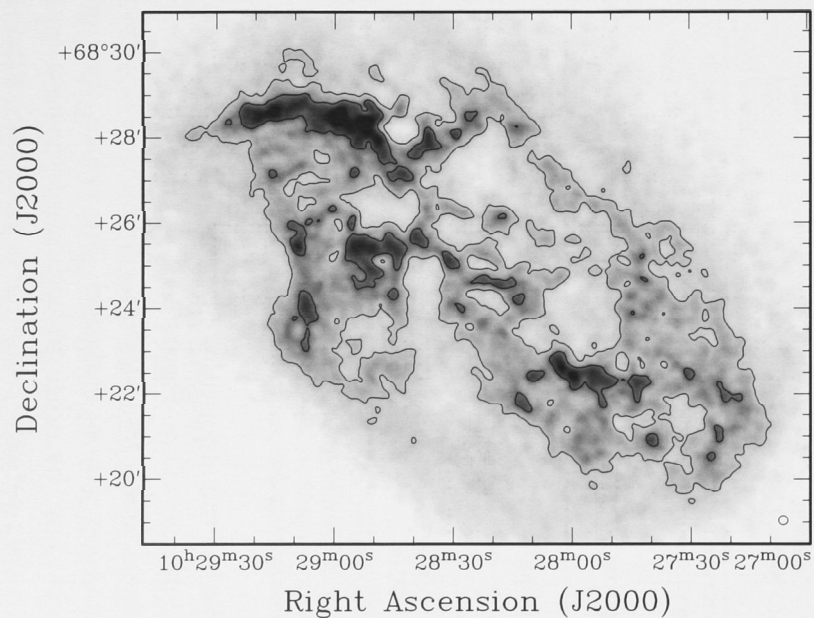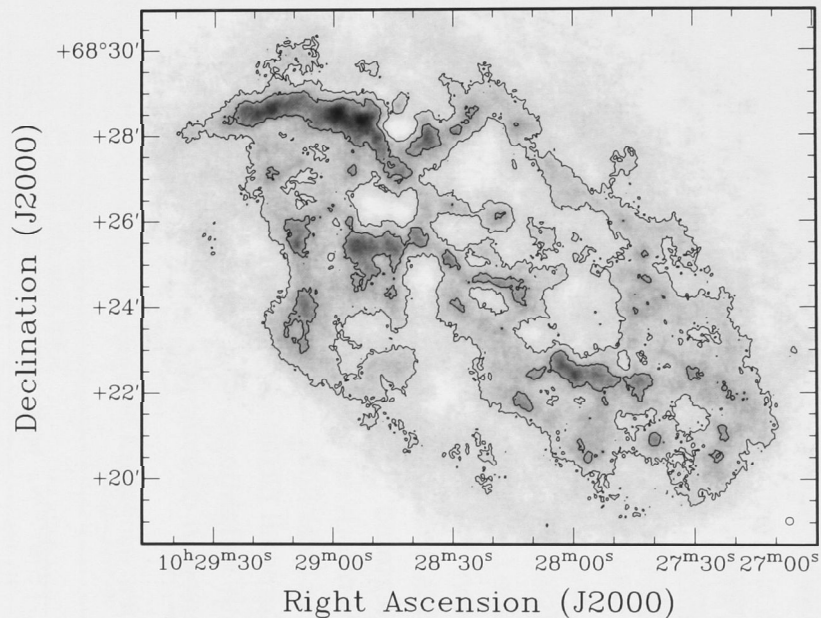
(a) CLEAN

(b) MSCLEAN

Figure 2.12 Comparison of flux levels for IC 2574 on an integrated intensity map for CLEAN (a) and MSCLEAN (b). Images were generated from the natural-weighted, masked and primary-beam corrected data. The CLEAN image has been residual flux corrected. Contour levels of column density are plotted at $1 \cdot 10^{21}$ and $2 \cdot 10^{21}$ cm^{-2}. The gray-scale levels run from 0 to 450 mJy beam^{-1} km s^{-1}. Beams are marked in bottom right corner of images.

2.2.6. Flux and Noise Measurements

Table 2.2 shows the comparison of total flux for both weightings for the CLEAN and MSCLEAN data. The total flux for the MSCLEAN data was calculated from the masked cubes after primary-beam correction, using the STAT task of the GIPSY[10] software package. The total flux values for the CLEAN data are derived with the same method, using the primary-beam corrected data with residual-scaling applied. The uncertainties in the flux densities measured here is of the same order as the flux calibration (~ 10%, see Walter et al., 2008). From Table 2.2, in all three galaxies it can be seen that MSCLEAN recovers more flux than classical CLEAN for a given weighting. This is despite apparently higher peak fluxes for compact sources in the CLEAN integrated H I maps of Figures 2.7 to 2.9. The flux gains by MSCLEAN are therefore mostly in the recovery the extended source structure. The relative differences in total fluxes as listed in Table 2.2 are consistent with the results derived by Cornwell (2008) using artificial data. Table 2.3 shows the *rms* noise values for both weightings. The noise was determined in line-free channels that were not used in determining the continuum.

Table 2.2   Total flux comparison of CLEAN and MSCLEAN for each galaxy.

Source	Weighting	Total Flux (Jy km s^{-1})		
		NGC 2403	Holmberg II	IC 2574
CLEAN	Natural	1055	219	387
	Robust	977	210	363
MSCLEAN	Natural	1200	261	418
	Robust	1205	271	426
Single-dish		1172 ± 553	245 ± 54	466 ± 69

Note: The measurements for CLEAN were made on data which had been residual flux corrected.

Table 2.3   Noise level comparison for CLEAN (without residual-scaling) and MSCLEAN images.

Source	Weighting	Noise (mJy beam^{-1})		
		NGC 2403	Holmberg II	IC 2574
CLEAN	Natural	0.38	0.92	0.56
	Robust	0.45	1.06	0.69
MSCLEAN	Natural	0.41	0.93	0.57
	Robust	0.50	1.11	0.68

Note: The measurements for CLEAN were made on data which had not been residual flux corrected and all measurements were made in line-free channels that were not used in determining the continuum.

An important issue is whether the algorithms alter the amplitude or distribution of noise in the data in a significant way. Figure 2.13 on Page 31 shows histograms of the flux values in a channel that is free of galaxy emission and within an empty region of a channel containing galaxy emission. For CLEAN, the non residual-scaled data has been used. For the noise in both emission and emission-free channels, and across both data-sets the noise has a Gaussian distribution. The

noise in the empty channels of the MSCLEAN and CLEAN data (left column) is identical. For channels containing emission there is a slight bias to negative values in the CLEAN data, due to the clean bowl. We also note that there is a similar but smaller bias in the noise in the MSCLEAN emission channel. It is clear however, that neither algorithm alters the noise significantly.
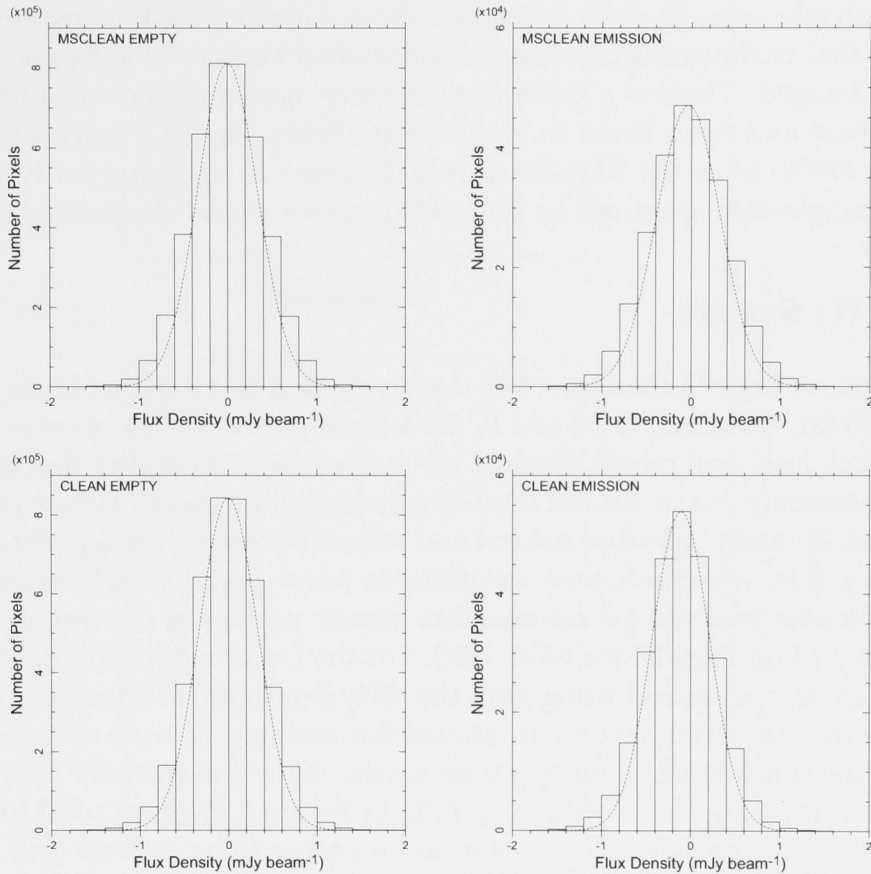
Figure 2.13 Histograms of the flux density in the galaxy NGC 2403 for both MSCLEAN (top) and CLEAN (bottom). On the left are histograms calculated an empty channel in the unmasked, non primary-beam corrected (and non residual-scaled for CLEAN) data cube located at a heliocentric velocity of 278 km s^{-1}. On the right are histograms calculated in a 500×500 pixel box situated in an empty part of the channel containing galaxy emission at a heliocentric velocity of 201 km s^{-1}. For each plot, 25 bins of width 0.18 mJy beam^{-1} have been used. Also, for each histogram, the Gaussian fit to the histogram values has been plotted (dotted line).

Comparison to Single-dish Measurements

Ideally one would like to compare the derived flux values with total flux values derived using single-dish instruments. Unfortunately for the THINGS galaxies their large extent leads to single-dish measurements which are more uncertain than one would like. In Table 2.2 the single-dish fluxes derived by computing

the average values and standard deviations of the single dish fluxes listed in the NASA/IPAC Extragalactic Database (NED) are listed. In general there see a good agreement, but a more precise comparison is precluded by the uncertainty in the single dish values. It should be noted that for such objects, single-dish flux measurements are dependant on the telescope used. Because of their extent, objects such as the THINGS galaxies often encompass the full primary beam of a single-dish telescope. In order to increase the accuracy of the flux measurements, a region that encloses the object and a substantial amount of surrounding area must be imaged. There is a general satisfactory agreement between the fluxes derived here and those listed in Walter et al. (2008). Finally, Figure 4 in Walter & Brinks (1999) plots the VLA H I (residual-corrected) spectrum for IC 2574 on top of a single-dish spectrum by Rots (1980) which shows excellent agreement.

2.2.7.   H I Spectra

Figure 2.14 on Page 33 shows the flux density plotted as a function of velocity for NGC 2403 (a), Holmberg II (b) and IC 2574 (c) respectively. The MSCLEAN natural (solid black line) and robust (dashed black line) result in higher flux densities than the standard CLEAN natural (dotted gray line) and robust (dashed gray line) cubes. Additionally, MSCLEAN natural and robust weighting are equally good at recovering flux, whereas robust weighting is worse than natural weighting for CLEAN. We also compare the residual flux density profiles of the two algorithms in Figure 2.15 on Page 34 for NGC 2403. For the CLEAN algorithm, the residual profile has been corrected using both the dirty beam (*i.e.*, residual flux scaling) and with the CLEAN beam (without residual flux scaling). Because MSCLEAN cleans close to the noise level on all specified scales, there is essentially little source emission remaining in its residual profile in Figure 2.15 (gray solid line). On the other hand, the classical CLEAN residual profile (long-dashed gray line) is a constant, flat line at a flux density of approximately 0.5 Jy, showing that the algorithm has left source emission uncleaned, due to the flux cut-off used in the CLEAN process only acting on the full resolution residuals. Correcting this residual profile using the CLEAN beam leads to a significantly higher residual profile (gray short dashed line) that will result in erroneous flux measurements, as opposed to measurements using the same residual profile but corrected using the dirty beam (gray long dashed line).

We also present a radial H I column density profile in Figure 2.16 on Page 35 for NGC 2403. The H I column density profile has been plotted for the CLEAN data with and without residual flux scaling applied and for the MSCLEAN data. All profiles were generated using the ELLINT task in the MIRIAD software package, in 10″ increments, correcting for the position angle and inclination of the H I disk. As can be seen, not applying residual flux scaling can lead to an overestimate of the H I flux (and thus column density) in the inner parts of the disk. As the disk radius increases, the non residual-scaled CLEAN profile begins to equal the
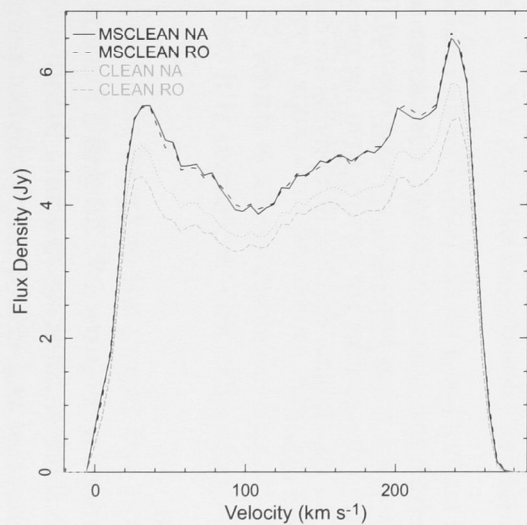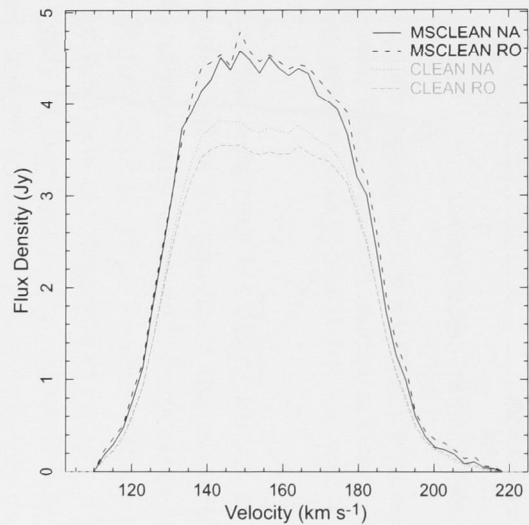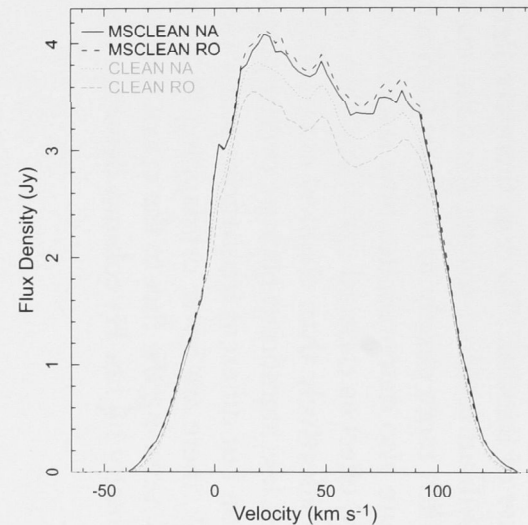
Figure 2.14 Global H I Profiles of NGC 2403 (a), Holmberg II (b) and IC 2574 (c). Both natural and robust CLEAN and MSCLEAN profiles are shown. The profiles are derived from masked, primary-beam corrected (and for CLEAN, residual scaled) data.

MSCLEAN and CLEAN residual scaled profiles, then drops below the latter two profiles out to the extremes of the disk. There is therefore significant variations in the fluxes measured without residual-scaling the data. CLEAN with residual-scaling applied agrees much more closely to MSCLEAN than when not applying residual scaling. The figure also demonstrates how MSCLEAN does not suffer as much from the CLEAN bowl effect as classical CLEAN and thus can probe the outer regions of the disk more effectively than classical CLEAN. In the inner parts of the disk, the CLEAN bowl is less significant because overlapping emission located at the same spatial position but different frequencies partly cancels its effect. In the outer parts of the disk, there are fewer overlapping flux regions, and so the bowl has a larger effect, depressing the flux in the CLEAN profile. MSCLEAN on the other hand shows consistently higher H I column densities out to the extremes of the disk.
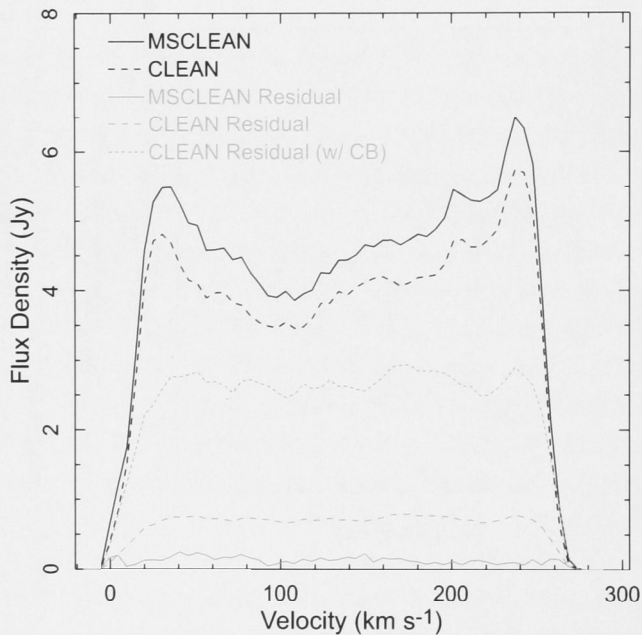
Figure 2.15 Total (black) and residual (gray) H I flux profiles for the natural-weighted MSCLEAN (solid) and CLEAN (long dashed) data cubes of NGC 2403. Also shown is the CLEAN residual flux profile calculated using the CLEAN beam (*i.e.,* without residual flux scaling) as the short-dashed gray line. Total flux profiles are derived from the masked, primary-beam corrected (residual scaled for CLEAN) data. Residual flux profiles are derived from masked, non primary-beam corrected data.

2.2.8. Power Spectra

The integrated moment maps in Figures 2.7, 2.8 and 2.9 seem to indicate that the MSCLEAN maps contain more small-scale structure than the CLEAN maps. The difference between the MSCLEAN and CLEAN maps can be quantified using the

34

(×10²¹)
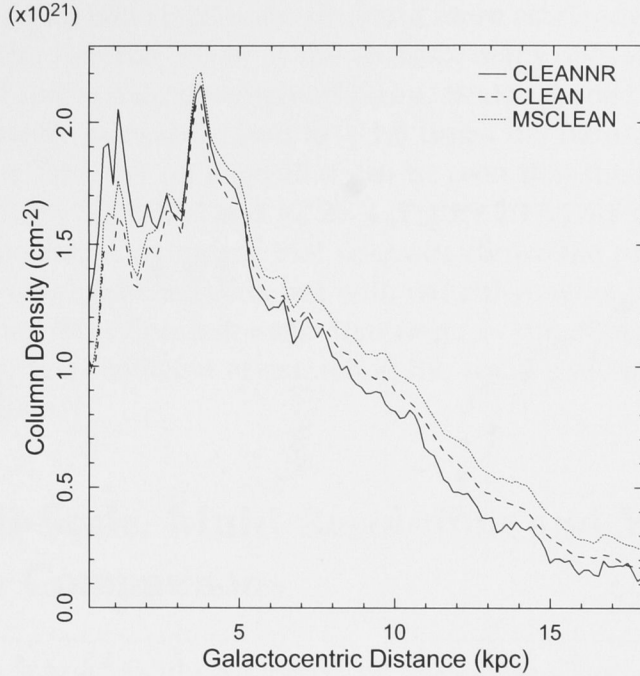
Figure 2.16 The radial H I column density profile of the galaxy NGC 2403 for CLEAN without residual scaling (solid line), CLEAN with residual scaling (dashed line) and MSCLEAN (dotted line). The masked, primary-beam corrected data was used for the generation of the profiles.

power spectrum of the resulting H I distributions in both types of maps. We derive the power (defined as the square of the modulus of the Fourier transform of the image) in azimuthally averaged rings with logarithmically increasing baseline length. Figure 2.17 on Page 36 shows the power spectra for our three sample galaxies for both sets of integrated H I maps. Both the CLEAN and MSCLEAN spectra flatten sightly at large scales (*i.e.*, shortest baselines), possibly indicating that some of these largest scales are not completely probed by the VLA, even at its shortest baselines. Alternatively it may indicate that these largest scales are simply not present in the galaxies under consideration. It is clear though that at large scales there is good agreement.

As the spatial scale probed approaches the size of the natural-weighted beam however, the power in the CLEAN integrated moment maps begins to decrease compared to the MSCLEAN maps. At about ∼ 1.5 times the natural-weighted beam size we start to see a significant deviation. Also shown in Figure 2.17 is a power law with slope −3 which is a reasonable description for the power spectrum at intermediate scales. It is consistent with values found in other galaxies (Muller et al., 2004).

We will not attempt here to relate the power law slope to *e.g.*, the turbulence or the energy input of the ISM, but we draw attention to the fact that as the small-scale power in the CLEAN maps starts to fall away, the MSCLEAN power spectrum continues to follow this power-law behavior. This indicates that the
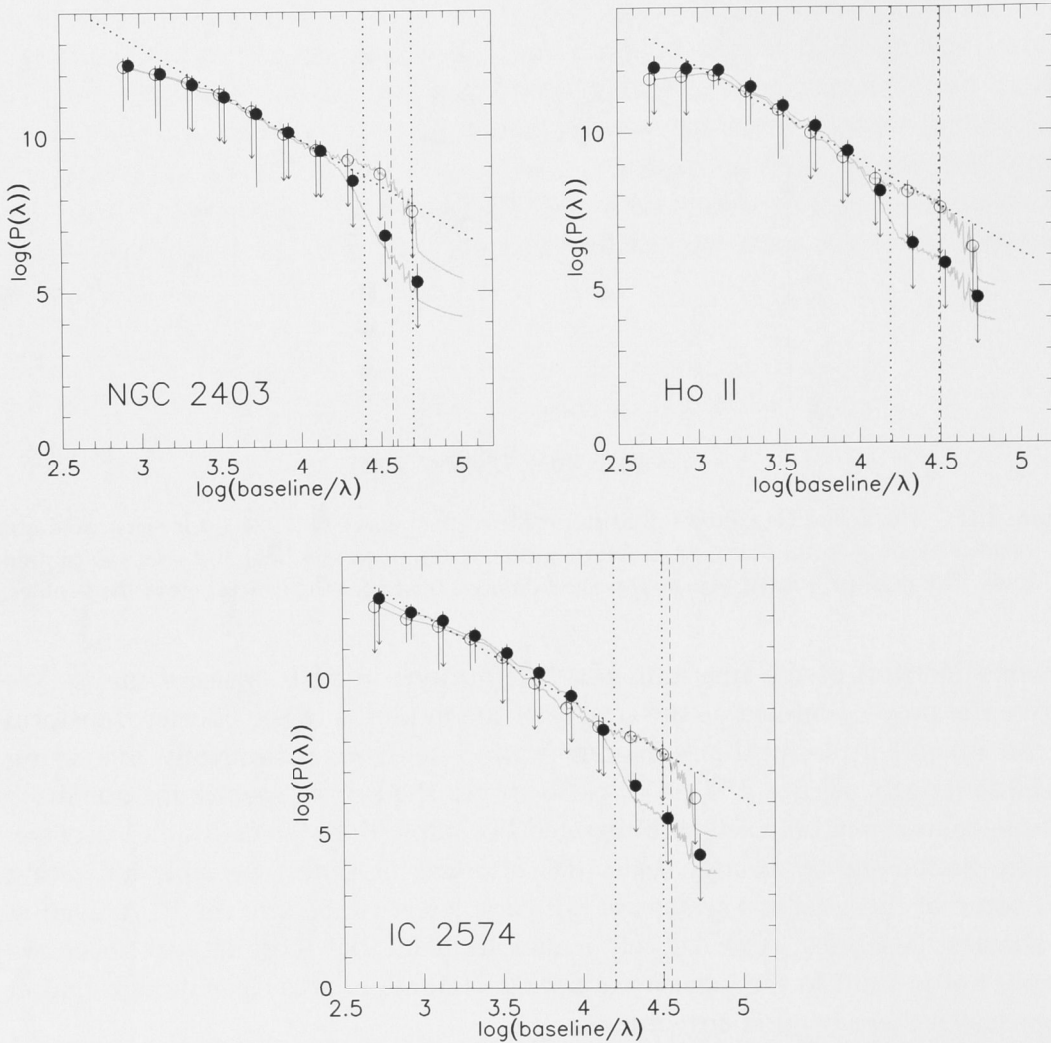
Figure 2.17 Power spectra of the natural-weighted integrated H I maps (galaxies as marked). Filled circles show the standard CLEAN data, open circles the MSCLEAN data. The points show logarithmically binned data, the thin gray lines show the actual behaviour of the power in linearly sampled intervals. The diagonal dotted line has a power law slope of −3. Note that it is not a fit to the data. The left-most dotted vertical line shows the natural-weighted beam size, the right-most dotted line half the natural-weighted beam size. The vertical dashed line shows the robust-weighted beam size. Arrows indicate that the lower error-bars extend beyond the plotted range.

MSCLEAN maps probe real small-scale structure more efficiently than the classical CLEAN maps. Note that the power in the MSCLEAN maps only starts to drop away at scale sizes of half a natural-weighted beam. Scales probed in classical CLEAN are only completely sampled down to ~ 1.5 times the natural-weighted beam size. Looking at Table 2.1 on Page 18 it can be seen that the robust beam sizes for Holmberg II (Figure 2.17b) and IC 2574 (Figure 2.17c) are about half the size of the natural beams. This means that MSCLEAN allows the probing of scales at close to robust-weighted resolution but with natural-weighted sensitivity, and at correct flux scales. This does not mean that MSCLEAN can super-resolve data, just that it is simply more efficient at extracting the small-scale information that is present in the data.

2.3. Multi-Scale, Multi-Resolution and Windowed CLEAN Comparisons

So far we have only explicitly compared MSCLEAN with classical CLEAN. We now extend our comparisons to also include CLEAN windows in combination with classical CLEAN, and include the version of MSCLEAN implemented in AIPS. We refer to this algorithm as AIPS Multi-Resolution CLEAN in keeping with the terminology used within the AIPS documentation. We note however, that it is not an implementation of the original multi-resolution CLEAN (Wakker & Schwarz, 1988) and so is similar in name only. The algorithm behind AIPS Multi-Resolution CLEAN is the similar to the algorithm used by MSCLEAN. MSCLEAN and AIPS Multi-Resolution CLEAN can therefore be thought of as differing implementations of the same scale-sensitive deconvolution algorithm.

A small variation on standard CLEAN, which does not alter the algorithm in any way, is to define a CLEAN 'window', restricting the CLEAN processing to a defined area of the dirty map. The advantage of this windowed-CLEAN is a greatly increased processing speed, particularly for extended sources. By defining a CLEAN window, CLEAN is restricted to where it can find components. However, care must be taken not to define a window that is too small to encompass low-level extended structure. Obviously, for the case of extended emission throughout a large fraction of the primary beam, the CLEAN window has to become so large that a windowed-CLEAN reverts to a simple un-windowed CLEAN.

For these comparisons between the algorithms, we have used a channel map from Holmberg II located at heliocentric velocity 165 km s^{-1}. For MSCLEAN and AIPS Multi-Resolution CLEAN, six scales/resolutions were chosen, using the same method as described in Section 2.2.2. The diameters from smallest to largest were 0″, 4″, 13″, 40″, 133″ and 400″. A gain of 0.7 was used for MSCLEAN and AIPS Multi-Resolution CLEAN (the same gain as used for MSCLEAN before) while a gain of 0.1 was used for the window CLEAN (in line with the gain used in classical

CLEAN). For all algorithms, a flux threshold of of 2.3 mJy beam^{-1} (2.5σ) was used in all algorithms. Maximum iteration limits of 5000 were set for MSCLEAN and AIPS Multi-Resolution CLEAN and 100000 for the window CLEAN. We note that for all algorithms the flux threshold was reached before hitting the iteration limit.

2.3.1. Beams, Total Flux and Noise Measurements

Values for the CLEAN beams, total flux recovered and the *rms* noise can be found in Table 2.4. To measure the flux, a mask was created from the MSCLEAN restored image by blanking out all emission below a 2σ level and applying this mask to all the images. The resulting masked image was corrected for the primary beam and used to measure the flux. For CLEAN and windowed CLEAN, residual-corrected images were used for measuring the total flux. For measuring the *rms* noise, unmasked, non primary beam corrected (and for CLEAN with/without windows, non residual-scaled) images were used. The *rms* noise was measured in a 50 × 50 pixel box within the cleaned region of each image, and in a location with no source emission.

Table 2.4   Beam, Total Flux and *rms* Noise comparison for MSCLEAN, AIPS Multi-Resolution CLEAN, windowed CLEAN and CLEAN in Holmberg II.

Algorithm	Beam Size (″)	Flux Recovered (Jy)	*rms* Noise (mJy beam^{-1})
MSCLEAN	11.3 × 10.8	3.11	0.83
AIPS Multi-Resolution CLEAN	13.7 × 12.6	3.02	0.87
CLEAN	13.7 × 12.6	2.77	0.88
Windowed CLEAN	13.7 × 12.6	2.88	0.91
Windowed CLEAN (1σ)	13.7 × 12.6	2.93	1.3
Windowed CLEAN (0.5σ)	13.7 × 12.6	2.95	1.6

Note: Total flux measurements for CLEAN and windowed CLEAN were made with data that was residual flux corrected, while *rms* noise measurements were made with data which was not residual flux corrected.

Windowed CLEAN recovers ~ 5% more flux than CLEAN, but does not recover as much flux as the two scale-sensitive algorithms. The number of iterations taken for each to reach the flux threshold were 3500 for MSCLEAN, 4050 for AIPS Multi-Resolution CLEAN, 5100 for windowed CLEAN and 9720 for CLEAN. The flux gains made here on real data by the scale-sensitive algorithms are in line with the gains made by these algorithms on simulated data (Cornwell, 2008). The *rms* noise measurements are in good agreement, which indicates that none of the algorithms significantly changes the noise properties of the data. We note that the small differences in noise levels between those listed in Table 2.4 (as derived for Holmberg II using MSCLEAN, AIPS Multi-Resolution CLEAN and CLEAN) are slightly different from those listed in Table 2.3 on Page 30 (as determined for a line-free channel in the Holmberg II data cube). This difference is mostly attributable to small channel-to-channel changes in the average noise level, as

well as small statistical spatial noise fluctuations in each channel. We find these noise measurements to have a dispersion of ~ 0.03 mJy for this particular case.

When using CLEAN windows, the search for CLEAN components is restricted to the area of known flux (*i.e.*, the window) and it should therefore in principle be possible to CLEAN to a deeper level, thus increasingly negating the need for residual scaling. We have tested this by running windowed CLEAN down to additional flux thresholds of 1σ and 0.5σ in Holmberg II. The total flux recovered and the *rms* noise are listed in Table 2.4 on Page 38. We note there is a significant increase in the number of iterations required to CLEAN down to these flux thresholds, with a marginal gain in recovered flux. For a 1σ threshold, 38000 iterations are required and for a 0.5σ level, 198000 iterations are needed. For the original 2.5σ threshold, 5000 iterations were required. In comparison, MSCLEAN and AIPS Multi-Resolution CLEAN recover more flux without an increase in *rms* noise, and with fewer iterations.

The resulting channel maps along with the channel map for the original windowed CLEAN to 2.5σ flux threshold are shown in Figure 2.18 on Page 41. The window applied is marked by the black box around the emission in the images. The box was chosen based on emission visible in the dirty image. After deconvolution, additional emission became visible outside our CLEAN window (as shown in Figure 2.18 on Page 41). Normally one would adjust the CLEAN window and perform further CLEAN runs. Here, however, we only show the result from our first run, as this clearly illustrates the differences in noise properties inside and outside the CLEAN box. Immediately noticeable in these images is the increased 'spottiness' that comes with cleaning to a deeper flux level. This is most likely due to CLEAN operating into the noise and thus cleaning noise spikes as opposed to real emission with a distortion of the noise. This can be seen in the histograms of Figure 2.18 which show the increased *rms* noise for the deepest windowed CLEANS and is also clear from the measured *rms* listed in Table 2.4. Alternatively, it could be due to attempting to represent extended, continuous emission by a collection of point sources, as CLEAN does. The histograms show minimal distortion overall, which could indicate the spottiness is a result of poor representation of the extended source. The same negative bias as observed in Figure 2.13 on Page 31 is seen in the histogram of the windowed CLEAN down to a flux threshold of 2.5σ (Figure 2.18a), but this bias disappears for deep windowed CLEANS (Figures 2.18b and 2.18c). A deep windowed CLEAN can therefore eliminate the negative bowl, but does so at the cost of distorted (and increased) noise. These results are in line with those on simulated data by Cornwell (2008).

We note that the definition of a CLEAN window is trivial for the case of a single channel map discussed here. For a large data-cube of a complicated extended source, an individual CLEAN window would need to be defined for each channel of the cube, as the structure of the source in each channel changes in both shape and position. It is therefore impractical to use windowed CLEAN for the THINGS

sample, where the number of spectral channels for a single galaxy can be as high as 100.

(a) 2.5σ **(b)** 1.0σ **(c)** 0.5σ
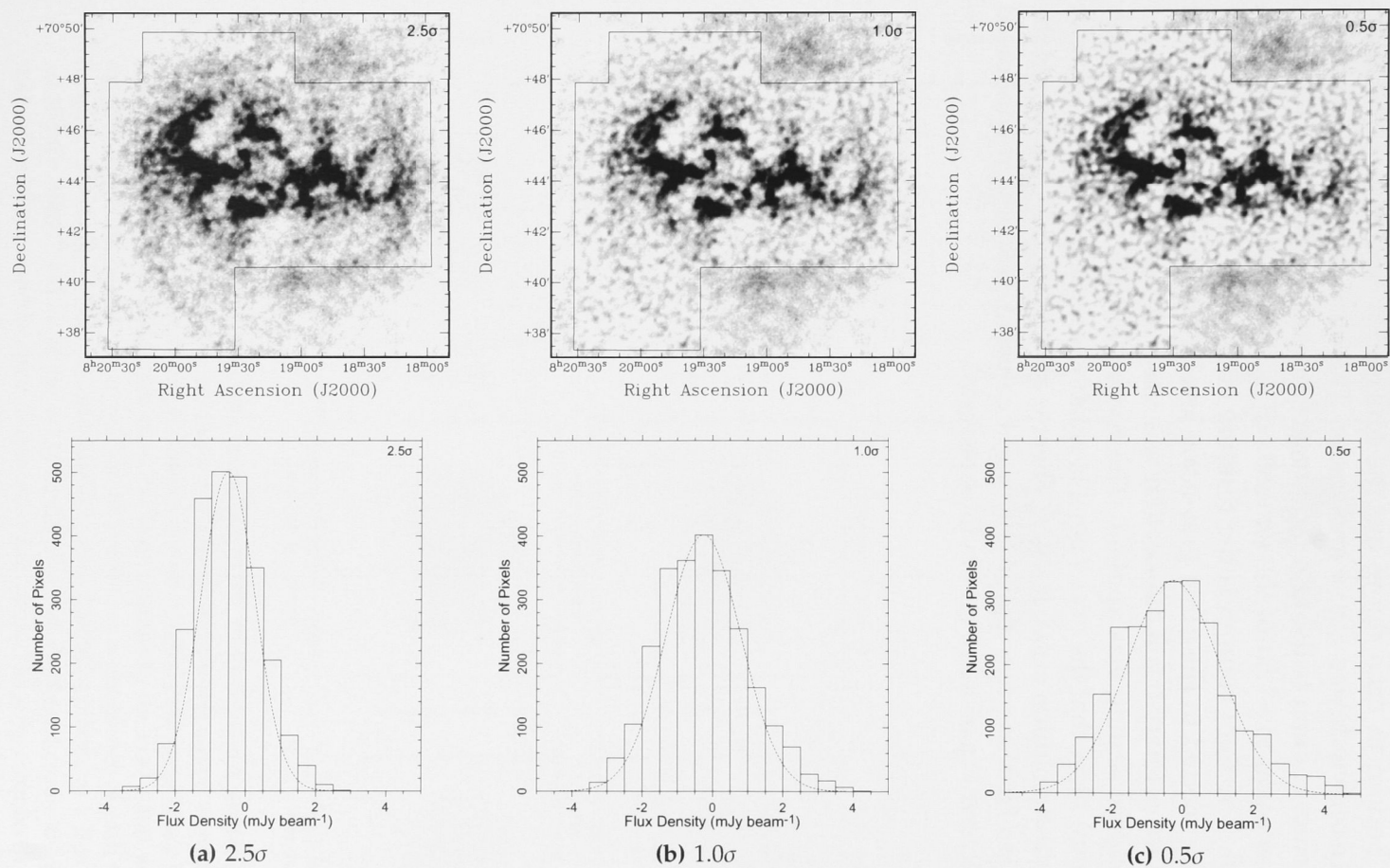
Figure 2.18   Images (top row) of windowed CLEAN to 2.5σ, 1σ and 0.5σ for a channel for the galaxy Holmberg II data. Images are residual flux corrected, unmasked and without primary-beam correction applied. The gray-scale levels run from 0 to 8 mJy beam^{-1}. Also shown are histograms (and the Gaussian fit) of the flux values (bottom row). The histogram values are sampled in a 50×50 pixel box within the cleaned region and where there is no source emission. Images without residual scaling applied were used for the histogram generation.

2.3.2. Channel Map Comparison

In Figure 2.19 on Page 43, we compare the images produced by each algorithm. From top to bottom in each figure are the images for MSCLEAN, AIPS Multi-Resolution CLEAN, windowed CLEAN and CLEAN. The left column is the restored image. The center column is the restored image smoothed to 30″ with a contour plotted at level equal to -1.5σ of the (smoothed) noise to show the effect of the negative bowl. The right column is the residual image. For each column, all of the images are plotted to the same gray-scale levels. Data without masks and not corrected for primary-beam attenuation was used. For CLEAN and windowed CLEAN, no residual scaling was applied. The contours in the smoothed images (middle column) show that the CLEAN bowl is notably less present for the MSCLEAN and AIPS Multi-Resolution CLEAN images. There is also no trace of emission in the residual images for these two algorithms (right column), while both windowed and un-windowed CLEAN leave an obvious pedestal.
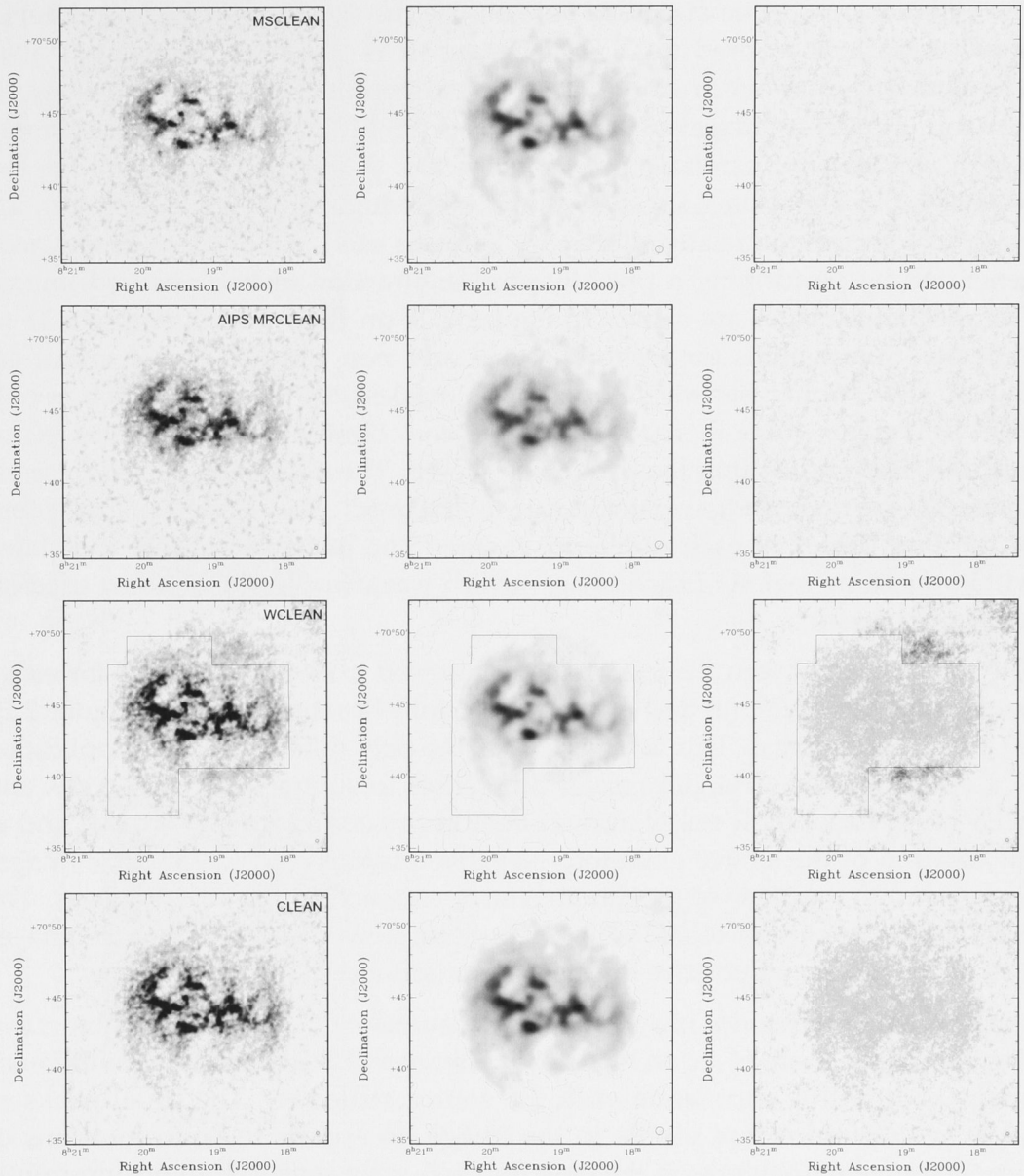
Figure 2.19 The cleaned image (left), smoothed to 30″ (middle) and residual (right) maps for, from top row to bottom row, MSCLEAN, AIPS Multi-Resolution CLEAN, windowed CLEAN and CLEAN, for the galaxy Holmberg II. Images are un-masked and no primary-beam correction has been applied. No residual-scaling has been applied to the CLEAN and windowed CLEAN images. Restoring beams are as marked in the bottom-right corner of each image. For each image in the center column, a (smoothed) contour has been plotted at a flux density level of -0.45 mJy beam^{-1} (-1.5σ of the CLEAN noise). For the windowed CLEAN images and residual, the outline of the window used is also shown in black. The gray-scale levels for the left and right columns run from 0 to 15 mJy beam^{-1} and for the middle column, 0 to 70 mJy beam^{-1}.

2.3.3. Difference Maps

The variations on CLEAN discussed here all use the same principles, but different implementations to produce a final image. It is therefore interesting to see whether these different methods introduce differences in the final images. To that end, difference images of MSCLEAN and AIPS Multi-Resolution CLEAN minus CLEAN/windowed CLEAN have been constructed. A difference image of the two scale-sensitive algorithms, MSCLEAN minus AIPS Multi-Resolution CLEAN, was also made to compare the relative difference between each. All of these images were generated by performing a pixel-by-pixel subtraction of two restored images. The resulting images are shown in Figure 2.20 on Page 45 and Figure 2.21 on Page 46. Subtractions for residual-scaled and non residual-scaled CLEAN are shown. The former has all flux below 2σ masked, as the comparison is only valid in regions where there is source emission. Similarly for windowed CLEAN, only the difference within the window is shown. The differences in the noise are shown for the non-residual scaled CLEAN subtractions. Also shown are histograms of the flux values in each difference image. The histograms were calculated within the same region of each image, which was equal to the window used for windowed CLEAN.

The difference between the CLEAN and windowed CLEAN subtractions for either MSCLEAN (Figure 2.20, (a) and (c)) or AIPS Multi-Resolution CLEAN (Figure 2.21, (a) and (c))is minimal. This is expected, as the only difference is the application of a CLEAN window. The only major differences in subtractions of MSCLEAN and AIPS Multi-Resolution CLEAN minus classical CLEAN are directly around and at the location of the source emission. Negative peaks in these difference images correspond to locations of maximum source emission in the actual images. The AIPS Multi-Resolution CLEAN minus CLEAN/windowed CLEAN difference images also show additional positive difference flux around the negative peaks.

Looking at the difference image of MSCLEAN minus AIPS Multi-Resolution CLEAN (Figure 2.20d), there is an average zero difference flux. Overall, this difference image shows little correlation with the source structure. The small peaks of negative difference flux visible in the image do appear to be at locations of strong source emission as is the case for each scale-sensitive algorithm minus classical CLEAN, but the extent of such differences is much smaller than in the latter difference images. Both scale-sensitive algorithms are therefore performing a similar clean process (*i.e.,* choosing components of similar strength size and location). But where there is compact, high peak flux emission present, the scale-sensitive algorithms and classical CLEAN diverge in their processing techniques. This difference leads to greater total flux recovery for scale-sensitive algorithms, as shown in the previous sections.
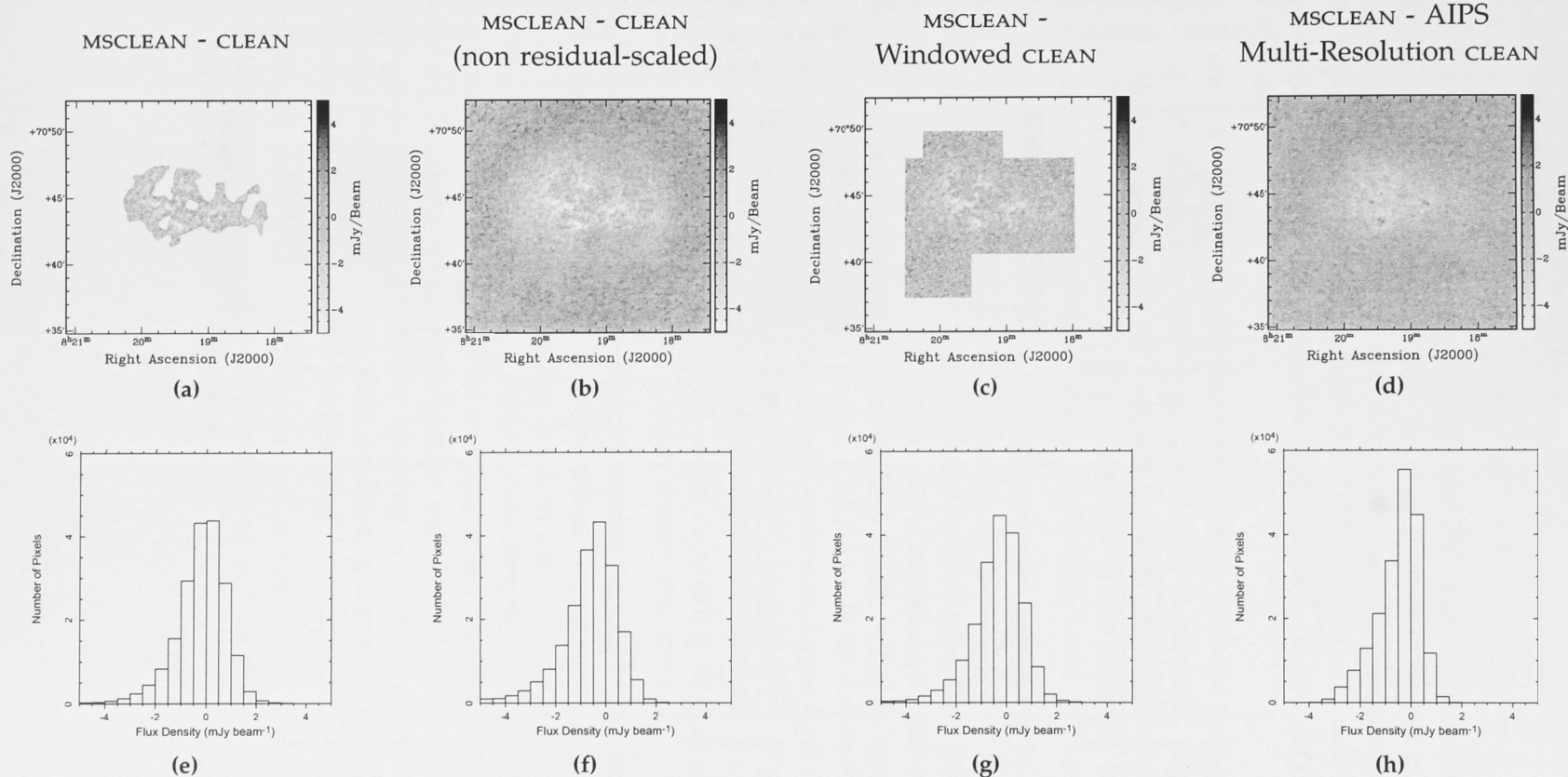
Figure 2.20 Difference images (top row) of MSCLEAN minus residual-scaled CLEAN (a), non residual-scaled CLEAN (b), residual-scaled windowed CLEAN (c) and AIPS Multi-Resolution CLEAN (d) for Holmberg II. The original images were corrected for the primary-beam. For residual-scaled CLEAN all flux below 2σ of the rms noise in the MSCLEAN restored image has been masked. For windowed CLEAN, only the difference within the CLEAN window used is shown. Histograms (bottom row, (e) to (h)) of the flux values calculated within the same area of each image and equal to the area inside the window used for the windowed CLEAN are also shown. Gray-scale levels in the images run from −5 to 5 mJy beam^{-1}.
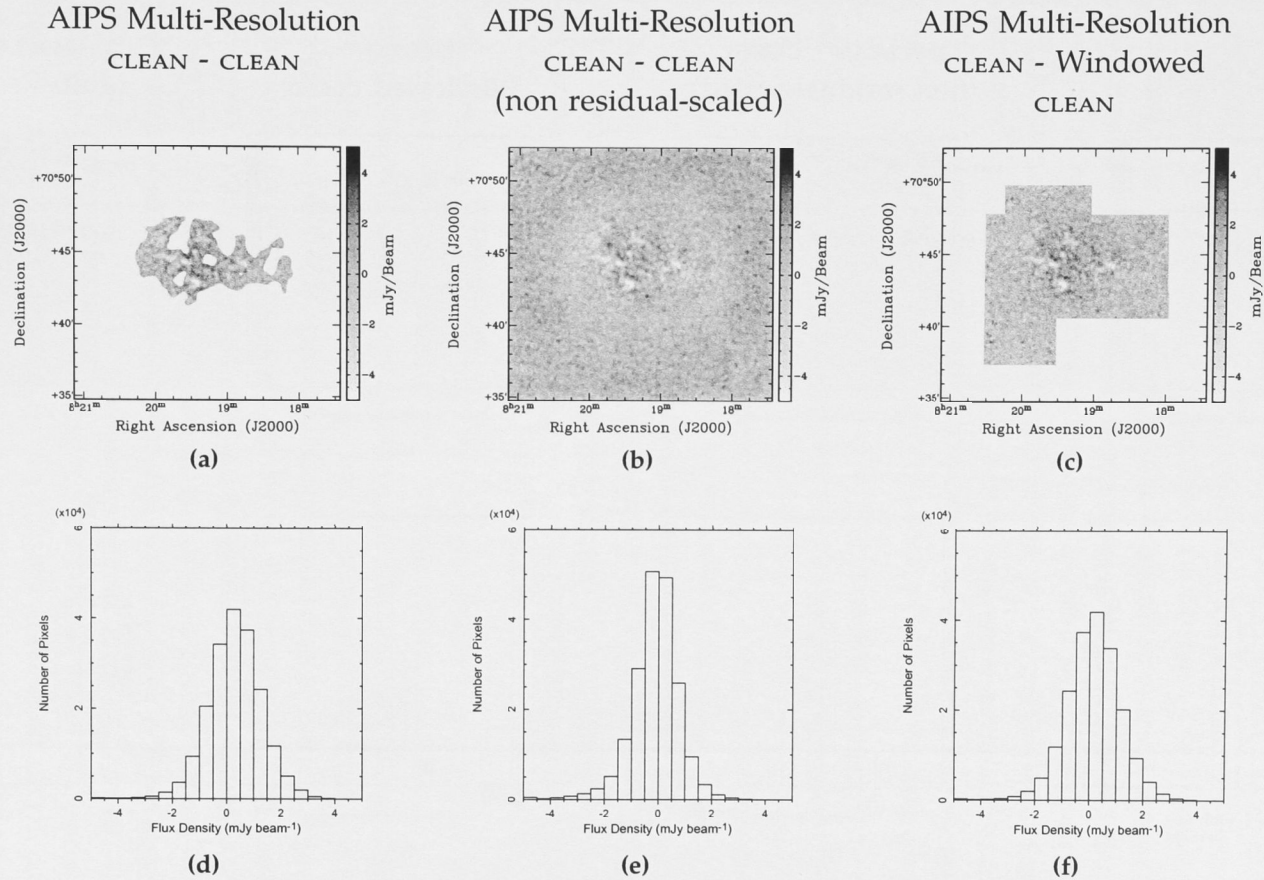
Figure 2.21 Difference images (top row) of AIPS Multi-Resolution CLEAN minus residual-scaled CLEAN (a), non residual-scaled CLEAN (b) and residual-scaled windowed CLEAN (c) for Holmberg II. The original images were corrected for the primary-beam. For residual-scaled CLEAN all flux below 2σ of the rms noise in the MSCLEAN restored image has been masked. For windowed CLEAN, only the difference within the CLEAN window used is shown. Histograms (bottom row, (d) to (f)) of the flux values calculated within the same area of each image and equal to the area inside the window used for the windowed CLEAN are also shown. Gray-scale levels in the images run from -5 to 5 mJy beam^{-1}.

2.4. Summary

This chapter presents a demonstration of the Multi-Scale CLEAN algorithm on a sample of galaxies from THINGS. MSCLEAN is an extension of CLEAN that attempts to overcome some of the short-comings of this algorithm, particularly relating to extended sources such as galaxies. The THINGS data are well-suited to test and compare the performance of CLEAN and MSCLEAN. A summary of the important results follows.

1. MSCLEAN (which here is taken to explicitly include both the CASA as well as the AIPS Multi-Resolution CLEAN implementations) uses fewer iterations than classical CLEAN and can CLEAN down to a low flux threshold much more efficiently than the latter. The algorithm itself is also relatively simple and easy to implement and is currently available in the CASA and AIPS software packages.

2. MSCLEAN removes the bowl and pedestal characteristics that occur when CLEAN is applied to extended sources. In the CLEAN data the extended wings of the dirty beam that are left uncleaned in the pedestal smooth out a lot of the low-level fine-scale structure. MSCLEAN, by significantly reducing the pedestal, reveals this structure more clearly. This leads to better contrast and higher resolution at the lowest flux levels. The CLEAN bowl lowers the apparent flux of all structures within it, due to the negative background it creates. Extended structure usually has a low column density compared to compact structure and so the effect is more pronounced for extended structure. MSCLEAN can greatly reduces this bowl effect, thereby better recovering large-scale structure. The noise characteristics of the final cubes remain the same.

3. MSCLEAN illustrates the importance for residual flux scaling when using classical CLEAN. This need for residual flux scaling arises because classical CLEAN cleans down to a set flux level in the full resolution image, leaving a residual map which is characterized by the dirty beam. The flux in the residuals has to be rescaled by the ratio of the clean beam over the dirty beam area before restoring the CLEAN components back on the residual map. MSCLEAN does a better job in modeling the emission by cleaning at multiple resolutions and cleaning down to the noise on all specified resolutions, leaving virtually no residual and hence removing the need for such scaling.

The added contrast provided by MSCLEAN is useful for a number of astronomical problems involving small-scale structure as will be demonstrated in Chapter 3 for H I holes in the disk of galaxies.

CHAPTER 3

HOLES AND SHELLS IN THE INTERSTELLAR MEDIUM OF THE NEARBY GALAXIES NGC 2403, HOLMBERG II AND IC 2574

T HE typical picture of the Inter-Stellar Medium (ISM) is that of a mixture of gas, dust and cosmic rays encompassing the space between the stars in a galaxy. It is also a violent, turbulent place undergoing constant transformation through the energetic processes including star-formation. Supernovae, gamma-ray bursts, high-velocity cloud collisions and even the nearby environment of the galaxy itself are all believed to shape the ISM into an intricate tapestry of holes, shells and bubbles that defines a complex set of tunnels, networks and cavities of under-densities through the tenuous gas and dust. It is apt then that it has been described as 'the violent interstellar medium' (McCray & Snow, 1979) and the 'cosmic bubble bath' (Brand & Zealey, 1975).

It was in imaging of the Milky Way gas that the first direct observations of the complexity of structure in the ISM were made (Heiles, 1979; Hu, 1981; Heiles, 1984). Coherent, shell-like, predominantly circular structures were observed with diameters mostly around 100 pc, along with a few larger objects bigger than 1000 pc. The expansion velocities (as measured from the surrounding H I gas) were between 5 and 30 km s^{-1} with evacuated masses up to a few 10^7 $M_\odot$ and energy requirements greater than 10^{51} ergs. These measurements suggested an explosive creation mechanism and fingers were immediately pointed at supernovae. Calculations revealed that some structures would require significant numbers of supernovae for their creation, up to a hundred simultaneous supernovae for a single structure, due to their large energy requirements ($> 10^{53}$ ergs).

This was highly improbably and in addition the limitations of the data and the lack of correlation of these structures with objects in other wavelengths (*e.g.*, H α) meant there was no way to pinpoint what the actual progenitors were at the time.

More recent observations have built upon these initial discoveries to find holes and shell-like structures over a wider latitude range in the Milky Way and with more accurate measurements of the properties of each structure found (McClure-Griffiths et al., 2002; Ehlerová & Palouš, 2005). The measurements of the masses, energy requirements and sizes of individual structures observed in these studies constrain the ranges set by Heiles (1984). Additionally, larger structures appeared to exist at large galactocentric radii, while many holes were observed between the spiral arms. This indicated that the dynamical properties of the galactic disk were also important for hole formation, in addition to a still elusive energetic progenitor population.

Shell-like structures such as those found in the Milky Way have also been observed and catalogued in most nearby galaxies within and around the Local Group. The third-person perspective this provides, as opposed to the first-person perspective attained through looking at objects in our own Milky Way, showed clearly the important effect of shell-like structures on the H I distribution of a galaxy. For example, Figure 3.1 on Page 51 shows an integrated intensity map of the Large Magellanic Cloud on which the location of the 23 'super-giant' shell-like structures have been drawn, discovered by Kim et al. (1999). Although they already almost blanket the disk, another 103 smaller shell-like structures were also found in this galaxy; clearly such objects are not formed by isolated or rare events.

Figure 3.2 on Page 52 shows a comparison of a 'shell' structure in our Milky Way with a 'hole' structure in the external, nearby galaxy IC 2574. Despite the differences in resolution and viewing orientation and the completely different galaxy environments, the similarity of the two structures is quite astounding. Attempts have thus been made to compare the properties of the structures in galaxies of varying Hubble type (see Walter & Brinks, 1999; Ehlerová & Palouš, 2005, for example). The result is that there is a building consensus that the forces that lead to the creation of such structures are not unique to the specific environment. However the environment and properties of the host galaxy are sometimes important contributing factors. Terms such as shells, bubbles and holes have been used to describe these structures in the literature. In this study, the term 'hole' is preferred, as such structures appear to be an excavated region in the H I distribution.

As mentioned earlier, the sizes of these holes range from the resolution of the observations (a few hundred parsecs) to a significant fraction of the dimensions of the host galaxy (a few kilo-parsecs). Most studies find objects which have tunneled through the H I disk, forming vertical 'shafts' or 'chimneys' (to use
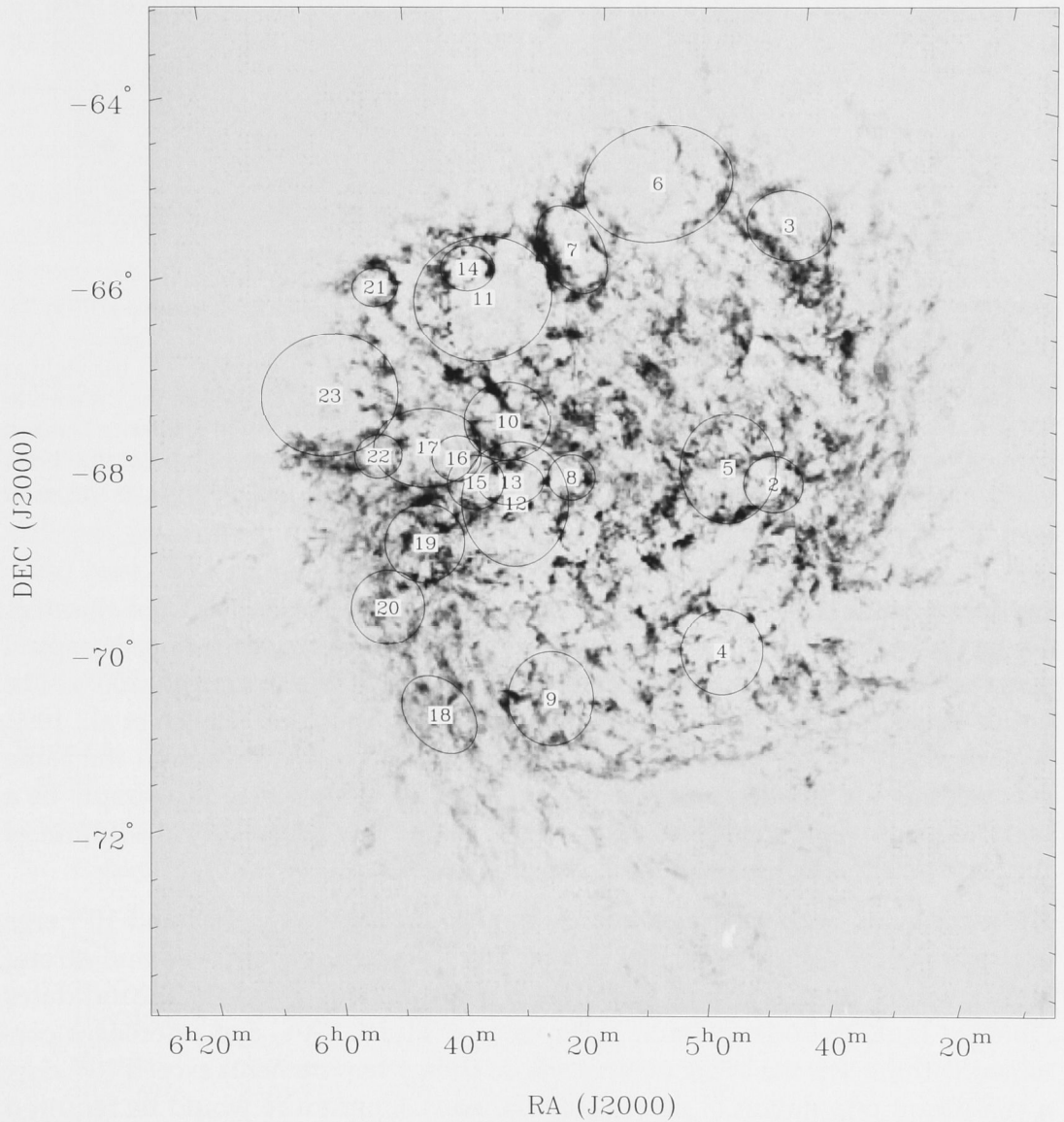
Figure 3.1 An integrated intensity map of the Large Magellanic Cloud showing the location of the 23 'super-giant' shell structures taken from and discovered by Kim et al. (1999). Considering the additional 103 'giant' shell structures found, the H I disk is almost completely covered by shells, which indicates that they are not formed by isolated or rare events, and that they clearly have a large impact on the structure and properties of the ISM.

51
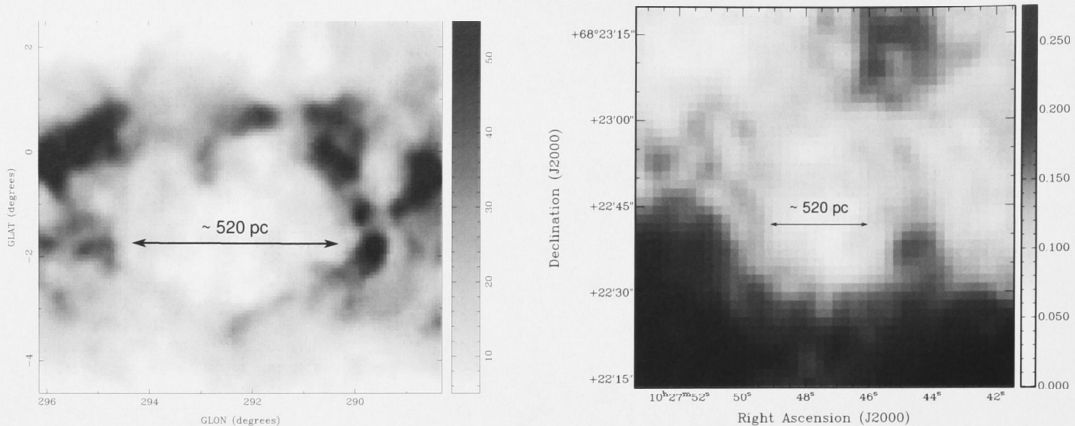
Figure 3.2 Channel maps showing the similarity of hole and shell-like structures within the Milky Way and the galaxy IC 2574. On the left is a channel map of the GSH 292-01+55 'shell' structure discovered by McClure-Griffiths et al. (2002) in the Milky Way. On the right is 'hole' 9 discovered by Walter & Brinks (1999) in the galaxy IC 2574. Despite the differences in resolution and viewing orientation between the two images, the visual similarity between the structures is astounding. The observed and derived properties of these 'shells' and 'holes' also show good agreement between those found in other galaxies and our own, as shown by the size of the structures as marked in each image.

the terms from the literature) with sizes equal to the scale height of the disk. Generally, there is a dominance of smaller structures, particularly in spiral galaxies (Brinks & Bajaja, 1986; Deul & den Hartog, 1990; Boomsma, 2007). The larger structures, so-called 'super-shells' and 'super-bubbles' (Puche et al., 1992; Kim et al., 1999) are generally believed not to have formed through the same processes as the smaller, more numerous structures. They may just simply be a blending of several smaller structures, due to the low contrast or resolution of the data (Walter & Brinks, 1999; Boomsma, 2007).

For most holes, with estimated energy requirements between 10^{51} and 10^{53} ergs and expansion velocities in the 5 to 30 km s^{-1} range, supernovae and strong stellar winds from a young star cluster are the likely progenitor candidates (Tenorio-Tagle & Bodenheimer, 1988; van der Hulst, 1996, and references contained within). For the larger objects, whose energy requirements exceed 10^{53} ergs, a significant population of nearly simultaneous supernovae would be required to trigger their formation, an implausible occurrence. For such objects, propagating star-formation, with successive generations of supernovae and stellar winds slowly evacuating a large hole could explain these structures (Oey et al., 2005). Supernovae are therefore the accepted (if yet to be shown without doubt) progenitor for the majority of holes. In contrast, some studies have proposed high-velocity cloud in-fall (Tenorio-Tagle & Bodenheimer, 1988), ram pressure from galaxy-galaxy mergers (Bureau & Carignan, 2002) or gamma-ray bursts (Efremov et al., 1998; Loeb & Perna, 1998) as the culprits.

It is thus evident that holes are most likely important sites related to star-

formation in the ISM. Their dominance across the H I disk of galaxies also means they have an important role in disk dynamics. Yet there are few good quality hole catalogues in galaxies spanning a range of Hubble types. Such catalogues could provide a wealth of data to mine and compare. This work attempts to contribute to this effort through the addition of catalogues of holes in the three galaxies NGC 2403, Holmberg II and IC 2574. The catalogue for NGC 2403 represents a completely fresh hole catalog, while the new catalogues of Holmberg II and IC 2574 build upon the existing work of Puche et al. (1992) and Walter & Brinks (1999). All three of the catalogues are derived from data created using the Multi-Scale CLEAN (MSCLEAN) algorithm discussed in detail in Chapter 2. The use of such a technique provides additional contrast that allows the probing of these structures in much greater depth than in previous studies. Finally, in addition to conducting an analysis of the properties of the holes in the newly created H I hole catalogues, comparisons are also made to the published catalogues of M31 (Brinks & Bajaja, 1986), M33 (Deul & den Hartog, 1990), M81 (Bagetakos, 2006) and NGC 6946 (Boomsma, 2007). No attempt is made to compare against the catalogued holes in either the Milky Way or the Large and Small Magellanic clouds, all of which contain well catalogued H I holes, because of the significant differences in resolution between the data used in those studies and the data used here. The sample of galaxies compared above covers a range of Hubble types and the data used is of a consistent resolution range that allows for direct and useful comparisons to be made. Properties of each of the galaxies and the studies are listed in Table 3.1 on Page 53.

Table 3.1 The types of the galaxies and the resolution limits of the data compared in this study.

Galaxy	Right Ascension (J2000.0)	Declination (J2000.0)	Type	Size Resolution (pc)	Velocity Resolution (km s^{-1})	Ref.
M31	00:42:44.3	41:16:09	SA(s)b	100	8.2	1
M33	01:33:50.9	30:39:36	SA(s)cd	40	8.2	2
NGC 2403	07:36:51.1	65:36:02.9	SAB(s)cd	125	5.2	3
Holmberg II	08:19:05	70:43:12	Im	200	2.6	3
M81	09:55:33.1	69:03:54.7	SA(s)cd	80	2.6	4
IC 2574	10:28:27.7	68:24:59.4	SAB(s)m	200	2.6	3
NGC 6946	20:34:52.2	60:09:14.4	SAB(rs)c	370	4.1	5

References: (1) Brinks & Bajaja (1986); (2) Deul & den Hartog (1990); (3) This study; (4) Bagetakos (2006); (5) Boomsma (2007)

Firstly, the method of finding holes used in this study, and which is similar to the methods used in other studies, is explained in Section 3.1. This is followed in Section 3.3 by a discussion on distinguishing real holes from under densities in the H I gas and other image artifacts. Having explained the complete identification method, the data used is discussed in Section 3.2. Section 3.4 then details how the various properties of the identified holes are measured. A visual tour of the new hole catalogues for NGC 2403, Holmberg II and IC 2574 and the hole

catalogues of the other galaxies compared follows in Section 3.5. The actual comparison is contained in Section 3.6. Finally, a summary of the results of the comparison is presented in Section 3.7.

3.1. Finding Holes

The holes in each galaxy were found by eye, based on the method used by Walter & Brinks (1999). This method made heavy use of the KARMA software package of visualisation tools (Gooch, 1996). In particular, the KVIS and KPVSLICE tools were extensively used for finding the holes. These tools each provide a different way of looking at the H I disk, which is essential for identifying the physical signature of a hole in a data cube and integrated moment map.

Most holes are found using the integrated H I intensity map, as shown in Figure 3.3. These maps are a summation of all the velocity channels in the data. As such, holes that occupy a large number of channels in the cube (*i.e.,* holes that have blown completely through the disk) show up clearly in such an image. However, smaller holes and holes that occupy a limited number of velocity channels are much harder to see. If the H I flux density in the velocity channels at the spatial location of the hole but in which the hole does not exist is high, this will hinder the visibility of the hole in the integrated intensity map. The integrated intensity map is therefore useful for a quick first pass to identify larger and easy to spot holes and measuring their morphological properties.

For more accurate measurement of the properties and for finding smaller and/or harder to spot holes, the entire data cube must be used. A hole is identified in the data cube through its shape in the two spatial dimensions of right ascension and declination as well as its pattern in the third dimension (usually heliocentric velocity). In consecutive velocity channels, a hole signature appears where the flux wraps around a lower density elliptical or circular region as shown in the images of Figure 3.4 on Page 56. As can be seen, a hole is only usually visible in a limited number of consecutive channels indicating a hole surrounded by H I gas.

Position-velocity (*pV*) and position-flux (*pS*) slices also help identify and categorise hole candidates that are not easily identified directly from viewing the velocity channels. Figure 3.5 on Page 57 shows an example of using the KPVSLICE tool in the KARMA software package to generate *pV* and *pS* profiles of several nearby holes. A hole which is hard to spot in the moment map because of high H I densities (and thus low contrast between light and dark regions) such as hole 103 in Figure 3.5a, is often revealed in the *pV* slice across its location by gaps in the H I intensity profile (Figure 3.5b). In other cases, the *pS* slice shows a much clearer signature, as is the case for hole 90 in Figure 3.5c. Here the presence of a
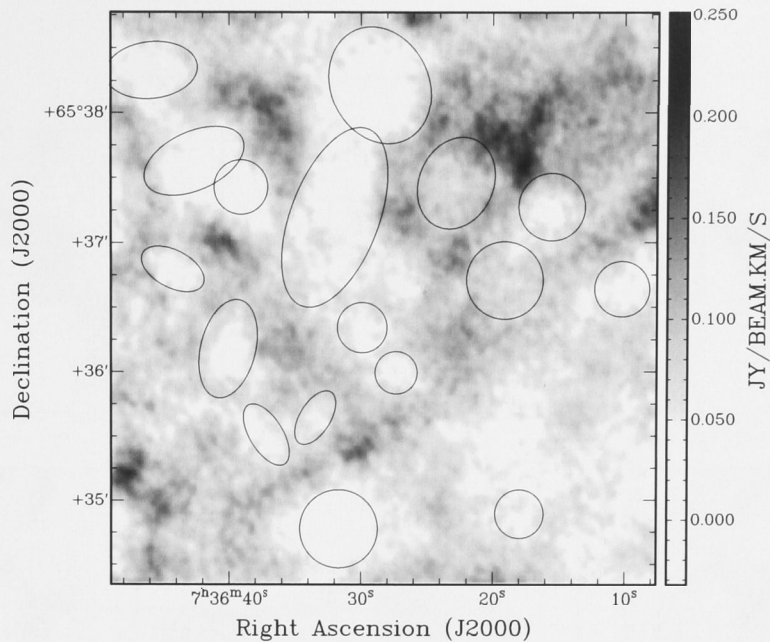
Figure 3.3 A part of the H I integrated intensity map (the moment zero map) of the galaxy NGC 2403, showing the locations of a number of discovered holes, as marked by the black ellipses and circles. With the contrast shown, some of the holes appear quite clearly on the moment map, while several are not clear at all in the moment map. However, they are often much more visible when viewing the individual velocity channels of the original data-cube.

hole is revealed by a dip in the pS profile, whose size corresponds to the faint outline of the hole in the integrated intensity map.

In this study, low signal-to-noise features that were of the order of the size of the beam were generally classified as just noise. Based on visual examination, a structure had to exist in more than four velocity channels as well before considering it. Once a hole is identified, it is categorised into one of three different types as is done in many previous studies (see Brinks & Bajaja, 1986; Puche et al., 1992; Walter & Brinks, 1999, for example). The primary factor defining the hole type is the shape of the hole in a pV cut through the hole centre. A typical example of the three different types are shown in Figure 3.6 on Page 58. A type 1 hole is indicative of a 'total blowout' as there is no receding or approaching side in the pV diagram (first image, Figure 3.6). A type 2 hole is a 'half blowout'; the central structure is offset from the disk, resulting in a concave deformation in the disk as shown in the second image of Figure 3.6. A type 3 hole has a complete expanding shell visible. Such holes appear as a circular or elliptical void inside the disk structure, as shown in the last image of Figure 3.6.

In summary, a hole candidate is first identified in one of two ways:

- By its visibility in the integrated H I intensity map as a contiguous under-density as shown in Figure 3.3.
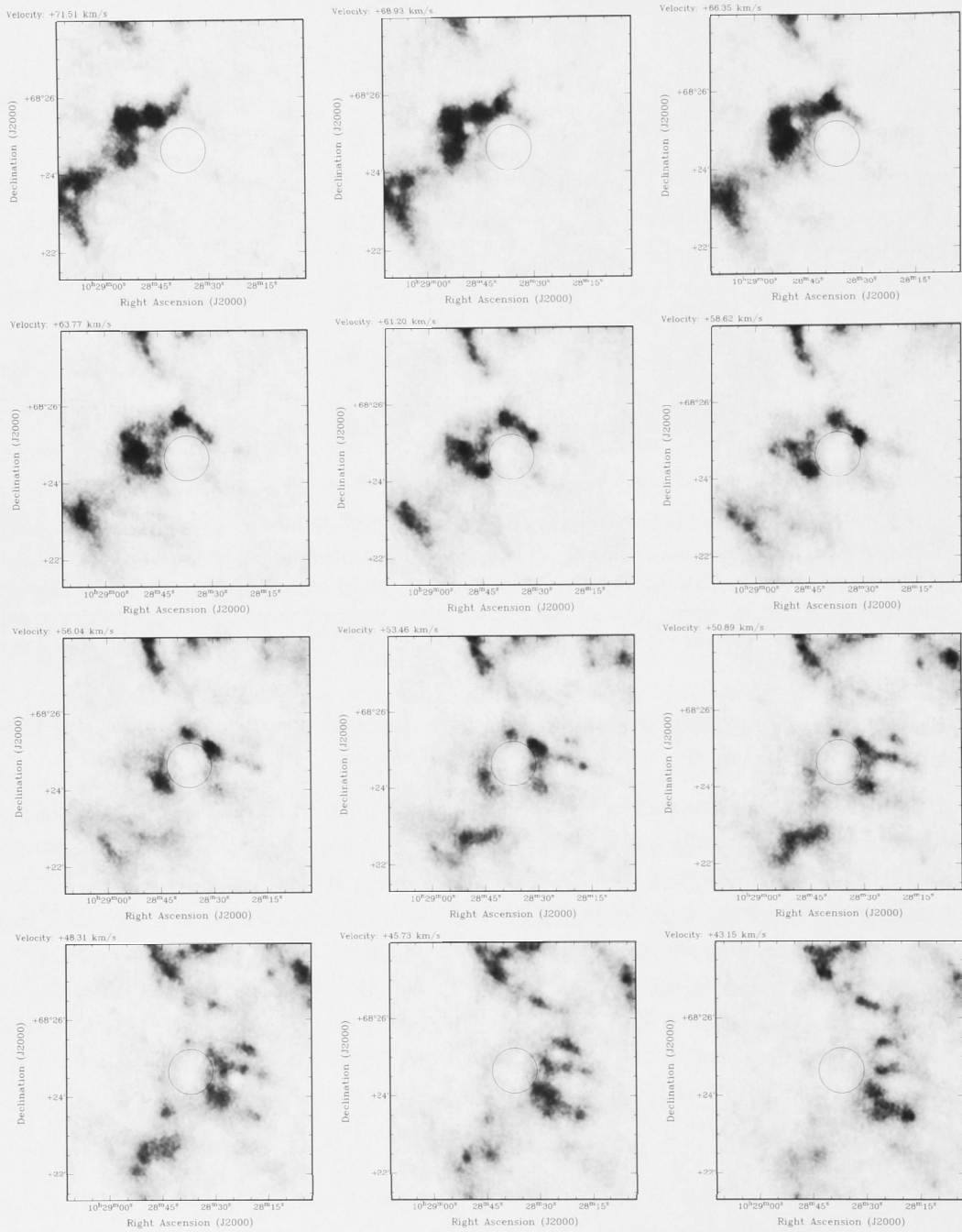
Figure 3.4 Sequential channel maps of a Hɪ hole (white circle) in the galaxy IC 2574, demonstrating how the Hɪ emission wraps itself around the hole region, thus providing a rough estimate of the size and shape of the hole.

(a) Cut across integrated intensity map   **(b)** *pV* slice   **(c)** *pS* slice
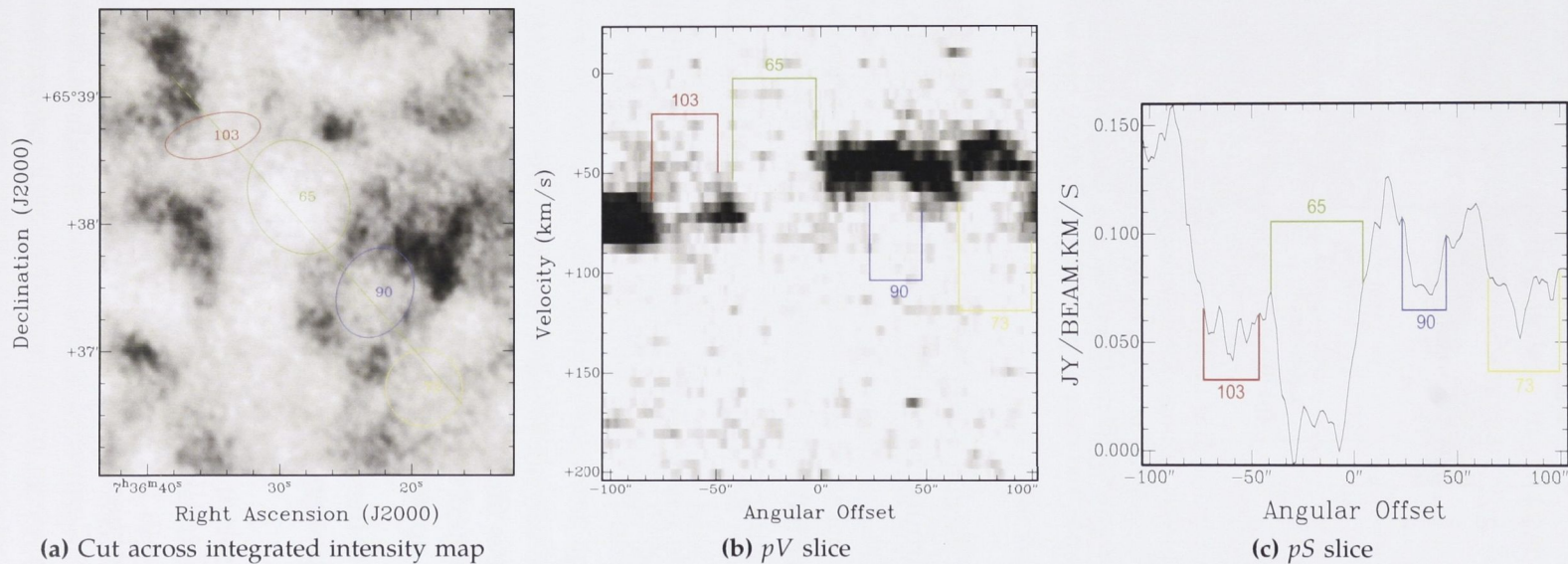
Figure 3.5 An example of taking a *pV* slice across four holes in the disk of the galaxy NGC 2403, with the KPVSLICE tool. (a) The cut is drawn as the diagonal green line across the region of the integrated intensity map shown in (a). (b) The *pV* slice produced by the cut, in which the rough signature of the potential hole candidates can be seen. (c) The cut in *pS* space, where 'dips' in the profile indicate the potential hole candidates as marked.

(a) Type 1   **(b)** Type 2   **(c)** Type 3
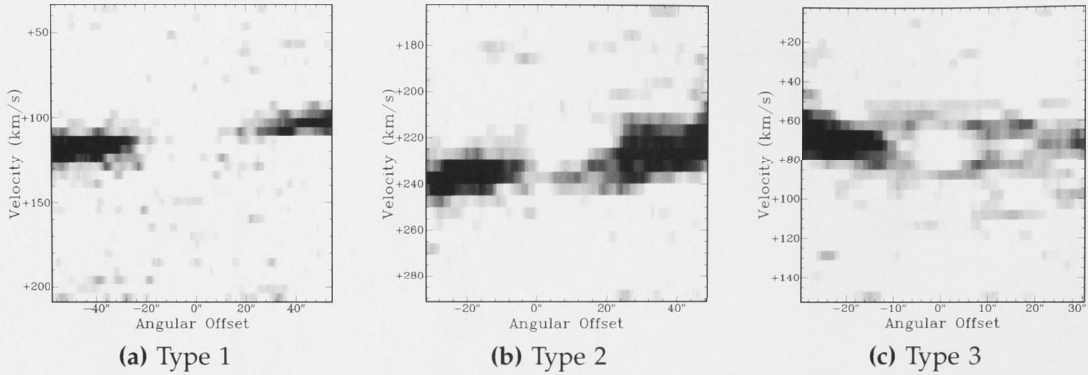
Figure 3.6 Position-velocity (pV) diagrams for a hole of each type from the galaxy NGC 2403. (a) Type 1 holes blow completely through the disk, as shown in the left image. (b) Type 2 holes only blow through one side of the disk making a semicircular depression in the disk, as shown by the 'bowl' structure in the middle image. (c) Type 3 holes are presumed to be still in the process of formation and clear a spherical (or elliptical) hole within the disk, as shown in the right figure.

- By its visibility in consecutive velocity channels in the H I data cube where the H I flux wraps around a circular or elliptical low density region, as in Figure 3.4 on Page 56.

Having identified a potential hole candidate, its size, shape and location is refined through the following steps:

1. For a hole candidate easily seen in the integrated H I intensity map, its properties are directly measured, with the assistance of flux contours where necessary.

2. If the hole candidate can not be seen clearly in the integrated H I intensity map, pV and pS slices are taken across the location of the hole candidate in the H I data cube and the size, shape and location are estimated from the hole candidates appearance in these slices.

3. The hole candidate is then categorised into one of three types as shown in Figure 3.6 by its appearance in a pV slice taken across its location.

3.2. Data Used

For generating the catalogues of holes in each galaxy, the natural-weighted, MSCLEAN data were used. Compared to the robust-weighted data, the natural-weighted MSCLEAN data appears much smoother and less granular, making it easier to see a contrast between light and dark regions in the data (i.e. an under-density where a potential hole candidate might exist). For comparison, a

natural and a robust weighted MSCLEAN integrated intensity map for NGC 2403 is shown in Figure 3.7 on Page 59. Because of this, the natural-weighted data was used exclusively for finding holes. In contrast, many other studies use a combination of both weightings when searching for holes (Bagetakos, 2006; Walter & Brinks, 1999, for example).

(a) Natural Weighting   (b) Robust Weighting
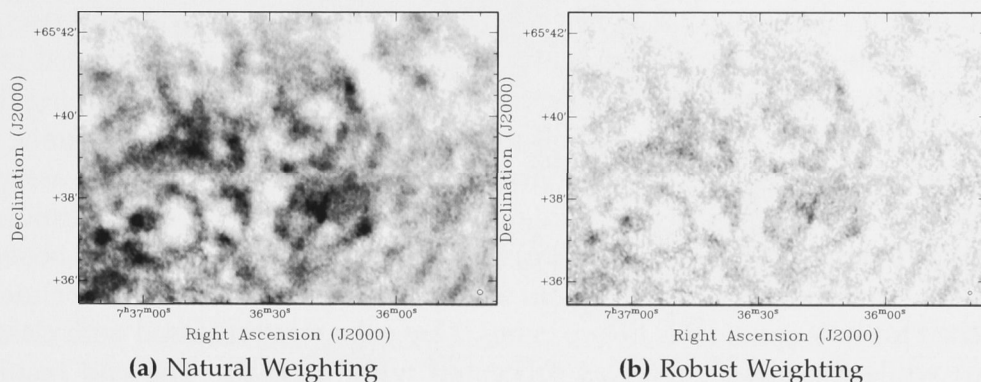
Figure 3.7   A comparison of MSCLEAN natural and robust weightings. Shown is a section of an integrated intensity map of the galaxy NGC 2403. The images have been masked and corrected for the primary-beam. The grey-scale levels run from 20 to 170 mJy beam^{-1} km s^{-1}. Despite being on the same scale, there is more contrast between the high and low flux density regions in the natural weighted map, which assists in the finding of H I holes. Further, to the author, the fine-scale details appear almost identical between both weightings.

For data processed with classical CLEAN, using the robust-weighted data allows probing of the small-scale structure (*i.e.*, small hole candidates) much more efficiently than CLEAN with natural-weighting (which probes the large-scale structure better, see Section 2.2.3 in Chapter 2). As discussed in Section 2.2.8 (of Chapter 2) however, MSCLEAN with natural-weighting appears to probe this small-scale structure on par with CLEAN using robust weighting, while still providing good sensitivity of large-scale structures. Therefore, restricting this study to the natural-weighted MSCLEAN data should not cause a significant handicap to the finding and classification of the smallest H I holes.

3.3.   Verifying Hole Identification

There is no guarantee using the method outlined in Section 3.1, that an identified hole candidate is actually a real hole. The qualities that separate a hole from an under-density in the H I gas are not clear-cut and depend largely on the signal-to-noise of their feature. Therefore the contrast of the data is very important to the identification of holes. Contrast can vary significantly depending on the data, as shown by the differences between data processed by classical CLEAN and MSCLEAN in Chapter 2. Therefore, the identification method used needs to be de-coupled from a dependence on the actual data used in order to ensure

that only real holes are found, false-positives are kept to a minimum and the identification method can be applied to data of differing quality.

To verify the reliability of the method of identification genuine, and to move away from a dependence on the contrast of the data for hole identification, an independent double analysis by two individuals has been conducted. This involved searching for holes in a single galaxy using the same technique, and by two different people, in data cubes processed with classical CLEAN and MSCLEAN. Only the basic observed properties of the hole candidates were catalogued in the test, being the position, size and shape of each hole (the details of assigning these properties, along with many others defined for the final hole catalogues, are discussed in Section 3.4). Also a 'quality rating' between one and ten was assigned. The quality rating defined the confidence that the observer thought a candidate hole was a genuine structure. So a quality rating of 7 meant that the observer was 70% confident that the candidate was real. So each observer independently searched for hole candidates in two cubes. One cube was processed with classical CLEAN while the other cube was processed with MSCLEAN. The end result of the double blind test was four catalogues, two for each observer and imaging algorithm.

There were some significant variations between the catalogues of the two observers, shown in Figure 3.8 on Page 61, which shows the catalogues created from the MSCLEAN data-cubes. However, the agreement between the catalogues, both as regards to size and shape of the holes increased with increasing quality rating. Figure 3.9 on Page 61 shows a plot of the average quality rating assigned versus the ratio of the diameters for holes that were a close match in spatial position (within 10″). There is a convergence of the assigned diameters across both catalogues for a quality rating of around $6 - 7$. This is also shown in Figure 3.10 on Page 62 where the ellipses fitted to various holes are shown for progressively higher quality ratings. That is, with the search method and criteria used in this paper, all candidates found with a quality rating of 6 or above are believed to be real holes.
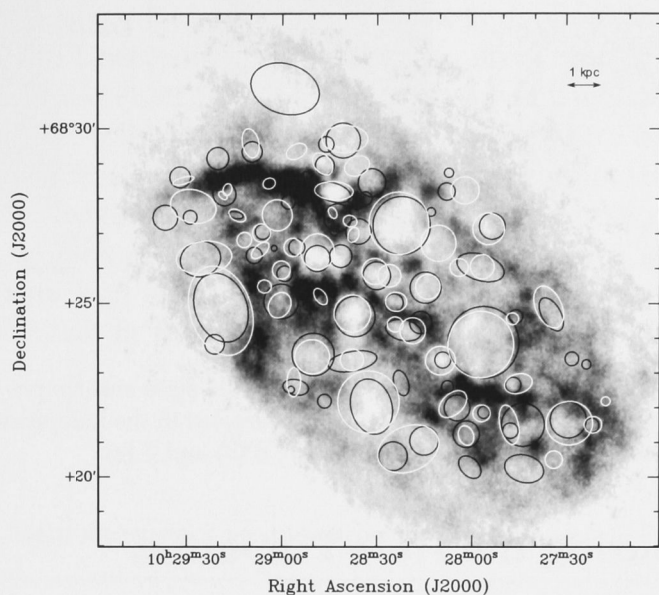
Figure 3.8 MSCLEAN integrated H I map with hole catalog overlays created from MSCLEAN (black) and CLEAN (white) data. The grey-scale levels run from 0 to 251 mJy beam^{-1} km s^{-1}.
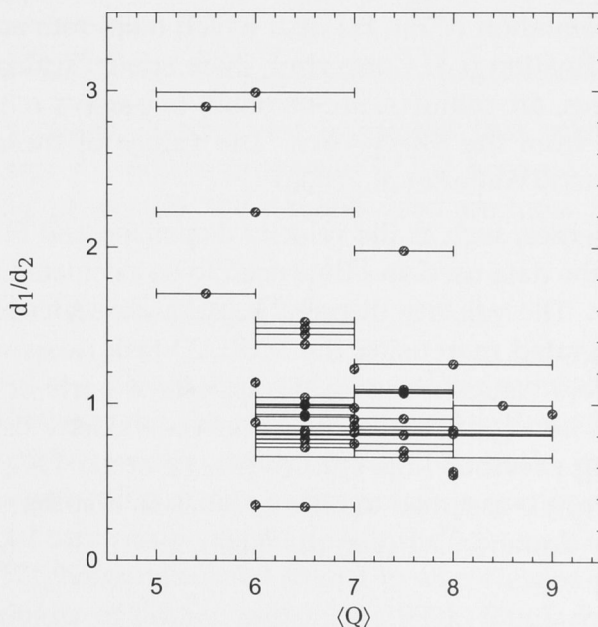
Figure 3.9 A comparison of the average quality ratings assigned to a closely matched hole in both catalogs of the independent double analysis with the ratio of its measured diameters. The error bars in the average quality rating represent the range of the two quality ratings assigned to a hole. The diameters converge at a quality rating of around 6 − 7.

(a) $Q = 5$ **(b)** $Q = 6$ **(c)** $Q = 7$
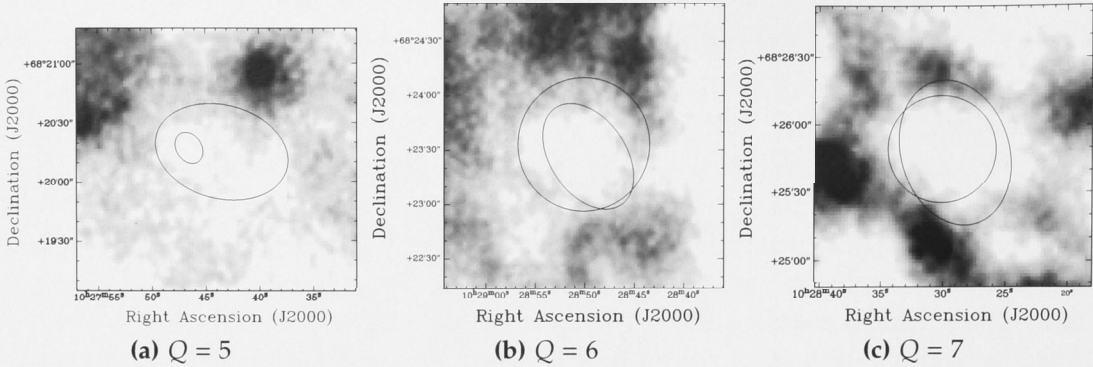
Figure 3.10   Comparison of the agreement between hole sizes and shapes with progressively higher quality ratings for the MSCLEAN catalogues created in the independent double analysis. The quality ratings are (from left to right) 5 (a), 6 (b) and 7 (c).

3.4. Measuring the Hole Properties

3.4.1. Correcting Hole Properties for the Host Galaxy

Several of the measured hole properties are dependent on the parameters of the host galaxy, in particular, the parameters of the H I disk. For the spatial hole properties (galactocentric distance, *etc.*), it is necessary to apply a correction to account for the orientation of the H I disk which takes into account its position angle (θ_ϕ) and inclination (i_ϕ). Converting these spatial scales from distance on the sky (*i.e.*, degrees, arc-minutes, arc-seconds) to parsecs requires the distance (D) of the galaxy from the Milky Way. The values of these properties from THINGS are adopted (Walter et al., 2008).

Other galaxy properties, such as the velocity dispersion and H I disk scale height are dependent on the data used and thus need to be calculated using the MSCLEAN data of this study. The velocity dispersion, σ_{disp}, was calculated by creating a second-order integrated map using the MIRIAD task MOMENT and then taking the median of a few values measured in quiescent parts of the disk. We are assuming there is no significant variation in the velocity dispersion over the H I disk. Following previous hole studies (Puche et al., 1992; Walter & Brinks, 1999), the scale height is assumed to have a Gaussian distribution with a 1σ scale height, h, given by Equation 3.1 (van der Kruit, 1981).

$$h = \frac{\sigma_{disp}}{\sqrt{2\pi G \rho_*}} \tag{3.1}$$

Equation 3.1 assumes the H I gas is isothermal. The density (ρ_*) refers to the total volume density of all gas, stars and dark matter in the disk, calculated from the dynamical mass and volume. ρ_* therefore represents an average value. The

density within the H1 disk is generally much higher than the outer halo and other parts of the galaxy and so the value of ρ_* is doubled to account for this (Puche et al., 1992). Uncertainties in the density do not significantly effect the calculation of the scale height as they are taken to the square root. The dynamical volume is calculated from the simple formula for a sphere by assuming that the galaxy is spherical and all the matter is confined within this sphere with a radius of R_{max}, the maximum disk radius calculated from the rotation curve of the galaxy (see de Blok et al., 2008). The dynamical mass is approximated by Equation 3.2 where V_{max} is the final velocity on the rotation curve. All of the values used are shown in Table 3.2.

$$m_{dyn} = \frac{V_{max}^2 R_{max}}{G} \qquad (3.2)$$

Table 3.2 Galaxy properties used in derivation of the various hole properties.

Property (unit)	Symbol	NGC 2403	Holmberg II	IC 2574
Right Ascension (J2000.0, $hh{:}mm{:}ss$)	α_ϕ	07:36:51.1	08:19:05	10:28:27.7
Declination (J2000.0, $°{:}'{:}''$)	δ_ϕ	65:36:02.9	70:43:12	68:24:59.4
Position Angle (°)	θ_ϕ	123.7	177	55.7
Inclination (°)	i_ϕ	62.9	41	53.4
Distance (Mpc)	D	3.22	3.39	4.02
Disk Radius (kpc)	R_{max}	22	10	10
Scale Height (pc)	h	265	415	509
Velocity Dispersion (km s^{-1})	σ_{disp}	8.7	9.6	9.6
Max. Rotational Velocity (km s^{-1})	V_{max}	135	70	70

In the following sections, symbols for properties that refer to the holes are given the superscript (^{h}). Where properties of the host galaxy are used in the calculation of a hole properties, the symbols used are those found in Table 3.2.

3.4.2. Uniquely Identifying Holes

The first property that a hole is assigned is a unique number for identification. Having identified holes using the method outlined in Section 3.1, the holes are then assigned a number, which usually corresponds to the order in which they were found. For direct comparisons to the previous catalogues of Holmberg II and IC 2574, special care has been taken with the hole numbering in these two galaxies. For IC 2574, holes numbered from 1 to 48 correspond to the same holes found in the catalogue of Walter & Brinks (1999). Similarly for Holmberg II, holes 1 through to 42 correspond to the same numbered holes in the catalogue of Puche et al. (1992). Where holes in these previous catalogues have been rejected in the new catalogues, the hole number has not been used again.

3.4.3. Observed Properties

Position, Size and Shape

The right ascension and declination of the holes (assigned the symbols α^h and δ^h respectively) give the centre co-ordinates of the hole. This is taken as the position within the hole area with the lowest flux density, as observed when using the KVIS tool. The error in the positions is roughly 1.5 arc-seconds in both directions.

To measure the position angle for elliptical holes (assigned the symbol θ^h), contours are plotted on the moment map and the elliptical overlay of the hole is adjusted until it appears to fit the flow of the contours (see Figure 3.11). Then, using KPVSLICE, position-velocity cuts are taken along and perpendicular to the position angle axis to measure the major (a^h) and minor (b^h) axis lengths of the hole. For holes where it is difficult to discern the edges, the FWHM of the pS profile was used instead (see Figure 3.5). For circular holes, $a^h = b^h$ and $\theta^h = 0$.
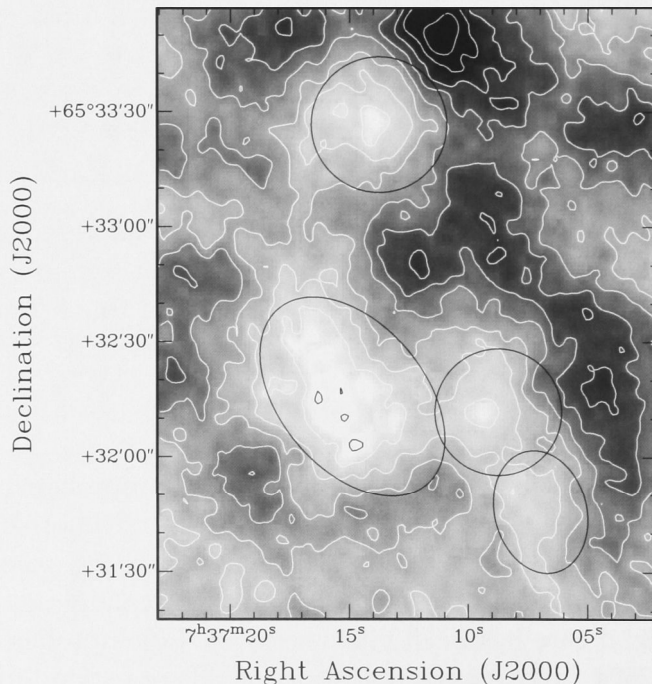
Figure 3.11 Using flux contour levels to constrain the position, size and shape of hole candidates. Contour levels are plotted at arbitrary levels on top of the integrated intensity map as shown and using the annotation feature of the KVIS tool of the KARMA software package, an ellipse is drawn and adjusted on top of the hole candidate location until a good fit to the plotted contours is found.

Velocities

Two velocities are measured for each hole; the heliocentric (V_{hel}^h) and expansion (V_{exp}^h) velocity. The heliocentric velocity is equal to the velocity channel of the data-cube in which the structure of the hole is most prominent. The expansion velocity is calculated differently depending on the hole type. For type 1 holes which are a total blow-out through the disk, there is no way to measure the expansion velocity, and so it is taken as the velocity dispersion of the disk gas (see Section 3.4.1). For type 2 and 3 holes, it is measured from the position-velocity diagrams of each hole, obtained with the KPVSLICE tool. For type 2 holes, it is taken as the velocity difference between the centre of the deformation and where the disk edge would have terminated, had the hole not been there. For type 3 holes, it is half the velocity difference between both sides of the hole. The images in Figure 3.12 on Page 66 demonstrate the measurement of V_{exp}^h for type 2 and 3 holes. The error in the velocities is the three times the width of the velocity channels in each cube, (7.8 km s^{-1} for Holmberg II and IC 2574 and 15.6 km s^{-1} for NGC 2403).

3.4.4. Derived Properties

Diameter

Holes are classified as either circular or elliptical in shape and the parameters that define this shape (diameter for circular holes, major/minor axis and position angle for elliptical holes) can be measured directly. To simplify the calculation of hole properties requiring a diameter (d^h), the geometric mean diameter is used for the elliptical holes, as defined in Equation 3.3 using the measured major (a^h) and minor (b^h) axis of the ellipse. For circular holes, the observed diameter is used. The diameter d^h is limited in accuracy by the resolution of the data, which can be calculated from the FWHM of the synthesised beam of the data. This is ~ 100 pc in all three galaxies.

$$d^h = \sqrt{2a^h 2b^h} \tag{3.3}$$

Age

For measuring the ages of the holes, a simple kinematic age (t^h) is calculated using the hole expansion velocity (V_{exp}^h) and diameter (d^h) (Equation 3.4). This assumes the holes have been expanding for their entire lifetimes with a constant expansion velocity, which implies the age measured is an upper limit on the actual age. For type 1 holes which have blown through the disk, the velocity dispersion of the gas (σ_{disp}) is used, as no expansion velocity can be measured.
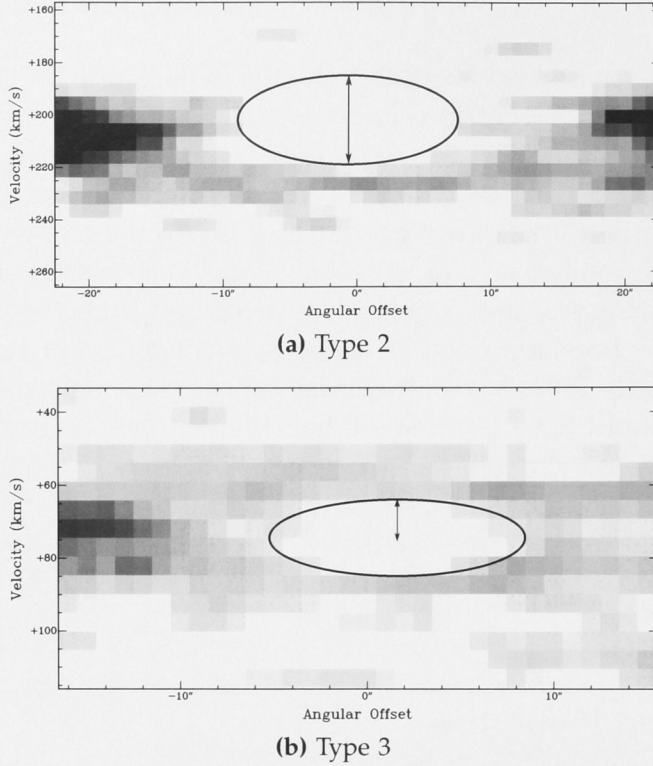
(a) Type 2

(b) Type 3

Figure 3.12 Measuring the expansion velocity (V^h_{exp}) for type 2 (a) and type 3 (b) holes. A pV slice is taken using the KPVSLICE tool in the KARMA software package. The expansion velocity is then estimated as either the half or full width (as marked by the arrows) of the estimated shape of the hole in velocity space (dashed ellipse), depending on the type of the hole. For type 1 holes, which have blown through both sides of the disk and therefore do not show any shell structure, the expansion velocity is set to the dispersion velocity of the H I gas.

As the velocity dispersion of the H I gas is at the lower end of the range of expansion velocities measured for type 2 and 3 holes, the t^h for type 1 holes is a lower estimate. The uncertainty in t^h is $\sim 20\%$.

$$t^h = \frac{d^h/2}{V^h_{exp}} \tag{3.4}$$

Galactocentric Distance

The galactocentric distance (R^h), the distance of the hole from the centre of the host galaxy, relies on a series of corrections to be made to compensate for the inclination (i_ϕ) and position angle (θ_ϕ) of the H I disk of the galaxy. The distance itself depends on the right ascension and declination of the hole (α^h, δ^h) and galaxy (α_ϕ, δ_ϕ) centres and was calculated through Equation 3.5.

$$R^h = \sqrt{(x')^2 + (y')^2} \tag{3.5}$$

where

$$x' = -y \, \cos \, \theta_\phi - x \, \sin \, \theta_\phi$$

$$y' = \frac{y \, \cos \, \theta_\phi - x \, \cos \, \theta_\phi}{\sin \, i_\phi}$$

and

$$x = (\alpha^h - \alpha_\phi) \, \cos \, \alpha_\phi$$

$$y = \delta^h - \delta_\phi$$

Virtual H$\textsc{i}$ Gas Densities

Holes are, by nature, low in H$\textsc{i}$ gas content. The H$\textsc{i}$ column ($N_{\mathrm{H}\textsc{i}}{}^h$) and volume ($n_{\mathrm{H}\textsc{i}}{}^h$) densities of the holes are used for calculating a number of additional derived properties such as, for example the energy requirement to form the hole. Using the current density of a hole would produce a value not reflective of the actual energy input that went into forming the hole, so a H$\textsc{i}$ volume and column density, prior to the evacuation of the H$\textsc{i}$ gas is calculated by using a typical value of the density in the environment surrounding the hole.

In practical terms, this was done using the $\textsc{ellplt}$ task in the MIRIAD software package, using the inclination (i_ϕ) and position angle (θ_ϕ) of the host galaxy (as given in Table 3.2 on Page 63) and over an annulus centered at the galactocentric distance of the hole (R^h) and with a width equal to the diameter of the hole (d^h). The $\textsc{ellplt}$ task calculates the average integrated intensity, $\langle S_{\mathrm{H}\textsc{i}} \rangle$ (in $Jy \ beam \ km \ s^{-1}$) the annulus, which is then used in Equation 3.6 to calculate the virtual H$\textsc{i}$ column density of the hole, $N_{\mathrm{H}\textsc{i}}{}^h$. Equation 3.6 also requires the calculation of the brightness temperature, which is dependent beam size of the data used. As mentioned in Section 3.2, the natural-weighted $\textsc{msclean}$ data were used in this study, and the beam sizes can be found in Chapter 2, Table 2.1 on Page 18.

$$N_{\mathrm{H}\textsc{i}}{}^h = 1.835 \times 10^{18} \, (605.7383/b_x b_y) \, \langle S_{\mathrm{H}\textsc{i}} \rangle \tag{3.6}$$

The virtual volume density can then be calculated from the virtual column density together with the scale height (h) and inclination (i_ϕ) of the H$\textsc{i}$ disk with Equation 3.7. As explained in Section 3.4.1, the scale height is represented by a Gaussian distribution and the H$\textsc{i}$ gas is assumed to be isothermal.

$$n_{\mathrm{H}\textsc{i}}{}^h = N_{\mathrm{H}\textsc{i}}{}^h \left(\frac{h \, \sqrt{8 \, ln \, 2}}{cos \, i_\phi} \right)^{-1} \tag{3.7}$$

It is important to note that using the average flux in an annulus at the galacto-centric distance of the hole produces a rough estimate of the H I densities in the location of the hole before it existed. It should therefore produce a good estimate of the evacuated or consumed H I mass (and in turn the energy requirements) of the hole. It does however ignore asymmetrical and other complex disk H I gas distributions. It further assumes the hole is located vertically in the plane of the disk. For holes that form above or below the disk plane, the density will be higher and Equation 3.7 will overestimate $n_{H_I}{}^h$. The relative error in the H I densities is $\sim$ 20%, based on the error in the average flux measurements.

Volume

To calculate the hole volume (V^h), it is assumed that, for all three types of holes, they are circular and completely evacuated of H I gas. The volume can then be calculated by the equation for the volume in a sphere of diameter d^h using Equation 3.8.

$$V^h = (4/3)\pi(d^h/2)^3 \tag{3.8}$$

Evacuated Mass

The evacuated H I mass ($M_{H_I}{}^h$), or the amount of H I gas that was in the hole location before the hole was formed, can be calculated from the hole volume and virtual H I column density, as in Equation 3.9. As mentioned above, $n_{H_I}{}^h$ measures the virtual H I volume density at the galactocentric distance of the hole. It represents an upper limit of the density, and so the evacuated H I mass calculated here is also an upper limit estimate.

$$M_{H_I}{}^h = n_{H_I}{}^h V^h \tag{3.9}$$

Energy Requirement

To facilitate an easy comparison of the energy requirement of the holes (the initial amount of energy required to produce a given hole) in the new catalogues with existing catalogues, we adopt the formula used by these existing studies and proposed by Chevalier (1974), shown in Equation 3.10.

$$E^h = 5.3 \times 10^{43}(n_{H_I}{}^h)^{1.12}(d^h/2)^{3.12}(V^h_{exp})^{1.14} \tag{3.10}$$

Here, $n_{H_I}{}^h$ is in m^{-2}, d^h in pc and V^h_{exp} in km s^{-1}. Using the hole virtual H I column density does not fully account for the contribution of Helium and heavier elements to the density of the ISM, so a correction factor of 1.36 is

applied to $n_{\mathrm{H\,I}}^h$ in Equation 3.10. The formula also makes the assumption that the holes are expanding, which is an adequate assumption for type 2 and 3 holes, but type 1 holes are most likely stalled (as they have blown through the disk completely and so have nothing to expand into). By replacing the expansion velocity, V_{exp}^h in Equation 3.10 with the velocity dispersion σ_{disp} when calculating the energy requirement for a type 1 hole, Equation 3.10 can be used to estimate the energy requirements for producing type 1 holes as well. However, the velocity dispersion is typically around the minimum expansion velocity of a type 2 or 3 hole, so the energy requirements calculated for type 1 holes using Equation 3.10 are minimum estimates. Finally, as noted by Walter & Brinks (1999), the numerical coefficient of the formula for E^h is actually dependent on the heavy element abundance in the expanding shell, which is dependent on both the galaxy and the location of a hole in the H I disk. The energy requirement is therefore an order of magnitude estimate of the real energy requirements, at best.

3.5. The Sample of Galaxies and their Hole Catalogues

3.5.1. The New Hole Catalogues

The full observed and derived properties for all holes in the catalogues of NGC 2403, Holmberg II and IC 2574 are shown in Tables A.1, A.2 and A.3 (starting on page 111) of the appendices. This study finds 172 holes in NGC 2403, 61 holes in Holmberg II and 70 holes in IC 2574. The previous hole catalogues of Holmberg II (Puche et al., 1992) and IC 2574 (Walter & Brinks, 1999) found 51 and 48 holes respectively. Basic statistics of hole properties for each galaxy are listed in Tables 3.3 to 3.5. For the hole expansion velocity (V_{exp}^h), derived age (t^h) and derived energy requirements (E^h), the statistics both including and excluding type 1 holes (where no true expansion velocity can be measured and the velocity dispersion was used, see Section 3.4.3) are included. Integrated H I intensity maps showing the sizes and locations of all the holes in each galaxy are shown in Figures 3.13 (page 71), 3.14 (page 72) and 3.15 (page 73).

Table 3.3 Basic Statistics of Hole Properties in NGC 2403.

Property		Min	Max	Mean	Std. Dev
V_{exp}^h	km s^{-1}	5.2	20.6	10.9	4.0
V_{exp}^h(ex. type 1)	km s^{-1}	5.2	20.6	14.6	4.7
V_{hel}^h	km s^{-1}	10.1	257.7	138.5	77.1
d^h	pc	159	1817	651	274
t^h	Myrs	6	102	33	18
t^h(ex. type 1)	Myrs	6	66	20	12
R^h	kpc	0.3	15.9	8.3	3.7
N_{H1}^h	cm^{-2}	4×10^{20}	1×10^{21}	6×10^{20}	2×10^{20}
n_{H1}^h	cm^{-3}	0.20	0.47	0.32	0.09
V^h	$10^6 \, pc^3$	2	3000	200	400
M_{H1}^h	$10^4 \, M_\odot$	2	2171	203	270
E^h	10^{50} ergs	4	2820	292	383
E^h(ex. type 1)	10^{50} ergs	4	1750	238	334

Table 3.4 Basic Statistics of Hole Properties in Holmberg II.

Property		Min	Max	Mean	Std. Dev
V_{exp}^h	km s^{-1}	1.0	11.9	7.8	2.8
V_{exp}^h(ex. type 1)	km s^{-1}	1.0	11.9	6.0	3.0
V_{hel}^h	km s^{-1}	125.5	184.8	151.3	15.4
d^h	pc	198	1815	661	371
t^h	Myrs	12	118	46	25
t^h(ex. type 1)	Myrs	13	118	48	30
R^h	kpc	0.2	6.6	3.3	1.5
N_{H1}^h	cm^{-2}	5×10^{20}	2×10^{21}	9×10^{20}	2×10^{20}
n_{H1}^h	cm^{-3}	0.17	0.58	0.28	0.07
V^h	$10^6 \, pc^3$	4	3000	300	600
M_{H1}^h	$10^4 \, M_\odot$	5	3129	270	494
E^h	10^{50} ergs	0.5	4754	364	739
E^h(ex. type 1)	10^{50} ergs	0.5	1035	78	189

Table 3.5 Basic Statistics of Hole Properties in IC 2574

Property		Min	Max	Mean	Std. Dev
V_{exp}^h	km s^{-1}	2.6	20.9	10.1	3.2
V_{exp}^h(ex. type 1)	km s^{-1}	2.6	20.9	10.4	4.1
V_{hel}^h	km s^{-1}	-3.2	115.3	54.0	30.7
d^h	pc	195	2415	798	462
t^h	Myrs	5	123	41	24
t^h(ex. type 1)	Myrs	5	70	31	15
R^h	kpc	0.5	9.7	5.4	2.1
N_{H1}^h	cm^{-2}	6×10^{20}	9×10^{20}	7×10^{20}	4×10^{19}
n_{H1}^h	cm^{-3}	0.16	0.24	0.18	0.01
V^h	$10^6 \, pc^3$	4	7000	600	1000
M_{H1}^h	$10^4 \, M_\odot$	2	4188	335	678
E^h	10^{50} ergs	0.8	6153	499	997
E^h(ex. type 1)	10^{50} ergs	0.8	1336	196	342
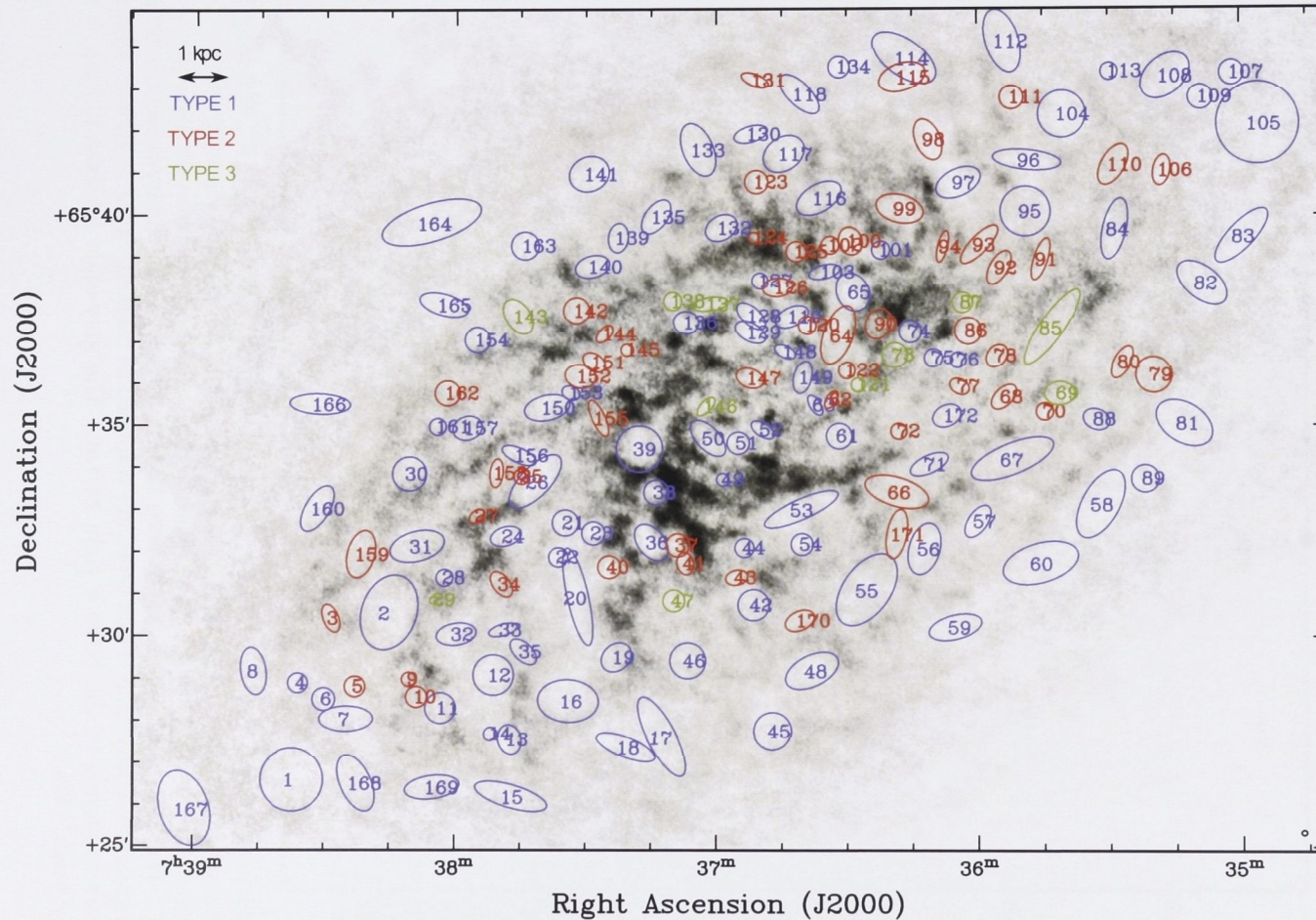
Figure 3.13 The hole catalogue for NGC 2403 on a masked and primary-beam corrected H I integrated intensity map. Hole types are coloured as marked. Scale as shown. Restoring beam is shown in the bottom right corner. The grey-scale levels run from 0 to 225 mJy beam^{-1} km s^{-1}.
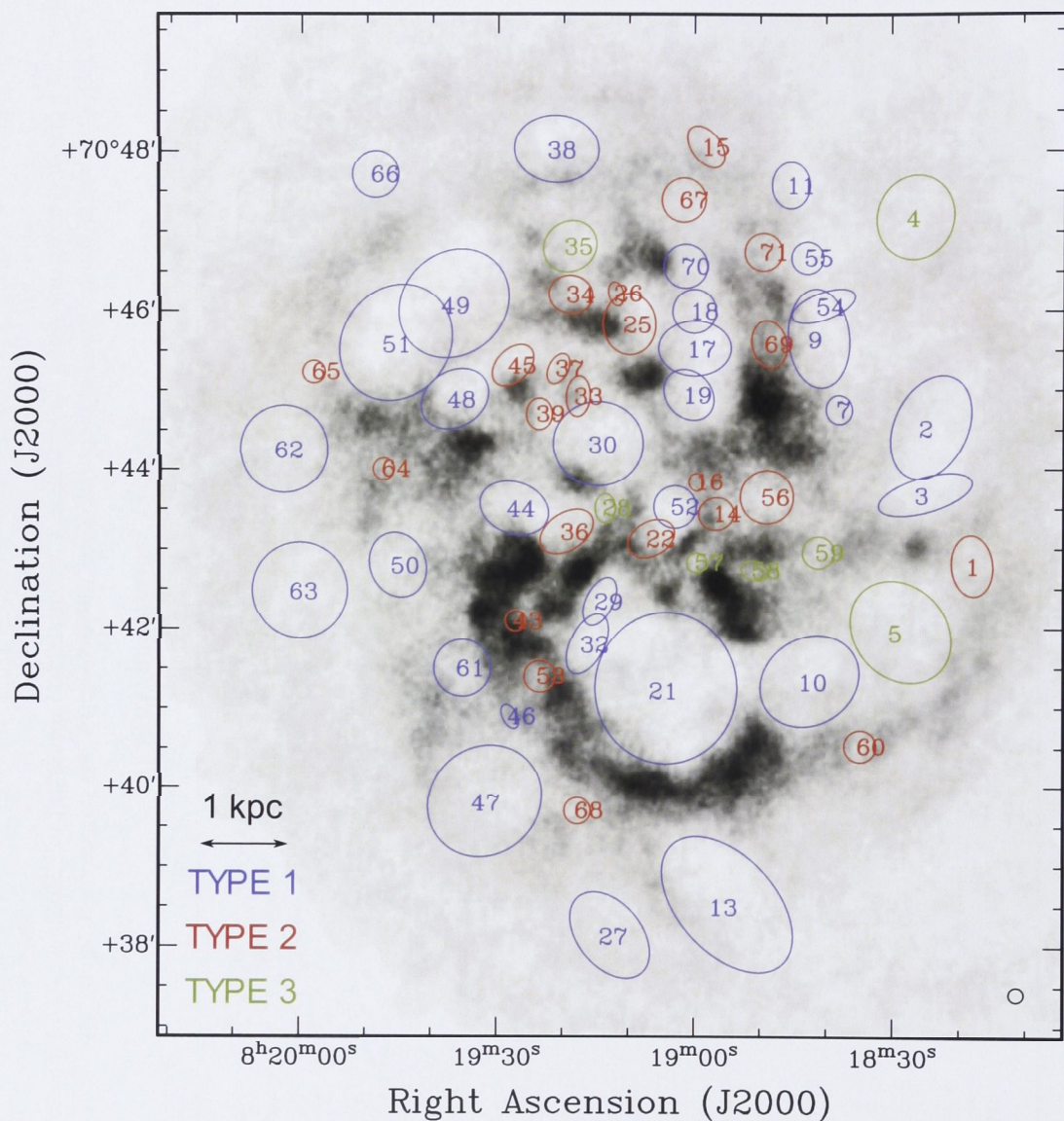
Figure 3.14 The hole catalogue for Holmberg II on a masked and primary-beam corrected H I integrated intensity map. Hole types are coloured as marked. Scale as shown. Restoring beam is shown in the bottom right corner. The grey-scale levels run from 0 to 400 mJy beam^{-1} km s^{-1}.
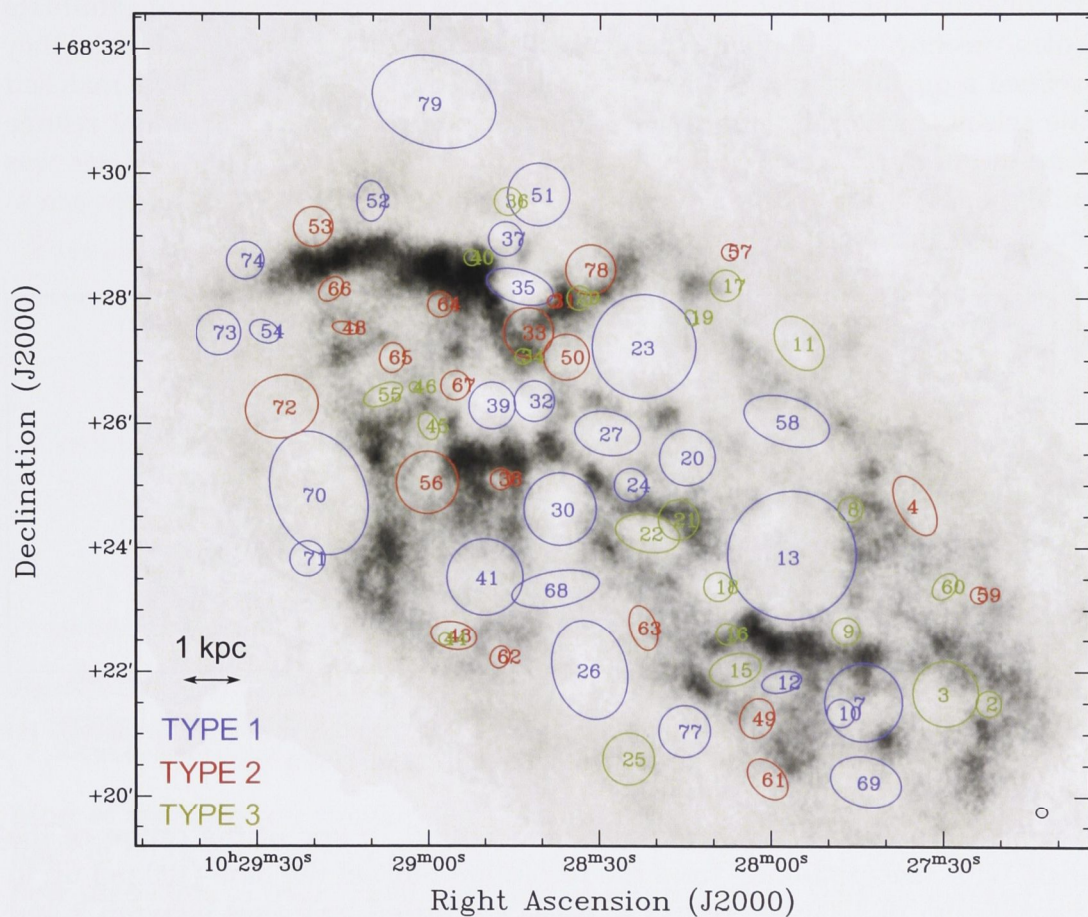
Figure 3.15 The hole catalogue for IC 2574 on a masked and primary-beam corrected H I integrated intensity map. Hole types are coloured as marked. Scale as shown. Restoring beam is shown in the bottom right corner. The grey-scale levels run from 0 to 455 mJy beam^{-1} km s^{-1}.

3.5.2. Existing Hole Catalogues

M31

The H I hole population in the Andromeda galaxy, or M31 was cataloged by Brinks & Bajaja (1986). The observations used in the study had a size resolution limit of 80×120 pc and a velocity resolution of 8.2 km s^{-1}. M31 is located at a distance of 0.77 Mpc. A scale height of the H I disk was calculated as 120 pc. To construct the catalog, the two authors made independent lists of candidate holes, meeting well-defined criteria established beforehand. For each hole, they defined a quality rating Q which indicated how well a candidate hole matched the selection criteria. Through consultation with a third independent referee who did not participate in the search, a catalogue consisting of 141 holes was published. A sketch of the hole catalog, showing the location of the holes across the disk is presented in Figure 3.16.
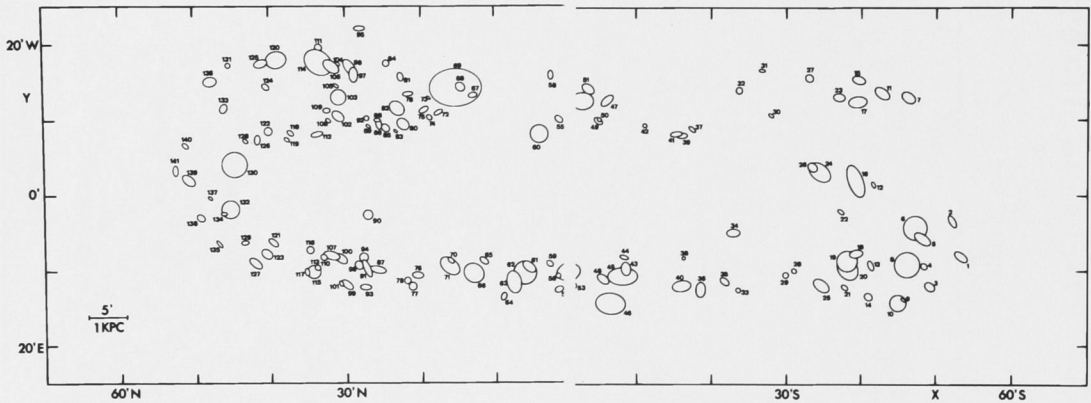
Figure 3.16   The original sketches showing the location of the holes discovered in the M31 H I disk, taken from the original publication of Brinks & Bajaja (1986).

The holes in the catalogue are all found within 10 kpc of the centre of the disk, with sizes spanning from the resolution limit of the data (100 pc) up to a maximum of 1000 pc. Brinks & Bajaja calculated hole ages between 3 and 30 Myrs. For holes that are expanding, they measured expansion velocities up to 8 km s^{-1}. From these observations, it was estimated that the energy requirements to form the holes ranged from 10^{49} to 10^{53} ergs. Type 2 holes, where the shell has blown out one side of the H I disk, make up 50% of the catalogued holes, while type 3 complete shell holes take up 28% of M31 holes, leaving 12% showing signs of complete blow-out through both sides of the disk (type 1 holes).

M33

The hole catalogue for M33 was created by Deul & den Hartog (1990), using the same hole-finding method employed by Brinks & Bajaja (1986), resulting in

148 holes. The data used in the study had a linear and velocity resolution of 40 pc and 8.2 km s^{-1} respectively. The Hi disk scale height was calculated to be 100 pc. M33 is located at a distance of 0.85 Mpc. A diagram showing the locations of the holes across the Hi disk of M33 is shown in Figure 3.17.
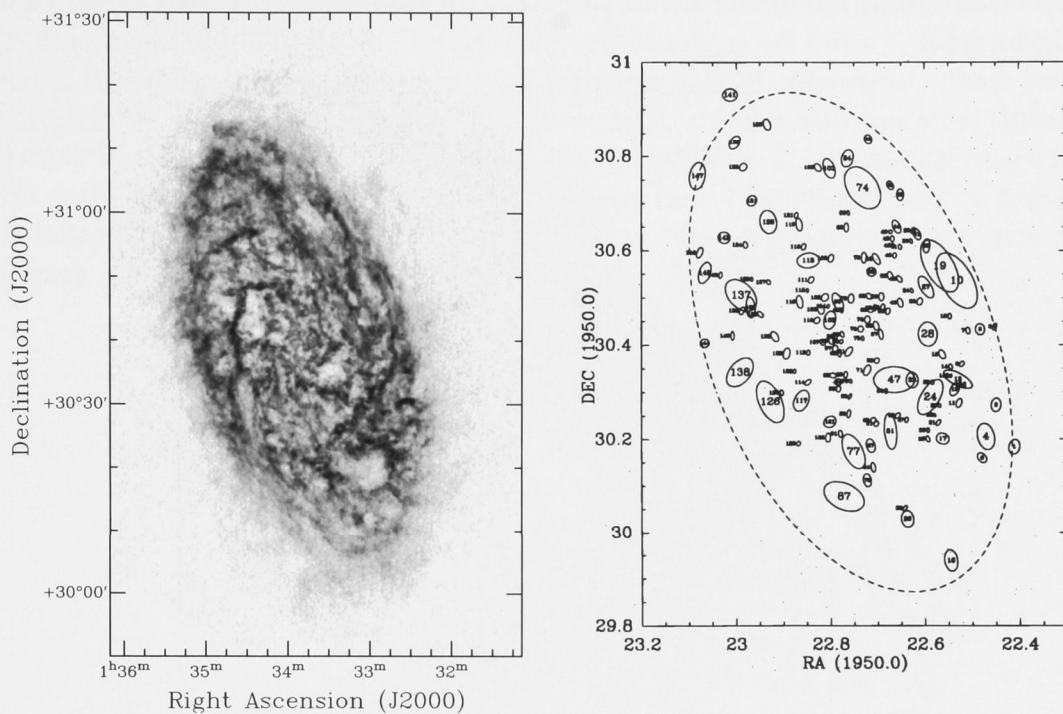
(a) Integrated Hi intensity map of M33

(b) Sketch of M33's Hi hole locations

Figure 3.17 A Hi integrated map of M33 at 20″ resolution from Braun et al. (2009) (a) and the original sketch showing the location of the holes discovered in the M33 Hi disk taken from Deul & den Hartog (1990) (b). Note that the scales on each figure are not the same.

Most of the holes are circular, with diameters detected down to the resolution limit of 40 pc and up to a maximum of 1000 pc, spanning a similar range of hole diameters as M31. Hole ages start at about 2 Myrs, with an average age of 7 Myrs. Expansion velocities up to 20 km s^{-1} were calculated, leading to a slightly larger energy requirement range of 10^{49} to 10^{54} ergs. An interesting correlation was observed between the size of the holes and galactocentric distance, with smaller holes being located in the inner part of the disk and larger holes in the extremities. Additionally, the size correlated with the type of the hole, with diameters decreasing from type 1 holes (complete blow-out) to type 3 holes (complete shell). In terms of hole types, the distribution is 47% type 2, 38% type 1 and 15% type 3.

M81

Bagetakos (2006) contains a hole catalogue for M81, generated following the

method of Brinks & Bajaja (1986), which defines a set of criteria for a hole to match and assigns quality ratings. The data used had a linear resolution of 80 pc. The velocity resolution was 2.6 km s^{-1}. The scale height the H I disk of M81 was calculated to be 100 pc. M81 is located at a distance of 3.63 Mpc. Of the 1212 candidates discovered, 330 are contained in the final catalog, which is shown in Figure 3.18.
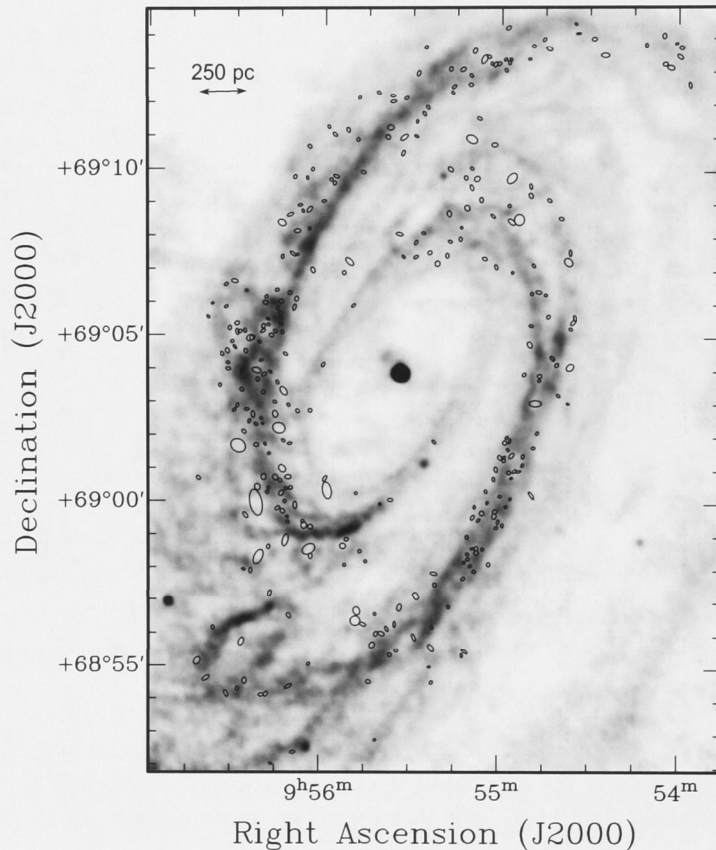
Figure 3.18   The hole catalogue for M81, created by Bagetakos (2006), overlaid on an integrated H I intensity map from The H I Nearby Galaxy Survey (Walter et al., 2008).

The holes in M81 are significantly smaller than the two spirals already discussed (M31 and M33), with a diameter range from 80 to 600 pc. Several very large (super-shell) structures were found, but were not added to the final catalogue due to being located in an inter-arm region. These were assumed to be just large under-densities where the H I gas showed a slight coherence, which the author was not confident were real H I holes. The ages, however, have a similar range to M31 and M33, around 3 to 35 Myrs, with most holes being younger than 10 Myrs. The expansion velocities of the holes range from 8 to 20 km s^{-1}, and the energy requirement to produce a hole runs from a minimum to 10^{50} ergs to a maximum of 10^{52} ergs. There is a slight dominance of type 1 holes in the catalog, accounting for 42% of the holes, followed by 36% type 2 and 22% type 3 holes.

NGC 6946

Although the holes in NGC 6946 were originally catalogued by Kamphuis (1993), this study compares results against the more recent catalogue compiled by Boomsma (2007). The linear resolution of the data used in the study conducted by Boomsma was 370 pc, with a velocity resolution of 4.2 km s^{-1}. It should be noted that these numbers differ from all previous galaxies discussed, which have comparable velocity and linear resolutions. NGC 6946 is also the most distant galaxy in the sample at 5.09 Mpc from the Milky Way. Boomsma calculated a H I scale height of 200 pc. The study uses the hole finding method of Brinks & Bajaja (1986), cataloguing 121 holes. The published catalogue is shown in Figure 3.19.
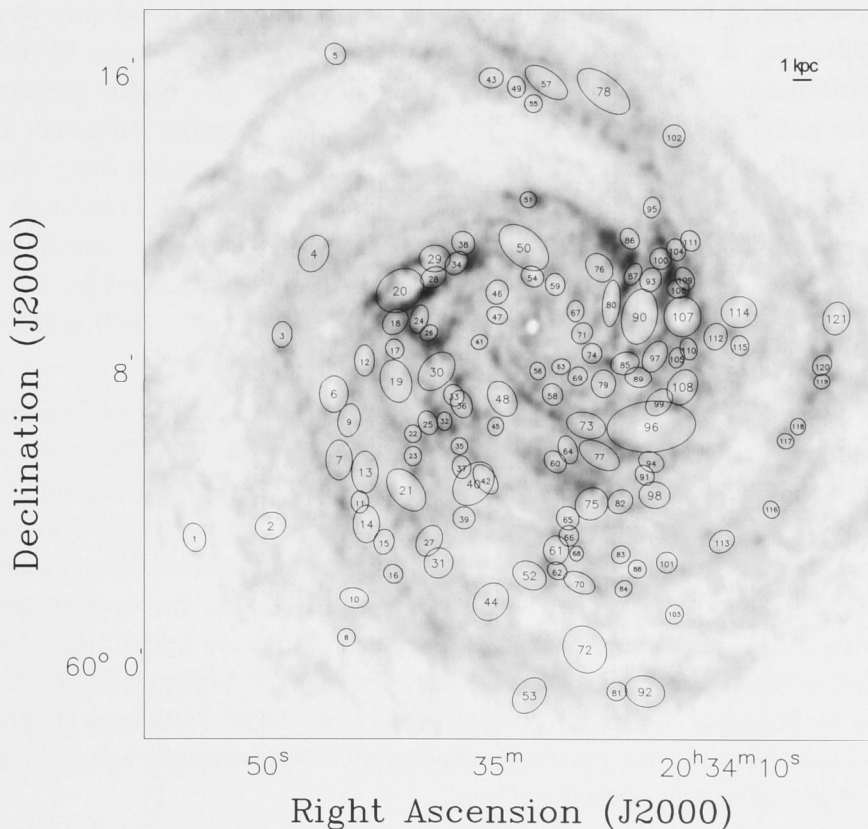
Figure 3.19   The H I hole catalogue for NGC 6946 overlaid on an integrated H I intensity map of the galaxy. Figure taken from Boomsma (2007).

There is a clear asymmetric distribution of hole locations across the H I disk. However, the hole distribution does cover the optical disk, which has a similar asymmetrical distribution. The locations of holes do correlate with high H I column density, even at large galactocentric radii. Hole diameters range from 800 to 3000 pc, indicating the catalogue has not sampled the hole population in sizes down to the resolution limit of the data. Ages of holes in the catalogue are

77

spread between 10 and 60 Myrs. The average expansion velocity is 20 km s^{-1}. To form the holes, energies between 10^{53} and 10^{55} ergs are required. Type 1 holes dominate the catalog, making up 77% of the catalog, followed by type 3 making up 13%, leaving 10% as type 2.

3.6. Analysis of Hole Properties

3.6.1. Hole Coverage and Distribution

A visual inspection of the hole catalogues for NGC 2403 (Figure 3.13 on Page 71), Holmberg II (Figure 3.14 on Page 72) and IC 2574 (Figure 3.15 on Page 73) reveals a good coverage of holes across the disk of each galaxy. A good way to quantify this distribution is by defining a 'hole coverage factor' as done by Boomsma (2007). Boomsma defines the hole coverage as a profile of the percentage of area of the galaxy disk covered by holes with galactocentric distance. The hole coverage with galactocentric distance for the three galaxies from this thesis are shown in Figure 3.20. Also shown on the plots is the H I column density profile (calculated from the masked, primary-beam corrected, natural weighted integrated intensity maps) and the optical radius, R_{25}, marked by the vertical line. Values from the HyperLeda database[11] (Paturel et al., 2003) were used for the optical radius in each galaxy.

For NGC 2403 (Figure 3.20a) there is a significant variation of hole coverage with galactocentric distance, deviating between 10 and 30%. The coverage does not drop off sharply after the optical radius, which would be expected if holes are closely linked with star-formation. But the coverage does correlate well with the column density profile beyond the optical radius. For Holmberg II (Figure 3.20b), the coverage also varies significantly below the optical radius, but stays above a minimum coverage of 30%. Approximately 2 kpc after the optical radius, the coverage begins to drop steeply. For IC 2574 (Figure 3.20c), there is a relatively stable hole coverage (compared to both NGC 2403 and Holmberg II). As with Holmberg II, the coverage stays above a minimum value of 30% and drops sharply after the optical radius.

In addition to the hole coverage plots of Figure 3.20 on Page 79, relative percentage histograms are shown in Figure 3.21 on Page 80. Such histograms show the count of holes (as a percentage of all holes in the galaxy) within a certain bin range of a particular hole property (in this case, the galactocentric distance as a fraction of the optical radius, R^h/R_{25}). This allows an easier comparison of the range of a hole property across all the galaxies, where the total number of holes in each galaxy differs considerably. Plotted in the figure is the distribution for the three galaxies of this study (Section 3.5.1), along with the data from the hole catalogues of M31, M33, M81 and NGC 6946 (Section 3.5.2).
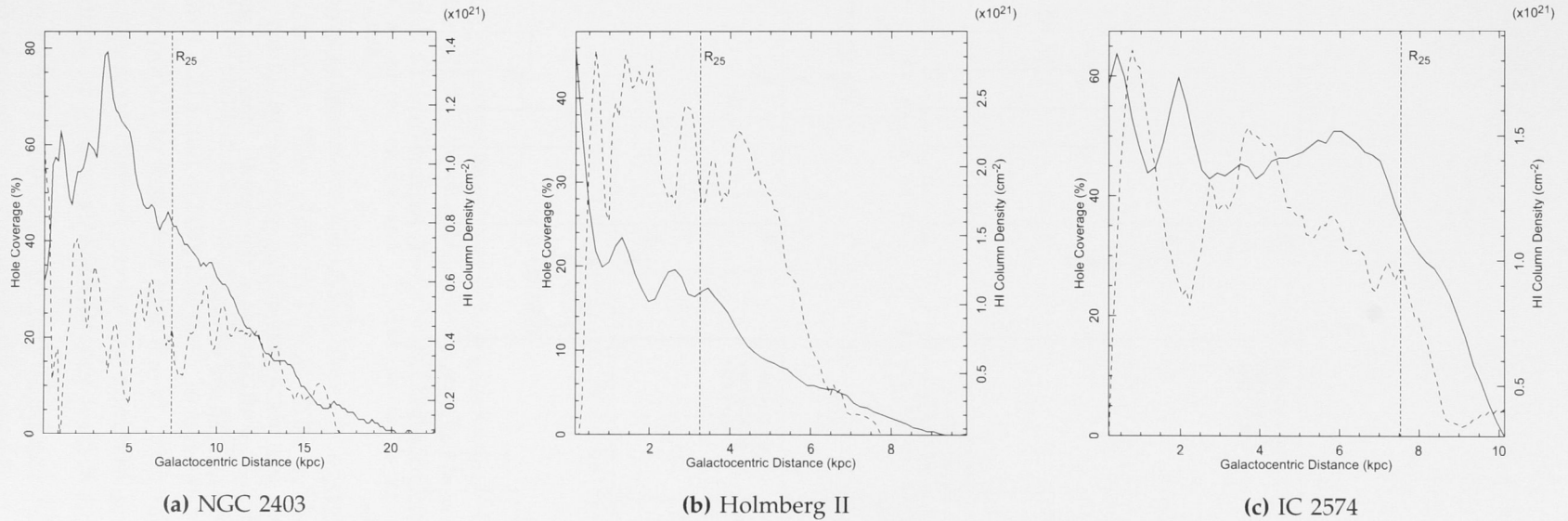
Figure 3.20 The hole coverage factor (dashed line) and H I column density (solid line) profile with galactocentric distance for NGC 2403 (a), Holmberg II (b) and IC 2574 (c). Also shown is the optical radius (R_{25}) marked by the dotted vertical line in each plot.
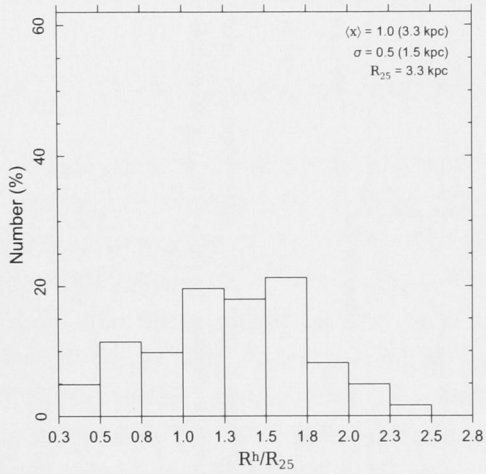
(a) Holmberg II
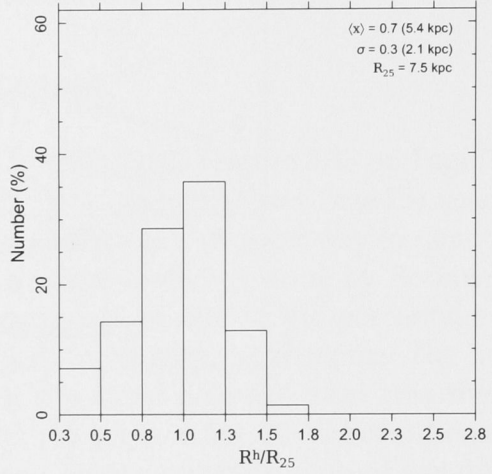
(b) IC 2574
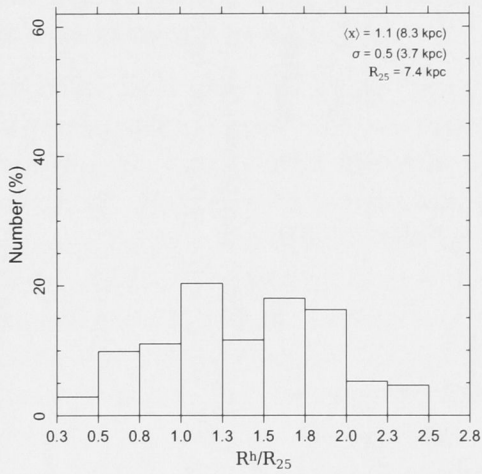
(c) NGC 2403
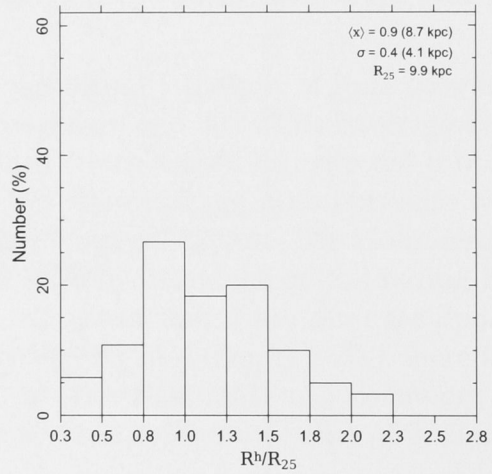
(d) NGC 6946

Figure 3.21   Relative percentage histograms of hole galactocentric distance as a fraction of the disk optical radius (R^h/R_{25}) for all galaxies in the sample. Mean and standard deviation for both R^h/R_{25} and R^h (in brackets) are shown.

(e) M31   **(f)** M33

(g) M81
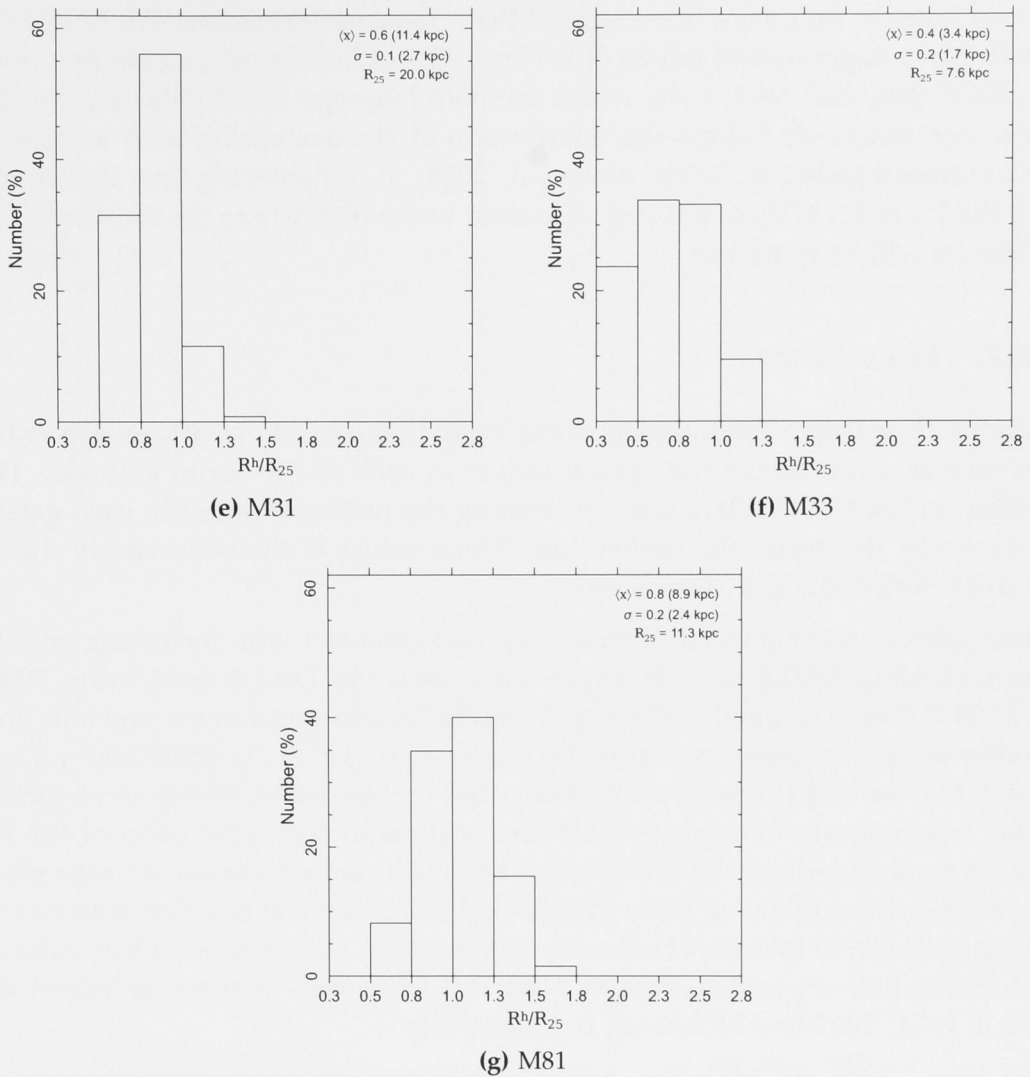
Figure 3.21 Relative percentage histograms of hole galactocentric distance as a fraction of the disk optical radius (R^h/R_{25}) for all galaxies in the sample. Mean and standard deviation for both R^h/R_{25} and R^h (in brackets) are shown *(Figure continued from page 80)*.

For all of the spiral galaxies besides M33, there is a very broad range of hole galactocentric distances. The plots in Figure 3.21 on Page 80 show that the distribution of holes peaks in the centre of the H I disk for all galaxies. For the spiral galaxies in the sample excluding M33, the peak is around 10 kpc. For the two dwarfs (Figures 3.21a and 3.21b), the peak is around 5 kpc. In the latter case, this roughly corresponds to just over half the H I disk radius of these galaxies. In terms of hole types, no distinct trends are observed in any galaxies, all have an equal distribution of galactocentric distance with hole type.

NGC 2403 (Figure 3.21c), Holmberg II (Figure 3.21a) and NGC 6946 (Figure 3.21d) show a significant population of holes beyond the optical radius. For NGC 2403,

81

56% of the holes are at a radius greater than the optical radius (7.4 kpc). Likewise, 54% of holes in Holmberg II are beyond the 3.3 kpc optical radius. For NGC 6946, which has a larger optical radius of 9.9 kpc, 38% of holes exist outside this value. For NGC 2403 and NGC 6946, which are both late-type spiral galaxies, the star-formation efficiency follows the distribution of H_I, decreasing with increasing disk radius (Bigiel et al., 2008; Leroy et al., 2008). It is interesting then that almost half the H_I holes in these galaxies at located in the disk where the star-formation efficiency will be quite low.

3.6.2. Hole Sizes

Figure 3.22 on Page 83 shows plots of the log of hole diameters with galactocentric distance as a fraction of the optical radius in each of the seven galaxies. The resolution limit of the data used in creating the hole catalogues in each galaxy is shown by the horizontal dashed line. Mean values of the two axis are shown by solid horizontal and vertical lines.

Three galaxies show a trend of increasing hole diameter with increasing galacto-centric distance, M33 (Fig. 3.22f, as previously noted by Deul & den Hartog, 1990), NGC 2403 (Fig. 3.22c) and Holmberg II (Fig. 3.22a, also noted in the previous hole catalogue for this galaxy produced by Puche et al., 1992). As discussed in Deul & den Hartog and Puche et al. and as noted by McClure-Griffiths et al. (2002), holes may migrate to or sit in inter-arm regions in the outer parts of the H_I disk of a galaxy, where the H_I densities are lower and expansion can take place more easily (thus allowing holes to grow to bigger sizes). It was also reasoned in Puche et al. (1992) that the H_I density may decrease with galactocentric distance, also aiding hole expansion. Figures 3.20a and 3.20b show that this is indeed the case in NGC 2403 and Holmberg II respectively.

M31 (Fig. 3.22e) and M81 (Fig. 3.22g) both show a more constrained range of hole diameters throughout their respective H_I disks, with at most a smaller proportion of holes beyond the optical radius. This means that in these galaxies, holes are generally only found where H_{II} regions and emission associated with star-formation is found. IC 2574 (Fig. 3.22b) and NGC 6946 (Fig. 3.22d) on the other hand have a wide range of hole diameters across the disk, with no apparent trend of increasing hole size with galactocentric distance.

NGC 2403 and NGC 6946: A Missing Hole Population?

In Figure 3.22, there is a significant gap between the smallest detected holes and the resolution limit for NGC 2403 (3.22c) and NGC 6946 (3.22d). For NGC 2403, the smallest hole diameter is 160 pc while the resolution limit is 125 pc. For NGC 6946, the smallest diameter is 750 pc for a resolution limit of 400 pc. The remaining galaxies all show holes detected with diameters close to the resolution
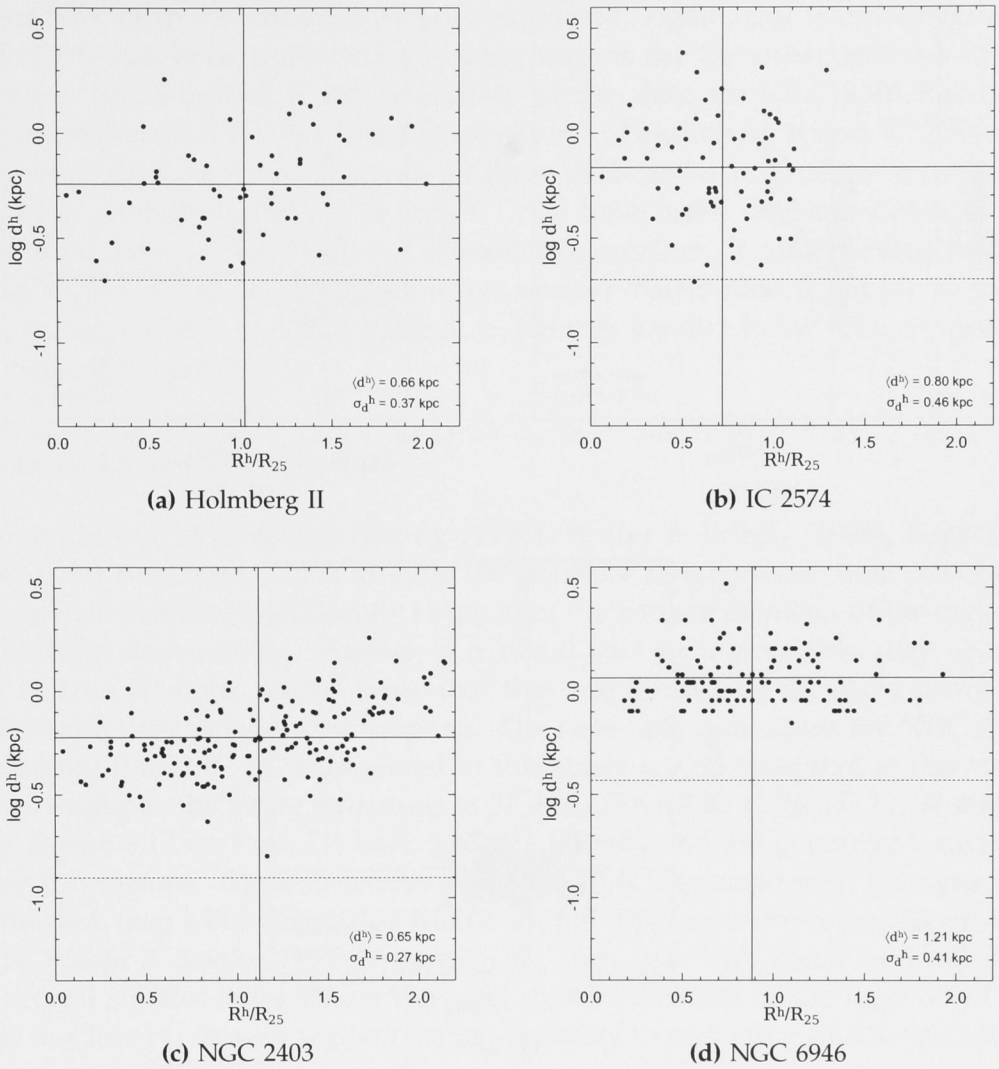
Figure 3.22 The trend of the hole diameters (d^h) with galactocentric distance as a fraction of the optical radius (R^h/R_{25}). The resolution limit of the data is marked with a horizontal dashed line. Mean values of d^h and R^h are marked with horizontal and vertical solid lines. The value of the mean and standard deviation for d^h are also shown.

limit. It is therefore possible that there is significant population of small holes missing from the catalogues of NGC 2403 and NGC 6946 (Boomsma, 2007). For NGC 6946, Boomsma proposed an exponential fit to the size distribution of the hole diameters and calculated that the NGC 6946 hole catalogue only accounts for one-third of the holes in NGC 6946. Performing a similar process on the data of this study for NGC 2403, it is calculated that the current catalogue accounts for only half of the number of holes that can be potentially found in the data. In both cases, this indicates that there is a significant small hole population in these types of galaxies. Given that in the other spirals studied here (M31, M33
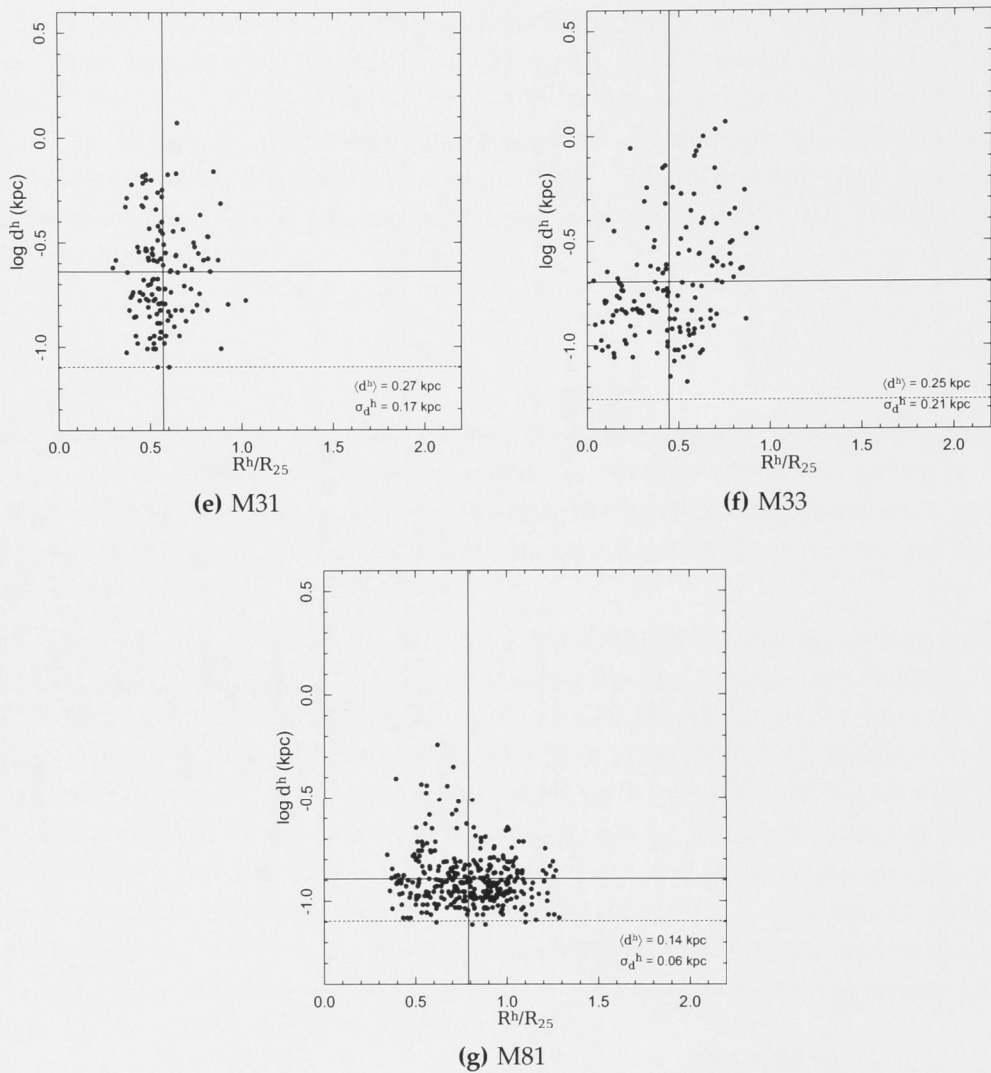
83

Figure 3.22 The trend of the hole diameters (d^h) with galactocentric distance as a fraction of the optical radius (R^h/R_{25}). The resolution limit of the data is marked with a horizontal dashed line. Mean values of d^h and R^h are marked with horizontal and vertical solid lines. The value of the mean and standard deviation for d^h are also shown *(Figure continued from page 83)*.

and M81), the hole population in each galaxy has been probed down to the hole limit, NGC 2403 and NGC 6946 would have the most holes of the entire sample. Hole formation is therefore much more prevalent in these late-type spirals than in either dwarfs or the early-type spirals M31, M33 and M81.

It is difficult to pinpoint what is the exact cause for the discrepancy in small hole detections in both of these galaxies, given the different data-sources and properties. One possibility is that the holes are *physically* absent. This is, however, extremely difficult to prove, given that there is no logical reason as to why the

holes should not be visible in either case. Another possibility is that the sensitivity limits have been systematically under-estimated. Again, this is unlikely, as the sensitivity has been estimated the same way as for the other galaxies in the sample. In particular, if the sensitivity of the data for NGC 2403 has been under-estimated, it follows that the sensitivity of Holmberg II and IC 2574 will have been under-estimated, given all three galaxies have undergone the same processing. Both Holmberg II and IC 2574 have holes detected down to the resolution limit, so it is likely not a sensitivity problem. It could be that there is some aspect of the H I distribution (*i.e.,* spatial distribution, contrast) in these two galaxies which makes it difficult to identify smaller holes. This too would be difficult to quantify.

Notes on Large-Scale Structure

The studies of Deul & den Hartog (1990), Walter & Brinks (1999), Bagetakos (2006) and Boomsma (2007) all note the presence of large-scale hole structures, whose diameters are significantly larger than the average diameter of the majority of holes in each catalog. Further, it is noted that such structures may or may not be true H I holes, in the sense that they are formed by the same processes that shape their smaller counterparts. The new hole catalogues for NGC 2403, Holmberg II and IC 2574 presented in this study are no exception to this trend. As an example, the larger structures in NGC 2403 such as holes 17, 20, 84 and 85 (see Figure 3.13 on Page 71) have a high ellipticity and are generally located in inter-arm regions. These structures are more likely associated with the dynamics of the disk than a bubble created from multiple supernova explosions (Boomsma, 2007; Walter & Brinks, 1999). Alternatively, such structures could be a blending of several smaller holes where the resolution of the data or the location of the hole in a low H I density region restrict the ability to pick out a smaller structures (Boomsma, 2007). Either way, their signature in pV space is more or less the same as a H I hole. As such, we have decided to include these objects in the hole catalogues of each galaxy for completeness.

3.6.3. Hole Ages

Figure 3.23 on Page 86 shows the distributions of derived hole ages in each galaxy. The dwarf galaxies Holmberg II (Figure 3.23a) and IC 2574 (Figure 3.23b) have the greatest mean hole ages. This indicates that H I holes might evolve undisturbed within the H I disk with no dynamical effects acting upon it. A simple way to measure this is by calculating the time for the disk at a given radius to make a complete rotation (Puche et al., 1992). Assuming a flat rotation curve and using the values of V_{max} given in Table 3.2 on Page 63, the rotation timescales are approximately 286 and 661 Myrs at the optical radius for Holmberg II and IC 2574 respectively. Differential rotation will result in shear over shorter time-scales

than the rotation time-scale. For Holmberg II, the rotation timescale measured here is in agreement with the value measured by Puche et al. (1992), confirming the possibility of some shear in the holes in this galaxy. IC 2574 has a larger rotation time-scale and as noted by Walter & Brinks (1999), exhibits solid-body rotation, meaning the holes are truly undisturbed in this galaxy. Therefore for dwarf galaxies, any dynamical forces (if such forces exist) play no major role in hole development in these galaxies.
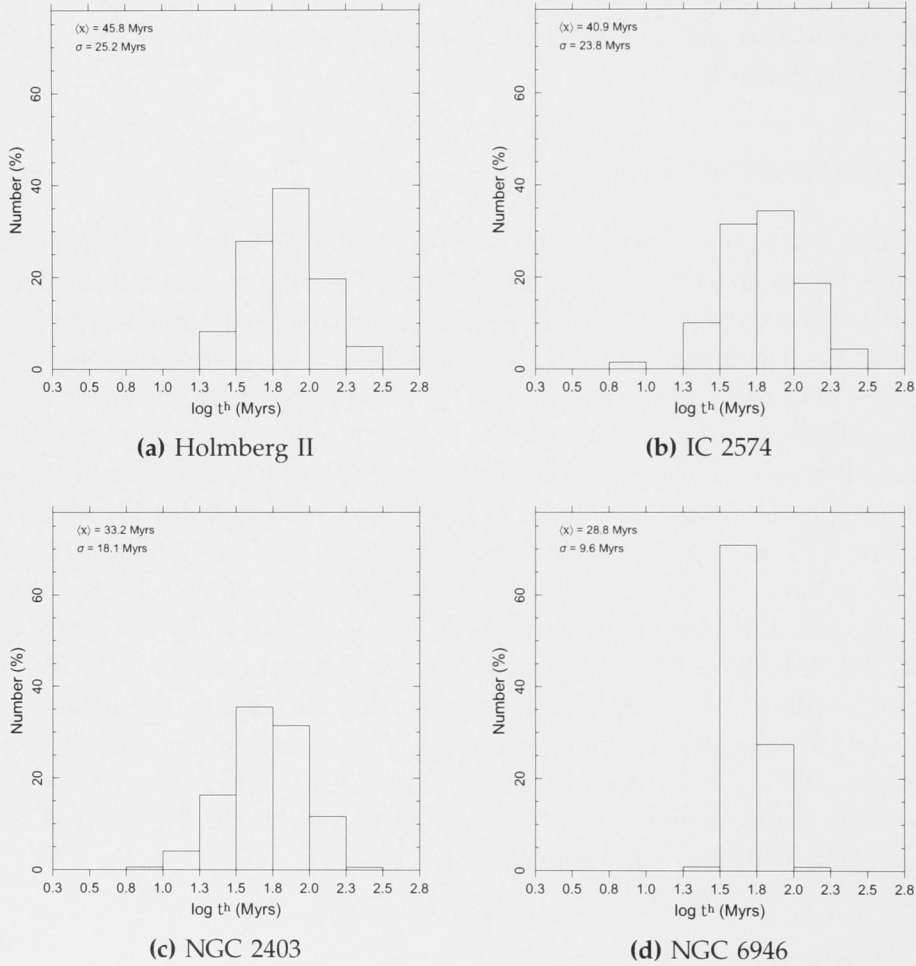
Figure 3.23 Relative percentage histograms of hole age (t^h) for all galaxies. The mean and standard deviation of t^h are also shown.

The early-type spirals M31, M33 and M81 all have very young holes with peak ages between 7 to 13 Myrs. As noted by Brinks & Bajaja (1986); Deul & den Hartog (1990), this time-scale is similar to age-estimates of OB associations. Given the small sizes as well (see Section 3.6.2), this could indicate on-going star-formation in these galaxies. It should be noted though that because of strong dynamical effects (*i.e.*, shear, density waves) in the disks, it would be difficult to find a long-lived and large hole in any of these spiral galaxies. The late-type

spirals NGC 2403 (Figure 3.23c) and NGC 6946 (Figure 3.23d) have much older hole ages. It should be noted that the hole ages for NGC 6946 are calculated with the average expansion velocity of all holes, not the individual expansion velocities as used in the other galaxies (see Boomsma, 2007), leading to a much more constrained spread of hole ages.
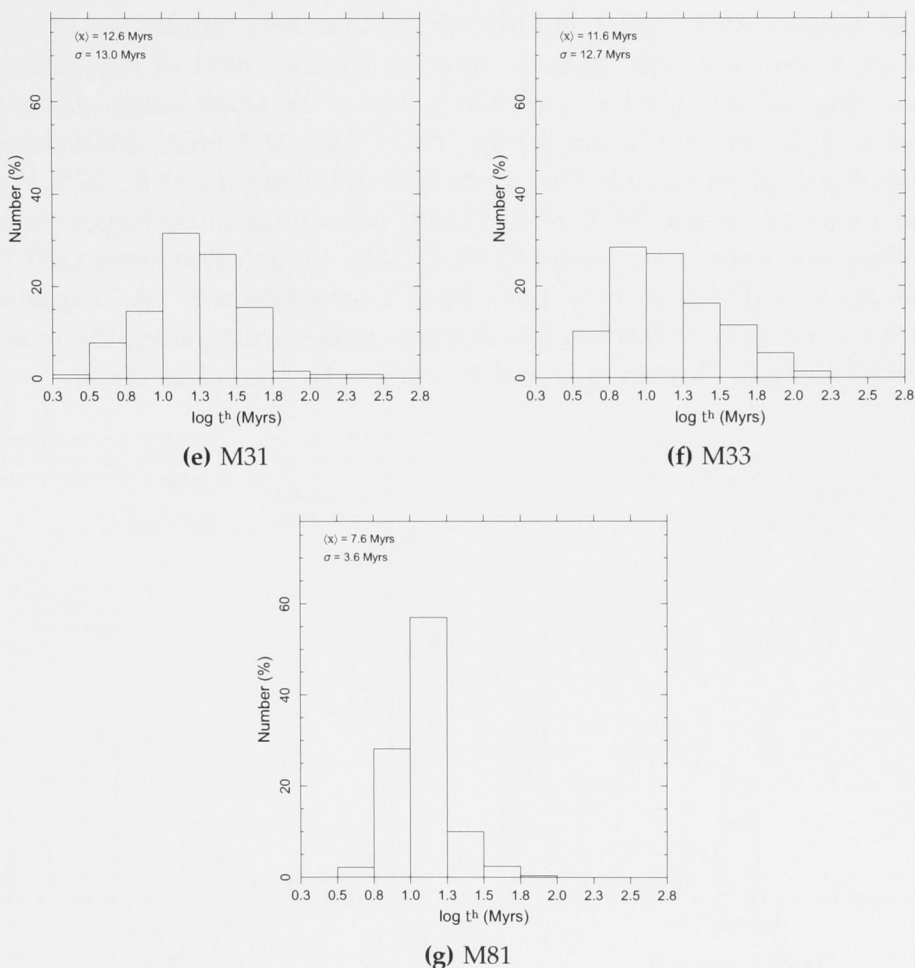
(e) M31

(f) M33

(g) M81

Figure 3.23 Relative percentage histograms of hole age (t^h) for all galaxies. The mean and standard deviation of t^h are also shown *(Figure continued from page 86)*.

3.6.4.   Evacuated H I Mass

As discussed in Section 3.4.4, the measured H I mass of a hole is actually a measurement of the H I mass that would be in the hole region if the hole was not there. This mass is referred to as the evacuated H I mass. Figure 3.24 shows the distributions of evacuated mass in each of the galaxies. The two dwarfs Holmberg II (3.24a) and IC 2574 (3.24b) have a very similar spread of hole evacuated masses. M31 (3.24e) and M33 (3.24f) also have similar histograms, but with much lower evacuated masses than the dwarfs. M81 (3.24g) has a more restricted range of hole masses, most likely due to the small range of holes sizes observed in this galaxy (Figure 3.22g). NGC 2403 and NGC 6946 show hole evacuated mass values equal to the two dwarfs Holmberg II and IC 2574, but with a tighter range of values. NGC 6946 (3.24d) has significantly larger evacuated masses than the other late-type spiral NGC 2403, though Boomsma (2007) notes that the column densities may have been over-estimated. As explained in Section 3.4.4, we believe the column density used in calculating the evacuated mass for NGC 2403, Holmberg II and IC 2574 to be a good estimate.
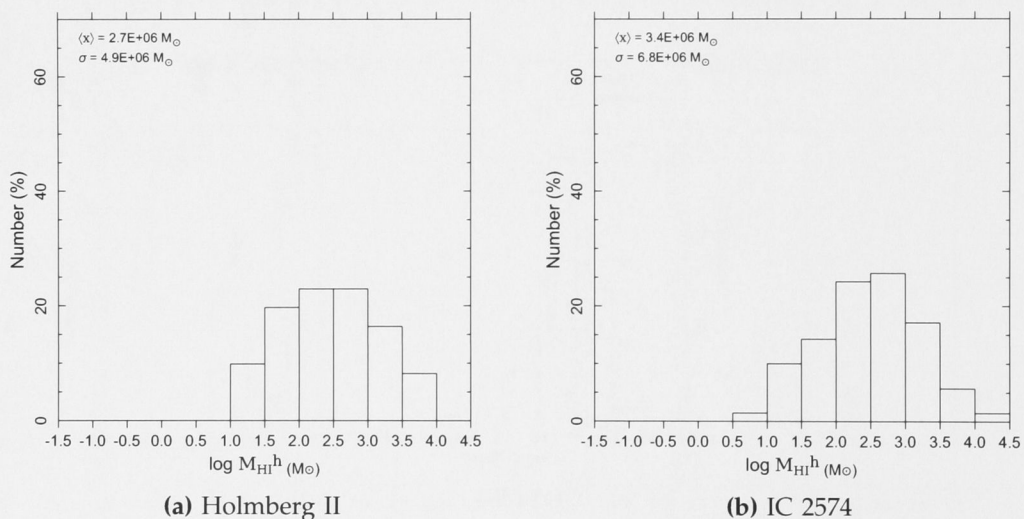
(a) Holmberg II   (b) IC 2574

Figure 3.24   Relative percentage histograms of hole evacuated H I mass ($M_{\mathrm{H I}}{}^{h}$) for all galaxies. The mean and standard deviation of $M_{\mathrm{H I}}{}^{h}$ are also shown.

What Fraction of the Total H I Mass does the Evacuated H I Mass Represent?

The H I holes are a prominent feature in the disk of all the galaxies examined in this study. An interesting question to ask is whether the total evacuated mass of all holes in a galaxy is significant when compared to the actual H I mass of the galaxy disk. Table 3.6 on Page 90 shows the total H I mass for all seven galaxies, taken from previous studies as noted, along with the fraction of the total H I disk
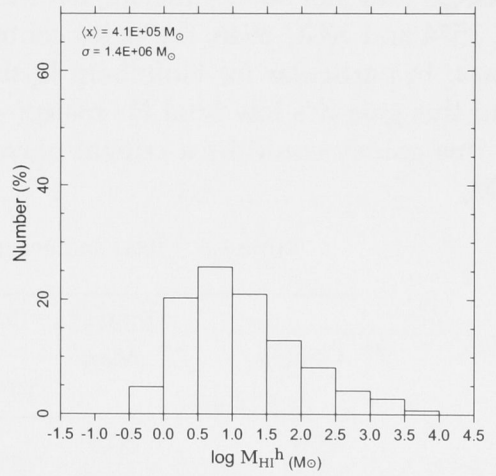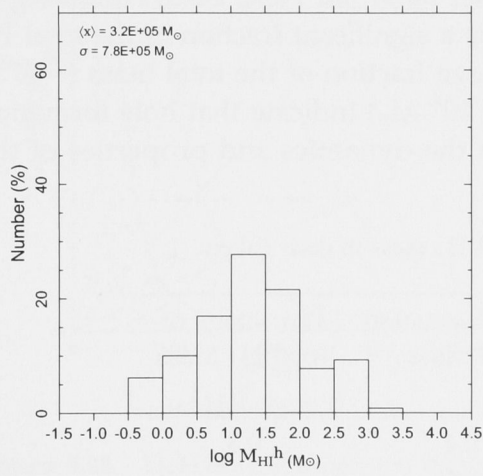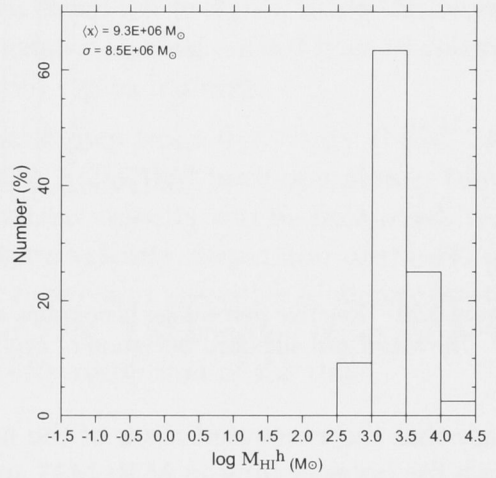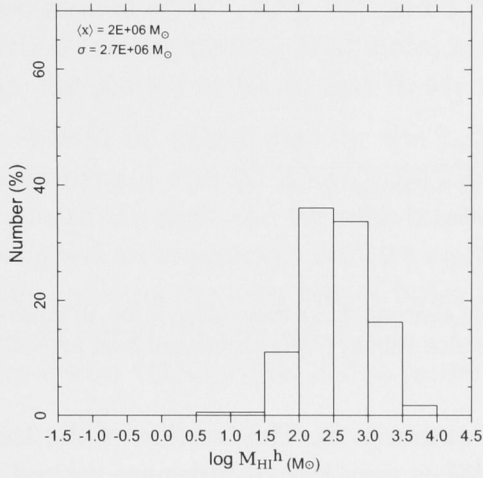
Figure 3.24 Relative percentage histograms of hole evacuated H I mass ($M_{HI}{}^{h}$) for all galaxies. The mean and standard deviation of $M_{HI}{}^{h}$ are also shown (*Figure continued from page 88*).

$\langle x \rangle = 2.2E+04\ M_{\odot}$
$\sigma = 5.6E+04\ M_{\odot}$

(g) M81
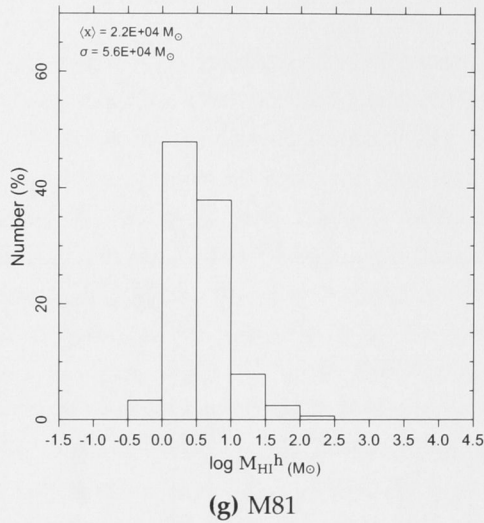
Figure 3.24   Relative percentage histograms of hole evacuated H I mass ($M_{HI}{}^{h}$) for all galaxies. The mean and standard deviation of $M_{HI}{}^{h}$ are also shown *(Figure continued from page 88)*.

mass that the evacuated mass of the holes amounts to. The fraction of the total mass the holes occupy in M31, M33 and M81 is very low. If holes are related to propagating star-formation, their contribution to feedback into the ISM from this process may not be significant. On the other hand, for NGC 2403, Holmberg II, IC 2574 and NGC 6946, the holes contribute a significant fraction of the total H I mass. In particular for Holmberg II, the large fraction of the total mass ($\sim 27\%$) and this galaxy's low total H I mass ($\sim 6 \times 10^8\ M_{\odot}$) indicate that hole formation in this galaxy could be a critical player in the dynamics and properties of the ISM.

Table 3.6   Total and evacuated H I mass in each galaxy.

Galaxy	Total H I Mass	Total Evacuated H I Mass	Percentage of Total H I Mass
		$10^8\ M_{\odot}$	%
M31	50.0[a]	0.4	0.8
M33	22.0[b]	0.6	2.0
NGC 2403	25.8[c]	3.5	13.6
Holmberg II	5.9[c]	1.7	27.8
M81	36.3[c]	0.07	0.2
IC 2574	14.7[c]	2.4	16.0
NGC 6946	41.5[c]	11.2	26.9

[a] Value taken from Carignan et al. (2006)
[b] Value taken from Corbelli (2003)
[c] Value taken from Walter et al. (2008)

x

90

3.6.5. Expansion Velocities and Energy Requirements

Measuring the expansion velocity of the H I holes is fundamental to estimating both the age of the holes and energy requirements for hole formation. Figure 3.25 on Page 91 plots the observed expansion velocity versus the measured diameter of the holes in each galaxy of the sample (excluding NGC 6946 for which individual hole expansion velocities are not available). Solid lines of constant energy are also plotted at 10^{49}, 10^{50}, 10^{51} and 10^{52} ergs (from left to right), using the average virtual column density of all holes in the galaxy. Dashed curved lines of constant age are plotted at 10, 30 and 70 Myrs (from top to bottom).

It should be noted that for the hole catalogues from this study (NGC 2403, Holmberg II and IC 2574), type 1 holes or holes that have completely blown through the disk and for which no expansion velocity can be measured, were assigned an expansion velocity equal to the velocity dispersion of the H I gas. This explains the long line of holes with expansion velocities of approximately $8 - 10$ km s^{-1} in Figures 3.25a, 3.25b and 3.25f. The banding observed in the expansion velocity axis is due to the velocity resolution of the data.
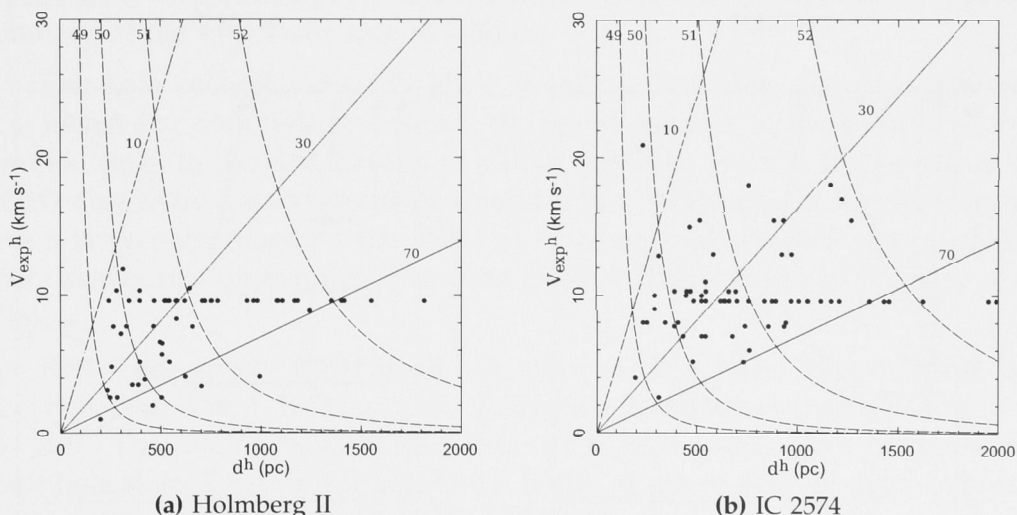
(a) Holmberg II   (b) IC 2574

Figure 3.25 Plots of hole expansion velocity (V_{exp}^h) with hole diameter (d^h). Also plotted are lines of constant age (solid) at 10, 30 and 70 Myrs and curves of constant energy (dashed) at 10^{49}, 10^{50}, 10^{51} and 10^{52} ergs as marked.

Holmberg II and IC 2574 (3.25a and 3.25b) have a much smaller spread and much lower values of hole expansion velocities than all of the spirals. It is the larger hole diameters (which contributes by a power of three to the energy as shown in Equation 3.10) found in these galaxies, however, that commits the most to larger energy requirements seen in Figure 3.25 compared to the spiral galaxies. The latter have a wide range of hole expansion velocities with smaller hole sizes and ages. The result is a smaller energy input to form the holes. The new catalogues
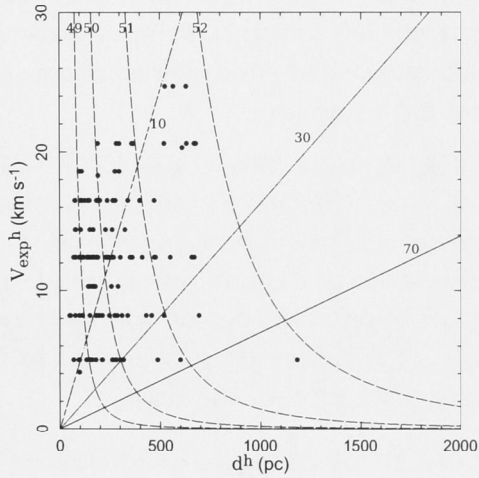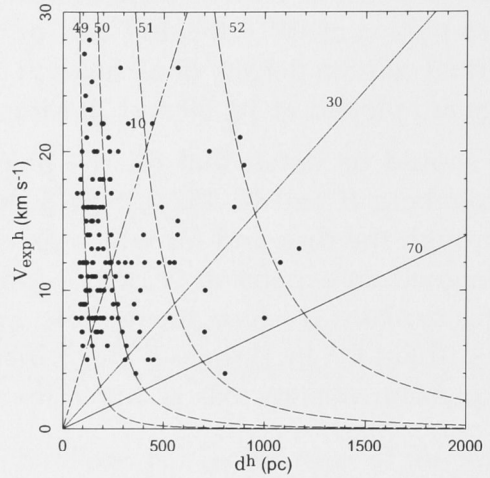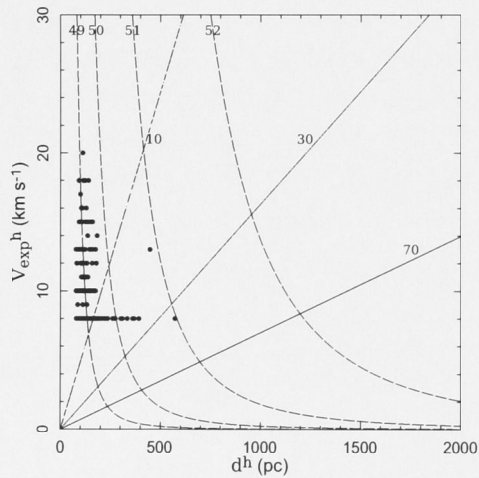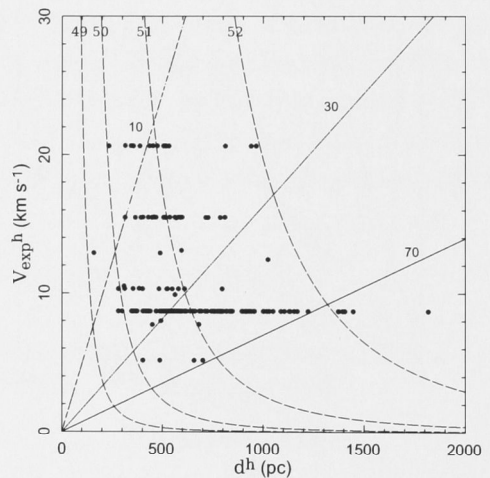
Figure 3.25 Plots of hole expansion velocity (V_{exp}^h) with hole diameter (d^h). Also plotted are lines of constant age (solid) at 10, 30 and 70 Myrs and curves of constant energy (dashed) at 10^{49}, 10^{50}, 10^{51} and 10^{52} ergs as marked (*Figure continued from page 91*).

in this sample therefore show the trends observed by Walter & Brinks (1999): the spirals are exhibiting signs of constant star-formation with time while the dwarfs could possibly have experienced a recent burst of star-formation which is now slowing down. There is however one exception, NGC 2403 (3.25f). Although NGC 2403 also shows a spread of expansion velocities, the hole ages, diameters and energies are close to those of the values found in the two dwarf galaxies. It is lacking the younger holes (< 10 Myrs) that are expected if star-formation is constant with time for spirals (Walter & Brinks, 1999). However as noted in Section 3.6.2, it is possible that the catalogue is missing the smaller holes that would fill in the left of Figure 3.25f.

3.7. Summary

This chapter has discussed the creation of catalogues of the H$\textsc{i}$ holes in the ISM of three nearby galaxies, NGC 2403, Holmberg II and IC 2574. An analysis and comparison of the observed and derived properties of the holes has been made. This analysis has made comparisons against a number of other galaxies to provide a snapshot of H$\textsc{i}$ hole populations over a range of Hubble types. A summary of the important results follows.

1. The hole coverage over the disk of each galaxy does not decrease with increasing disk radius. Instead, the spiral galaxies in the sample share a common peak in the distribution at a disk radius of around 10 kpc while the dwarfs also share a common peak around 5 kpc. Additionally, late-type spirals have a large percentage ($\sim 40 - 50\%$) of holes beyond the disk optical radius, where star-formation is unlikely in such galaxies (Bigiel et al., 2008; Leroy et al., 2008).

2. Early-type spirals have small hole diameters ($\sim 100 - 300$ pc) while late-type spirals and dwarf galaxies share hole diameters averaging 600 pc and upwards. The catalogues of holes found in late-type spirals does not probe the small hole sizes down to the resolution limits of the respective data. All other types of galaxies in the sample have holes detected as small as the sensitivity of the data allows. With the current data, there is unfortunately no way to tell whether this is an actual natural missing population of small holes, or whether the sensitivity limits of the data have been systematically under-estimated. All types of galaxies do however contain large-scale, 'hole structures' that may or may not be related be related to H$\textsc{i}$ holes. They are either real structure formed through some alternative method (which is not related to star-formation) or are a blending of smaller holes that cannot be seen individually because of the resolution, or contrast, of the data.

3. The ages of H$\textsc{i}$ holes in dwarf galaxies are the greatest across the galaxy types represented in the sample. The ages are between $40 - 46$ Myrs, but

are still much less than the calculated rotational time-scale of the disk for the dwarfs, allowing the holes to develop undisturbed and free of internal dynamical effects. Early-type spirals have hole ages around $7 - 13$ Myrs that match the life-span of OB associations. The young ages, combined with the small sizes of the holes are most likely shaped by dynamical effects in the disk. Late-type spirals have older holes (though not as venerable as the holes in dwarf galaxies), with ages around $28 - 34$ Myrs, which together with the larger diameters (than found in the early-type spirals) indicates that dynamical effects in the disk may not effect hole formation as much.

4. Comparing the sum of the evacuated H I mass of all holes in each galaxy with a galaxy's total H I mass, it was found that the evacuated mass in H I holes makes up a significant fraction of the total H I mass of late-type spirals and dwarf galaxies. The evacuated mass of H I holes in early-type spirals is significantly smaller, most likely due to the small hole sizes (because of dynamical effects which disrupt hole growth) and thin H I disks found in these galaxies.

5. In this study, it was found that the amount of energy required to form the H I holes, assuming supernova explosions as the progenitor, follows the trends with galaxy type observed by Walter & Brinks (1999). Dwarf galaxies have holes with large diameters but small expansion velocities, which could indicate a burst of recent star-formation. On the other hand, all spirals in the sample have a large spread of hole expansion velocities and hole sizes, hinting at possible on-going star-formation.

CHAPTER 4

FUTURE WORK AND FINAL REMARKS

4.1. Multi-Scale CLEAN and THINGS: The Next Steps

THE work presented in Chapter 2 indicates that using a scale-sensitive deconvolution algorithm on extended sources has potential benefits over classical deconvolution techniques. Algorithms such as MSCLEAN more accurately model the structure of extended sources, so the use of such an algorithm would be beneficial to surveys such as THINGS, which is comprised of high-resolution images of galaxies. The THINGS team is currently looking into the use of MSCLEAN for a future enhanced data-release of the THINGS catalogue and Chapter 2 is a first-step towards this endeavour.

The THINGS data-set covers a large range of Hubble types and the galaxies within the sample vary significantly in complexity and spatial size. It would be ideal then to take the two extremes, a very large and complicated source (*i.e.*, M81, NGC 5457 *etc.*) and a smaller, compact source such (*i.e.*, DDO 53, M81dwB *etc.*) and run the tests performed in Chapter 2. In addition to validating MSCLEAN's performance on the full range of real extended structure, this would allow further optimisation of the MSCLEAN parameter choices that produce acceptable results. Although this study discovered that MSCLEAN appears more robust to certain parameter changes than, for example, classical CLEAN, there is still room for refinement.

Ultimately however, more detailed quantitative comparisons do need to be performed and MSCLEAN needs to be compared against a larger range of modern scale-sensitive deconvolution algorithms. Such a comparison then needs to be duplicated with simulated data. With actual observations, the absolute flux of an object is not known, thus comparisons using real data are awkward, as the

'right' answer is not known. Using artificial observations, where the absolute flux is known and can be controlled, will alleviate this problem. Such a detailed testing process will not only be applicable to THINGS however, and will have wider implications for next-generation radio telescope facilities. THINGS reaches close to the spatial limits of the VLA and so can be thought of as the minimum data products that future facilities will produce. Therefore testing MSCLEAN on THINGS will show its applicability to the huge amounts of high-resolution, high-volume data that will be produced by facilities such as SKA, ALMA, LOFAR and EVLA.

4.1.1. Complete Hole Catalogues for all THINGS Galaxies

Work is already underway to catalogue the H$_I$ hole populations in all 34 galaxies in the THINGS sample. Bagetakos et al. (2009) has completed hole catalogues for 20 THINGS galaxies, including the three galaxies catalogued in this study. However, Bagetakos et al. used the original THINGS survey, which has been processed with classical CLEAN and will likely use this data to complete hole catalogues of the remaining 14 galaxies. Ideally, after the entire THINGS sample has been processed with MSCLEAN (as mentioned above) hole catalogues could be constructed from MSCLEAN versions of the THINGS data. Already there are significant differences, despite using almost identical hole finding methods. Bagetakos et al. (2009) finds only 39 and 27 holes in Holmberg II and IC 2574, while this study (Chapter 3) finds 61 and 70 respectively. It is then imperative that the processing performed on the data lead to the maximum contrast benefits, which MSCLEAN should provide.

4.1.2. A Multi-wavelength Hole Analysis

Once hole catalogues have been created for all galaxies within the THINGS sample, the next natural step would be to look for correlations with objects in other wavelengths, in order to investigate the link between H$_I$ hole formation and star-formation. H$_{II}$ regions, the sites of on-going star formation, are visible in Hα wavelengths. Such regions could be located on the rims of holes, where the compression of the H$_I$ gas caused by the expansion of the hole could trigger propagating star-formation (Oey et al., 2005). So holes should exhibit Hα emission on their rims. Young OB star clusters, a source of supernovae and strong stellar winds, are believed to be the most likely progenitor of holes. Such objects are traced most readily in the ultra-violet wavelengths, and so searching for ultra-violet emission in the centre of smaller holes should harden the link between hole-formation and star-formation. Older stars and complex dust and grains, the leftovers from supernovae explosions, are most easily seen in infrared wavelengths. For older holes, whose progenitors have likely burned out or

disappeared, looking in the infrared for signs of these products of supernovae explosions could further solidify the link between H I holes and stellar activity in the H I disk.

The properties of THINGS were designed to complement existing surveys on other facilities, namely the Spitzer Infrared Nearby Galaxy Survey (SINGS) (Kennicutt et al., 2003) and the GALEX Nearby Galaxy Survey (NGS) (Gil de Paz et al., 2006). So data on all of the THINGS galaxies in the wavelengths mentioned above is already available. Even more promising, the resolution and scale provided by the THINGS data-set complements those of these two surveys, allowing a direct comparison of the ISM of nearby galaxies contained in all three surveys over a wide wavelength range (Walter et al., 2008).

As an illustration of what is possible, Figures 4.1, 4.3 and 4.2 on pages 98, 99 and 99 show three-colour composite images of NGC 2403, Holmberg II and IC 2574 respectively. Red is a 24 micron image from SINGS, green is a Hα image (from SINGS ancillary data products) and blue is a far ultraviolet image from NGS. The white ellipses and circles are the H I holes and the dark grey contours are the H I contours at a column density of 1×10^{21} cm^{-2}, off an integrated intensity map from the MSCLEAN data.

A cursory glance at these images reveals the depth of possibilities. Further candidates like the super-giant shell in IC 2574 (hole 34, see Chapter 3 and Walter & Brinks, 1999; Stewart & Walter, 2000; Cannon et al., 2005) are also visible in NGC 2403 and Holmberg II. The central region of NGC 2403 shown in Figure 4.1b is a region of dense star-forming activity. Although, just beyond this central region, there is a lack of holes, within it are several H I holes (e.g., holes 147 and 148) which would make good candidates for a multi-wavelength study. In Holmberg II, there is a ridge of star-forming activity near the centre of the galaxy, and holes 22, 36, 43 and 58 all have strong emission sources in the different wavelengths within or around them that warrant further detailed analysis. Investigation of H I hole-star-formation links, in all of the galaxies from THINGS will result in a huge amount of information about the processes that drive star-formation in a wide range of galaxy Hubble types. As more of the galaxies in the THINGS sample have their H I holes catalogued, there will be a formidable amount of data to study the intricate details of star-formation within the local universe.

4.1.3. Beyond the H I Disk: Anomalous Gas

The increased contrast provided by MSCLEAN can also lead to interesting results beyond the high surface brightness disk of galaxies. 'Anomalous' neutral gas structures have been detected in a few nearby galaxies such as NGC 891 (Swaters et al., 1997) and including NGC 2403 (Fraternali et al., 2002). It has only been in recent, deep H I observations that these structures have been revealed as being

(a) Full HI disk

Figure 4.1 (a) Composite three-colour image of NGC 2403. Red is a 24 micron image from SINGS, green is a Hα image (from SINGS ancillary data products) and blue is a far ultraviolet image from NGS. The white ellipses and circles are the HI holes (Chapter 3). The dark grey contour is the HI column density at 1×10^{21} cm^{-2}, off an integrated intensity map from the MSCLEAN data (Chapter 2).
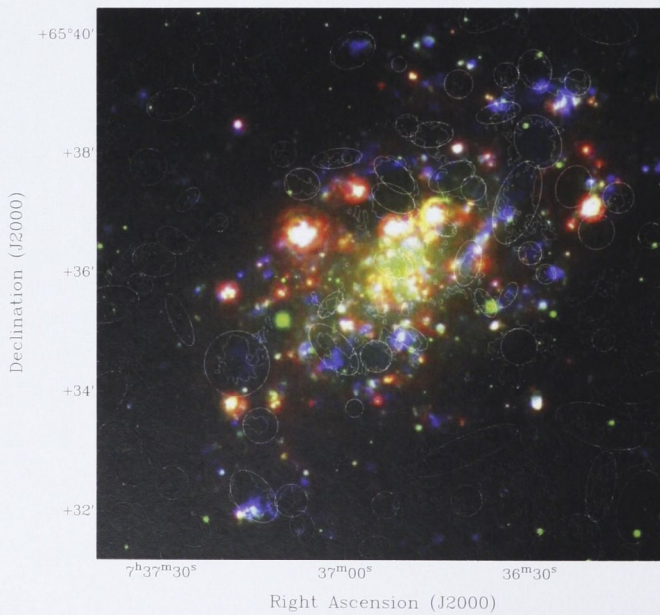
(b) Central region of HI disk

Figure 4.1 (b) Composite three-colour image of NGC 2403 showing a zoomed-in view of the central region of the disk *(Figure continued from page 98)*
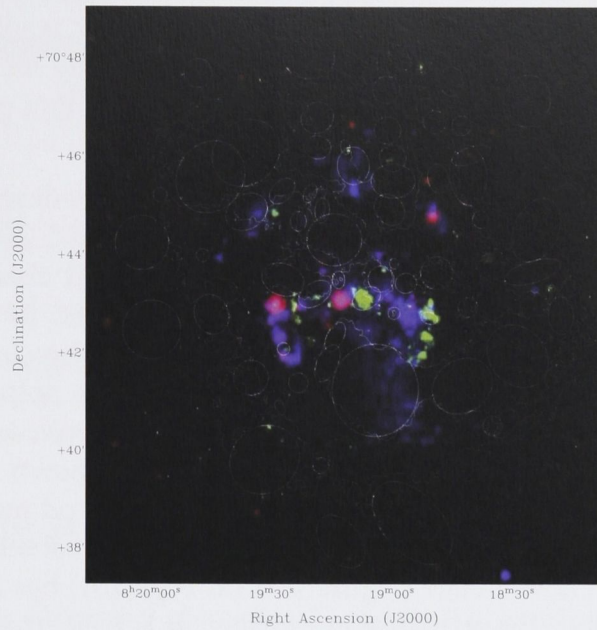
Figure 4.2 Composite three-colour image of Holmberg II. Red is a 24 micron image from SINGS, green is a Hα image (from SINGS ancillary data products) and blue is a far ultraviolet image from NGS. The white ellipses and circles are the H I holes (Chapter 3). The dark grey contour is the H I column density at 1×10^{21} cm^{-2}, off an integrated intensity map from the MSCLEAN data (Chapter 2).
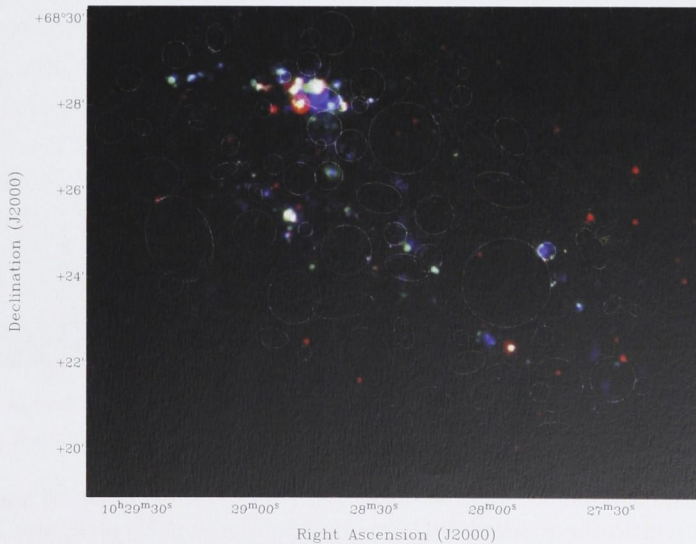
Figure 4.3 Composite three-colour image of IC 2574. Red is a 24 micron image from SINGS, green is a Hα image (from SINGS ancillary data products) and blue is a far ultraviolet image from NGS. The white ellipses and circles are the H I holes (Chapter 3). The dark grey contour is the H I column density at 1×10^{21} cm^{-2}, off an integrated intensity map from the MSCLEAN data (Chapter 2).

99

linked to a cold gaseous halo well above the main disk (Oosterloo et al., 2007). Like holes, such structures require significant angular resolution and image contrast for detection. And unlike holes, they are mostly located in the CLEAN bowl and so the performance of the deconvolution algorithm plays an important role in the interpretation of the data.

Here we make a preliminary comparison of the structures described in Fraternali et al. (2002) in the CLEAN and MSCLEAN data sets of NGC 2403. The KARMA software package was employed to make pV slices and channel map images. The structure located at ~ 108 km s^{-1} is easily observed in both data-sets as shown in Figure 4.4. The effects of the CLEAN bowl are also clearly visible in the CLEAN image (Figure 4.4b) as an apparent decrease in the noise level. This has a negative impact on the visibility of fine structure, however, as can be seen in a pV slice taken across the major axis of the ellipse as shown in Figure 4.5b on Page 101. A lot of the structure is hidden by the bowl, and much extra analysis would be needed to quantify structures over the entire cube to the same levels. In contrast, the MSCLEAN image (Figure 4.5a on Page 101) has a flat background and more features of the structure are visible. It is clear that a more detailed search will need to be conducted in NGC 2403. But as indicated, MSCLEAN greatly enhances the visibility of structures near the disk.
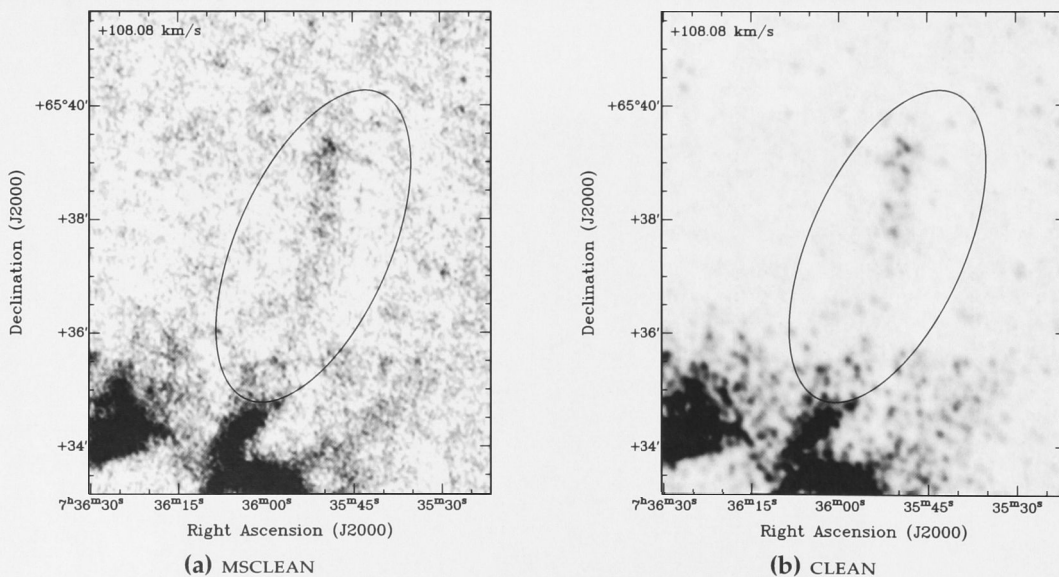
(a) MSCLEAN

(b) CLEAN

Figure 4.4 Zoomed in channel map for NGC 2403 for both MSCLEAN (a) and CLEAN (b) data cubes. Shown within the marked ellipse is the 'anomalous' H I structure as discovered by Fraternali et al. (2002). The grey-scale levels run from 0 to 15 mJy beam^{-1}.
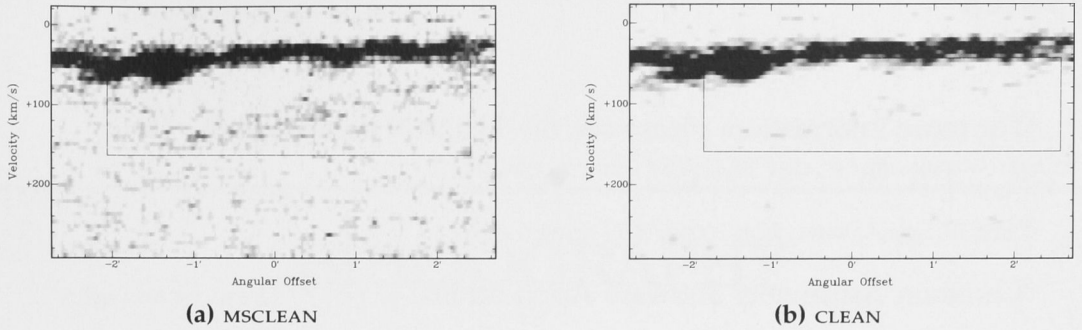
(a) MSCLEAN   **(b)** CLEAN

Figure 4.5   Position-velocity (pV) cuts through the major axis of the ellipse around the structure observed in Figure 4.4 in the MSCLEAN (a) and CLEAN (b) natural-weighted data cubes. The grey-scale levels run from 0.2 to 2 mJy beam^{-1}.

4.2. Closing Remarks

As the analysis in Chapter 2 shows, scale-sensitive algorithms such as MSCLEAN may serve as a suitable replacement for venerable deconvolution algorithms in use today. Chapter 3 demonstrates practically the advantages of using MSCLEAN, where the number of H I holes found in the galaxies Holmberg II and IC 2574 have almost doubled from the studies conducted using data processed with classical CLEAN. H I holes dominate the ISM in which they are found, and despite their small sizes, they appear to hold the key to massive star-formation through the disks of galaxies, warranting further studies to thoroughly document and analyze their properties, which may fill in gaps in the current knowledge of both star-formation and the dynamics of the ISM. The THINGS data-set produced by the VLA at its upper limits of capability, shows that continuing to use classical CLEAN, over newer algorithms like MSCLEAN, would be denying the ability to use future facilities to their full capacity and restrict the science that can be done. The next decade will therefore be interesting for the science that not only will be capable as new facilities come on-line, but what can be produced from data processed by cutting edge algorithms and software.

Notes

[1] For more information, please see the THINGS homepage at
`http://www.mpia.de/THINGS/Overview.html`

[2] See `http://www.iop.org/EJ/journal/aj`

[3] Common Astronomy Software Applications, `http://casa.nrao.edu/`

[4] Astronomical Image Processing System, `http://www.aips.nrao.edu/`

[5] `http://www.alma.info/`

[6] `http://www.aoc.nrao.edu/evla/`

[7] `http://www.lofar.org/`

[8] `http://www.skatelescope.org/`

[9] Multichannel Image Reconstruction, Image Analysis and Display
`http://www.atnf.csiro.au/computing/software/miriad/`

[10] Groningen Image Processing System, `http://www.astro.rug.nl/~gipsy/`

[11] `http://leda.univ-lyon1.fr/`

BIBLIOGRAPHY

Bagetakos, I. 2006, Master's thesis, Centre for Astrophysics Research, Department of Physics, Astronomy and Mathematics, University of Hertfordshire

Bagetakos, I., Brinks, E., Walter, F., & de Blok, W. J. G. 2009, in preparation

Bhatnagar, S. & Cornwell, T. J. 2003, in Presented at the Society of Photo-Optical Instrumentation Engineers (SPIE) Conference, Vol. 5169, Astronomical Adaptive Optics Systems and Applications. Edited by Tyson, Robert K.; Lloyd-Hart, Michael. Proceedings of the SPIE, Volume 5169, pp. 331-340 (2003)., ed. R. K. Tyson & M. Lloyd-Hart, 331–340

Bhatnagar, S. & Cornwell, T. J. 2004, A&A, 426, 747

Bigiel, F., Leroy, A., Walter, F., Brinks, E., de Blok, W. J. G., Madore, B., & Thornley, M. D. 2008, AJ, 136, 2846

Boomsma, R. 2007, PhD thesis, Kapteyn Astronomical Institute, University of Groningen

Brand, P. W. J. L. & Zealey, W. J. 1975, A&A, 38, 363

Braun, R., Thilker, D. A., Walterbos, R. M., & Corbelli, E. 2009, in preparation

Briggs, D. S. 1995a, PhD thesis, The New Mexico Institute of Mining and Technology

Briggs, D. S. 1995b, in Bulletin of the American Astronomical Society, Vol. 27, Bulletin of the American Astronomical Society, 1444

Brinks, E. & Bajaja, E. 1986, A&A, 169, 14

Brinks, E. & Shane, W. W. 1984, A&AS, 55, 179

Bureau, M. & Carignan, C. 2002, AJ, 123, 1316

Cannon, J. M., Walter, F., Bendo, G. J., Calzetti, D., Dale, D. A., Draine, B. T., Engelbracht, C. W., Gordon, K. D., Helou, G., Kennicutt, Jr., R. C., Murphy, E. J., Thornley, M. D., Armus, L., Hollenbach, D. J., Leitherer, C., Regan, M. W., Roussel, H., & Sheth, K. 2005, ApJ, 630, L37

Carignan, C., Chemin, L., Huchtmeier, W. K., & Lockman, F. J. 2006, ApJ, 641, L109

Chevalier, R. A. 1974, ApJ, 188, 501

Clark, B. G. 1980, A&A, 89, 377

Corbelli, E. 2003, MNRAS, 342, 199

Cornwell, T., Braun, R., & Briggs, D. S. 1999, in Astronomical Society of the Pacific Conference Series, Vol. 180, Synthesis Imaging in Radio Astronomy II, ed. G. B. Taylor, C. L. Carilli, & R. A. Perley, 151

Cornwell, T. J. 2008, IEEE Journal of Selected Topics in Signal Processing, vol. 2, issue 5, pp. 793-801, 2, 793

de Blok, W. J. G., Walter, F., Brinks, E., Trachternach, C., Oh, S., & Kennicutt, Jr., R. C. 2008, AJ

Deul, E. R. & den Hartog, R. H. 1990, A&A, 229, 362

Efremov, Y. N., Elmegreen, B. G., & Hodge, P. W. 1998, ApJ, 501, L163

Ehlerová, S. & Palouš, J. 2005, A&A, 437, 101

Fraternali, F., van Moorsel, G., Sancisi, R., & Oosterloo, T. 2002, AJ, 123, 3124

Gil de Paz, A., Boissier, S., Madore, B. F., Seibert, M., Joe, Y. H., Boselli, A., Wyder, T. K., Thilker, D., Bianchi, L., Rey, S. ., Rich, R. M., Barlow, T. A., Conrow, T., Forster, K., Friedman, P. G., Martin, D. C., Morrissey, P., Neff, S. G., Schiminovich, D., Small, T., Donas, J., Heckman, T. M., Lee, Y. ., Milliard, B., Szalay, A. S., & Yi, S. 2006, ApJS

Glazebrook, K. & Economou, F. 1997, The Perl Journal, 5

Gooch, R. 1996, in ASP Conf. Ser. 101: Astronomical Data Analysis Software and Systems V, ed. G. H. Jacoby & J. Barnes, 80

Heiles, C. 1979, ApJ, 229, 533

—. 1984, ApJS, 55, 585

Högbom, J. A. 1974, A&AS, 15, 417

Hu, E. M. 1981, ApJ, 248, 119

Jörsäter, S. & van Moorsel, G. A. 1995, AJ, 110, 2037

Kamphuis, J. J. 1993, PhD thesis, University of Groningen

Kennicutt, Jr., R. C., Armus, L., Bendo, G., Calzetti, D., Dale, D. A., Draine, B. T., Engelbracht, C. W., Gordon, K. D., Grauer, A. D., Helou, G., Hollenbach, D. J., Jarrett, T. H., Kewley, L. J., Leitherer, C., Li, A., Malhotra, S., Regan, M. W., Rieke, G. H., Rieke, M. J., Roussel, H., Smith, J.-D. T., Thornley, M. D., & Walter, F. 2003, PASP, 115, 928

Kim, S., Dopita, M. A., Staveley-Smith, L., & Bessell, M. S. 1999, AJ, 118, 2797

Leroy, A. K., Walter, F., Brinks, E., Bigiel, F., de Blok, W. J. G., Madore, B., & Thornley, M. D. 2008, AJ

Loeb, A. & Perna, R. 1998, ApJ, 503, L35

McClure-Griffiths, N. M., Dickey, J. M., Gaensler, B. M., & Green, A. J. 2002, ApJ, 578, 176

McCray, R. & Snow, Jr., T. P. 1979, ARA&A, 17, 213

Muller, E., Stanimirović, S., Rosolowsky, E., & Staveley-Smith, L. 2004, ApJ, 616, 845

Oey, M. S., Watson, A. M., Kern, K., & Walth, G. L. 2005, AJ, 129, 393

Oosterloo, T., Fraternali, F., & Sancisi, R. 2007, AJ, 134, 1019

Paturel, G., Petit, C., Prugniel, P., Theureau, G., Rousseau, J., Brouty, M., Dubois, P., & Cambrésy, L. 2003, A&A, 412, 45

Puche, D., Westpfahl, D., Brinks, E., & Roy, J.-R. 1992, AJ, 103, 1841

Rots, A. H. 1980, A&AS, 41, 189

Schwab, F. R. 1984, AJ, 89, 1076

Schwarz, U. J. 1978, A&A, 65, 345

Shore, S. N. 2002, The Tapestry of Modern Astrophysics (The Tapestry of Modern Astrophysics, by Steven N. Shore, pp. 888. ISBN 0-471-16816-5. Wiley-VCH , October 2002.)

Spitzer, L. J. 1956, ApJ, 124, 20

Stanimirovic, S., Staveley-Smith, L., Dickey, J. M., Sault, R. J., & Snowden, S. L. 1999, MNRAS, 302, 417

Starck, J.-L., Bijaoui, A., Lopez, B., & Perrier, C. 1994, A&A, 283, 349

Starck, J. L., Pantin, E., & Murtagh, F. 2002, PASP, 114, 1051

Stewart, S. G. & Walter, F. 2000, AJ, 120, 1794

Swaters, R. A., Sancisi, R., & van der Hulst, J. M. 1997, ApJ, 491, 140

Tan, S. M. 1986, MNRAS, 220, 971

Tenorio-Tagle, G. & Bodenheimer, P. 1988, ARA&A, 26, 145

Thompson, A. R., Moran, J. M., & Swenson, Jr., G. W. 2001, Interferometry and Synthesis in Radio Astronomy, 2nd Edition (Interferometry and synthesis in radio astronomy by A. Richard Thompson, James M. Moran, and George W. Swenson, Jr. 2nd ed. New York : Wiley, c2001.xxiii, 692 p. : ill. ; 25 cm. "A Wiley-Interscience publication." Includes bibliographical references and indexes. ISBN : 0471254924)

van der Hulst, J. M. 1996, in Astronomical Society of the Pacific Conference Series, Vol. 106, The Minnesota Lectures on Extragalactic Neutral Hydrogen, ed. E. D. Skillman, 47

van der Kruit, P. C. 1981, A&A, 99, 298

Wakker, B. P. & Schwarz, U. J. 1988, A&A, 200, 312

Walter, F. & Brinks, E. 1999, AJ, 118, 273

Walter, F., Brinks, E., de Blok, W. J. G., Bigiel, F., Kennicutt, R. C., Thornley, M. D., & Leroy, A. 2008, AJ, 136, 2563

Appendices

Tables of Hole Catalogues

Table A.1 Hole Properties for NGC 2403

Hole No.	α^h J2000.0	δ^h J2000.0	V^h_{hel} km s^{-1}	V^h_{exp} km s^{-1}	a^h $''$	b^h $''$	θ^h $\circ$	d^h pc	t^h Myrs	$N_{H\,I}{}^h$ cm^{-2}	$n_{H\,I}{}^h$ cm^{-3}	V^h pc^3	$M_{H\,I}{}^h$ $10^4 M_\odot$	R^h kpc	E^h 10^{50} ergs
(1)	(2)	(3)	(4)	(5)	(6)	(7)	(8)	(9)	(10)	(11)	(12)	(13)	(14)	(15)	(16)
1	07:38:37.2	65:26:36.4	247	8	45.0	45.0	0	1404	78	4.1e+20	0.20	1.5e+09	948.3	13.9	1186
2	07:38:15.1	65:30:35.3	252	8	54.6	39.3	161	1446	81	5.4e+20	0.26	1.6e+09	1350.2	9.6	1750
3	07:38:28.5	65:30:26.8	252	20	21.0	11.0	23	474	11	4.9e+20	0.24	5.6e+07	43.3	10.9	130
4	07:38:36.1	65:28:54.5	257	8	14.1	14.1	0	440	24	4.6e+20	0.22	4.5e+07	32.4	12.2	35
5	07:38:22.9	65:28:50.0	247	15	14.7	14.7	0	458	14	4.8e+20	0.23	5.1e+07	38.4	11.2	82
6	07:38:30.1	65:28:31.7	247	8	16.2	16.2	0	505	28	4.6e+20	0.23	6.8e+07	49.5	11.9	55
7	07:38:25.0	65:28:03.9	252	8	38.4	18.0	91	820	46	4.6e+20	0.22	2.9e+08	210.8	12.0	250
8	07:38:46.2	65:29:11.0	252	8	34.0	18.0	9	772	43	4.3e+20	0.21	2.4e+08	164.4	13.0	192
9	07:38:10.6	65:29:00.5	242	10	10.0	10.0	0	312	14	5.1e+20	0.25	1.6e+07	12.8	10.4	16
10	07:38:08.8	65:28:35.5	231	15	15.0	15.0	0	468	14	5e+20	0.24	5.4e+07	42.3	10.7	91
11	07:38:03.3	65:28:19.7	237	8	21.9	21.9	0	683	38	4.9e+20	0.24	1.7e+08	130.4	10.9	152
12	07:37:51.1	65:29:07.0	237	8	28.8	28.8	0	899	50	5.3e+20	0.26	3.8e+08	315.7	9.7	385
13	07:37:47.2	65:27:35.1	226	8	21.6	16.5	199	589	33	4.6e+20	0.23	1.1e+08	78.3	11.9	89
14	07:37:51.7	65:27:43.0	231	8	9.6	9.6	0	299	16	4.6e+20	0.23	1.4e+07	10.3	11.6	10
15	07:37:46.8	65:26:14.1	221	8	53.4	16.2	74	918	51	4.1e+20	0.20	4.1e+08	263.5	14.0	313
16	07:37:33.9	65:28:30.4	206	8	43.5	30.3	87	1133	63	5e+20	0.24	7.6e+08	598.0	10.8	745
17	07:37:12.4	65:27:39.7	190	8	63.3	19.8	28	1105	62	4.3e+20	0.21	7.1e+08	476.3	13.3	581
18	07:37:20.6	65:27:24.6	185	8	44.7	14.1	69	783	44	4.3e+20	0.21	2.5e+08	171.0	13.2	200
19	07:37:22.9	65:29:32.6	216	8	23.4	18.6	130	651	36	5.4e+20	0.26	1.4e+08	123.3	9.5	145
20	07:37:31.7	65:30:58.4	226	8	70.8	15.0	13	1017	57	8.4e+20	0.41	5.5e+08	734.6	7.1	963
21	07:37:34.7	65:32:43.4	242	8	18.6	18.6	0	580	32	8.9e+20	0.43	1e+08	143.4	5.3	176
22	07:37:36.3	65:31:54.4	242	8	13.8	13.8	0	430	24	8.9e+20	0.43	4.2e+07	58.6	6.1	69
23	07:37:28.2	65:32:28.5	237	8	16.5	16.5	0	515	28	9e+20	0.44	7.2e+07	101.6	5.1	123
24	07:37:48.3	65:32:24.1	247	8	22.5	13.5	106	544	30	8.6e+20	0.42	8.4e+07	114.1	6.5	139
25	07:37:44.7	65:33:49.2	231	20	11.1	11.1	0	346	8	8.9e+20	0.43	2.2e+07	30.5	6.0	94
26	07:37:41.6	65:33:42.3	231	8	49.2	21.0	136	1003	56	8.8e+20	0.43	5.3e+08	738.0	5.6	971
27	07:37:55.0	65:32:52.9	247	20	12.6	8.1	128	315	7	8.4e+20	0.41	1.6e+07	21.9	7.1	66
28	07:38:02.5	65:31:24.7	247	8	12.0	12.0	0	374	21	7e+20	0.34	2.8e+07	30.3	8.2	34

(1)	(2)	(3)	(4)	(5)	(6)	(7)	(8)	(9)	(10)	(11)	(12)	(13)	(14)	(15)	(16)
29	07:38:05.0	65:30:52.6	252	12	5.1	5.1	0	159	6	6.8e+20	0.33	2.1e+06	2.3	8.6	3
30	07:38:10.7	65:33:52.5	221	8	24.3	24.3	0	758	42	5.5e+20	0.27	2.3e+08	197.4	9.4	237
31	07:38:08.8	65:32:09.5	242	8	39.9	21.3	105	910	51	6.6e+20	0.32	3.9e+08	413.4	8.6	519
32	07:37:59.7	65:30:04.8	247	8	28.8	15.6	99	661	37	6.4e+20	0.31	1.5e+08	152.9	8.9	184
33	07:37:48.9	65:30:11.1	242	8	21.0	8.1	106	407	22	6.8e+20	0.33	3.5e+07	38.2	8.3	43
34	07:37:49.3	65:31:16.1	242	8	20.7	12.0	218	492	30	8.5e+20	0.41	6.2e+07	83.7	7.3	91
35	07:37:44.2	65:29:40.2	231	8	23.1	12.6	227	532	29	6.4e+20	0.31	7.9e+07	79.6	8.9	93
36	07:37:14.9	65:32:15.7	221	8	30.0	18.9	220	743	41	8.8e+20	0.43	2.2e+08	300.6	5.3	381
37	07:37:08.7	65:32:11.7	206	20	16.5	16.5	0	515	12	8.8e+20	0.43	7.2e+07	99.8	5.7	324
38	07:37:13.8	65:33:26.7	226	8	17.7	17.7	0	552	31	7.9e+20	0.38	8.8e+07	109.7	3.6	132
39	07:37:17.6	65:34:28.6	221	8	33.0	33.0	0	1030	57	6.6e+20	0.32	5.7e+08	596.2	3.0	760
40	07:37:24.5	65:31:40.6	231	20	16.2	16.2	0	505	11	8.8e+20	0.43	6.8e+07	94.5	6.1	306
41	07:37:07.0	65:31:45.7	208	20	16.2	12.0	194	435	10	8.6e+20	0.42	4.3e+07	58.7	6.5	186
42	07:36:51.4	65:30:46.8	175	8	22.2	22.2	0	693	38	5.5e+20	0.27	1.7e+08	151.0	9.4	179
43	07:36:55.2	65:31:25.8	180	15	15.9	10.5	103	403	12	7.5e+20	0.37	3.4e+07	40.7	7.9	90
44	07:36:53.4	65:32:07.8	175	8	13.5	13.5	0	421	23	8.4e+20	0.41	3.9e+07	51.9	6.8	61
45	07:36:47.0	65:27:47.8	164	8	26.7	26.7	0	833	46	4e+20	0.20	3e+08	191.9	15.1	224
46	07:37:06.5	65:29:27.7	195	8	25.5	25.5	0	796	44	5e+20	0.25	2.6e+08	210.5	10.5	251
47	07:37:09.7	65:30:52.7	200	5	15.6	15.6	0	487	46	7.6e+20	0.37	6e+07	72.5	7.9	47
48	07:36:38.0	65:29:13.8	149	8	40.5	21.9	116	929	52	4.2e+20	0.21	4.2e+08	282.3	13.4	337
49	07:36:58.5	65:33:44.8	180	8	9.0	9.0	0	280	15	7.9e+20	0.38	1.2e+07	14.4	3.6	16
50	07:37:01.8	65:34:43.8	190	8	32.1	16.2	224	711	40	6.9e+20	0.34	1.9e+08	205.4	1.8	251
51	07:36:54.9	65:34:36.8	175	8	15.9	15.9	0	496	27	6.1e+20	0.30	6.4e+07	61.5	2.3	71
52	07:36:49.3	65:34:55.8	149	8	18.6	9.6	238	417	23	6.3e+20	0.31	3.8e+07	38.0	2.2	43
53	07:36:40.4	65:33:02.8	144	8	57.0	14.4	114	894	50	8.6e+20	0.42	3.7e+08	509.6	6.4	659
54	07:36:40.3	65:32:12.8	154	8	15.6	15.6	0	487	27	7.5e+20	0.36	6e+07	71.2	7.9	84
55	07:36:25.5	65:31:08.7	133	8	58.2	33.3	144	1374	77	4.7e+20	0.23	1.4e+09	1017.6	11.4	1291
56	07:36:12.2	65:32:06.5	128	8	37.5	21.9	164	894	50	4.7e+20	0.23	3.8e+08	280.4	11.4	337
57	07:36:00.0	65:32:45.3	118	8	26.1	13.5	145	586	32	4.6e+20	0.23	1.1e+08	77.0	11.9	87

(1)	(2)	(3)	(4)	(5)	(6)	(7)	(8)	(9)	(10)	(11)	(12)	(13)	(14)	(15)	(16)
58	07:35:31.9	65:33:09.5	87	8	53.1	26.4	151	1168	65	4e+20	0.20	8.4e+08	531.0	15.1	647
59	07:36:05.2	65:30:15.4	123	8	38.4	17.1	104	800	44	4.1e+20	0.20	2.7e+08	172.2	15.3	201
60	07:35:45.7	65:31:45.9	108	8	54.9	27.9	106	1221	68	4.1e+20	0.20	9.6e+08	612.5	15.3	752
61	07:36:31.7	65:34:46.7	102	8	18.3	18.3	0	571	32	9.4e+20	0.46	9.8e+07	145.5	4.5	180
62	07:36:33.4	65:35:38.7	87	15	14.1	7.2	148	314	9	6.6e+20	0.32	1.6e+07	16.9	3.0	36
63	07:36:37.2	65:35:30.8	102	8	16.2	7.8	212	350	19	5.5e+20	0.27	2.3e+07	19.7	2.7	21
64	07:36:32.0	65:37:11.7	61	20	43.8	20.7	159	940	22	6.3e+20	0.31	4.4e+08	435.9	2.2	1463
65	07:36:28.6	65:38:12.7	61	8	27.9	22.8	208	787	44	6.9e+20	0.34	2.6e+08	278.8	3.1	346
66	07:36:18.5	65:33:27.6	113	20	46.8	20.4	253	964	22	6.9e+20	0.34	4.7e+08	513.9	8.4	1749
67	07:35:52.0	65:34:14.1	102	8	62.4	21.9	112	1154	64	5e+20	0.24	8.1e+08	631.7	10.8	789
68	07:35:53.9	65:35:42.1	77	20	21.9	12.6	135	518	12	6.8e+20	0.33	7.3e+07	78.5	8.6	247
69	07:35:41.2	65:35:46.8	66	13	21.6	16.8	90	594	22	5.1e+20	0.25	1.1e+08	88.5	10.3	163
70	07:35:44.6	65:35:20.9	82	10	12.3	12.3	0	384	18	5.1e+20	0.25	3e+07	23.9	10.3	31
71	07:36:11.1	65:34:06.5	108	8	29.1	12.6	115	597	33	6.9e+20	0.34	1.1e+08	121.5	8.3	145
72	07:36:18.0	65:34:53.6	97	20	11.4	11.4	0	355	8	8.8e+20	0.43	2.4e+07	32.7	6.2	101
73	07:36:19.1	65:36:42.6	61	9	18.0	18.0	0	561	27	8.1e+20	0.40	9.3e+07	119.4	3.9	167
74	07:36:15.5	65:37:16.6	46	8	15.6	15.6	0	487	27	8.4e+20	0.41	6e+07	79.8	4.1	95
75	07:36:10.2	65:36:38.5	56	8	12.9	12.9	0	402	22	8.9e+20	0.43	3.4e+07	47.9	5.2	56
76	07:36:04.5	65:36:35.4	71	8	11.1	11.1	0	346	19	8.8e+20	0.43	2.2e+07	30.4	6.1	35
77	07:36:04.1	65:35:57.4	66	20	14.7	10.5	241	387	9	8.4e+20	0.41	3.1e+07	40.4	6.8	126
78	07:35:55.7	65:36:41.2	56	10	17.7	13.5	142	482	22	8.5e+20	0.41	5.9e+07	78.9	7.2	114
79	07:35:19.7	65:36:13.1	61	10	25.5	25.5	0	796	37	4.3e+20	0.21	2.6e+08	180.9	12.9	258
80	07:35:26.8	65:36:31.4	66	20	25.5	11.4	151	532	12	4.7e+20	0.23	7.9e+07	58.3	11.5	176
81	07:35:12.8	65:35:03.9	71	8	43.5	27.9	238	1087	61	4e+20	0.20	6.7e+08	428.9	15.2	518
82	07:35:08.6	65:38:23.7	41	8	41.4	22.5	232	952	53	4.5e+20	0.22	4.5e+08	319.4	12.4	384
83	07:34:59.6	65:39:30.3	30	8	50.4	18.0	136	940	52	4.3e+20	0.21	4.4e+08	296.8	13.0	355
84	07:35:28.5	65:39:41.4	35	8	44.1	16.5	167	842	47	5.8e+20	0.28	3.1e+08	284.2	9.2	348
85	07:35:42.9	65:37:21.9	66	12	65.1	16.5	144	1023	40	6.8e+20	0.33	5.6e+08	604.4	8.5	1162
86	07:36:02.3	65:37:17.3	51	15	18.9	18.9	0	590	18	8.9e+20	0.43	1.1e+08	150.7	5.8	359

(1)	(2)	(3)	(4)	(5)	(6)	(7)	(8)	(9)	(10)	(11)	(12)	(13)	(14)	(15)	(16)
87	07:36:03.5	65:37:57.3	35	7	14.4	14.4	0	449	28	8.8e+20	0.43	4.8e+07	65.8	5.4	68
88	07:35:32.8	65:35:09.6	71	8	19.5	14.4	249	523	29	4.6e+20	0.22	7.5e+07	54.1	12.2	60
89	07:35:21.8	65:33:45.2	87	8	19.5	19.5	0	608	34	4.1e+20	0.20	1.2e+08	77.4	15.6	87
90	07:36:22.8	65:37:27.6	56	10	21.9	17.4	155	609	28	7.1e+20	0.34	1.2e+08	132.4	3.1	193
91	07:35:45.4	65:38:58.9	25	10	31.2	9.9	162	548	26	8.5e+20	0.41	8.7e+07	115.7	7.3	170
92	07:35:54.9	65:38:47.2	25	10	26.7	12.9	150	579	27	8.7e+20	0.43	1e+08	140.7	6.2	210
93	07:35:59.5	65:39:20.3	20	5	36.0	12.3	136	656	62	8.9e+20	0.43	1.5e+08	208.0	5.9	143
94	07:36:07.9	65:39:17.4	25	15	23.1	6.9	166	394	12	8.9e+20	0.44	3.2e+07	45.2	5.2	102
95	07:35:48.9	65:40:07.0	25	8	35.4	35.4	0	1105	62	8.4e+20	0.41	7.1e+08	938.5	7.1	1242
96	07:35:48.5	65:41:20.0	25	8	48.6	14.1	264	817	45	7.4e+20	0.36	2.9e+08	334.2	8.0	420
97	07:36:04.3	65:40:48.4	30	8	33.6	19.2	115	793	44	8.4e+20	0.41	2.6e+08	348.0	6.8	442
98	07:36:11.2	65:41:49.5	46	15	30.6	17.7	203	726	22	7.2e+20	0.35	2e+08	227.4	8.1	540
99	07:36:17.7	65:40:11.6	51	20	34.2	19.8	256	812	19	8.8e+20	0.43	2.8e+08	391.6	5.8	1344
100	07:36:29.0	65:39:25.7	61	15	20.1	16.5	199	568	18	9.6e+20	0.47	9.6e+07	145.2	4.8	346
101	07:36:22.1	65:39:12.6	51	8	12.9	12.9	0	402	22	9.2e+20	0.45	3.4e+07	49.8	4.4	59
102	07:36:33.7	65:39:19.8	61	15	12.6	12.6	0	393	12	9.7e+20	0.47	3.2e+07	48.7	4.7	111
103	07:36:35.0	65:38:41.8	71	8	22.8	9.9	104	469	26	7.9e+20	0.39	5.4e+07	67.6	3.8	80
104	07:35:40.5	65:42:24.8	30	8	33.6	33.6	0	1049	58	5.6e+20	0.27	6e+08	535.8	9.3	671
105	07:34:55.8	65:42:10.1	15	8	58.2	58.2	0	1817	102	4.4e+20	0.21	3.1e+09	2170.5	12.8	2820
106	07:35:17.8	65:41:04.0	20	20	21.9	12.0	169	506	12	5.1e+20	0.25	6.8e+07	54.6	10.4	165
107	07:35:01.7	65:43:21.4	10	8	17.1	17.1	0	533	30	4.4e+20	0.21	8e+07	55.2	12.6	61
108	07:35:16.8	65:43:18.0	15	8	39.3	26.1	129	999	56	4.7e+20	0.23	5.2e+08	390.5	11.4	476
109	07:35:08.9	65:42:47.7	15	8	17.4	17.4	0	543	30	4.6e+20	0.23	8.4e+07	61.4	11.7	69
110	07:35:28.8	65:41:12.4	25	15	31.8	16.5	150	715	22	5.5e+20	0.27	1.9e+08	167.8	9.3	386
111	07:35:52.0	65:42:49.1	35	10	16.8	16.8	0	524	24	5.4e+20	0.26	7.6e+07	64.3	9.5	89
112	07:35:54.1	65:44:09.2	41	8	46.5	23.4	198	1029	57	4.7e+20	0.23	5.7e+08	428.9	11.3	525
113	07:35:29.6	65:43:24.5	20	8	12.0	12.0	0	374	21	5e+20	0.24	2.8e+07	21.5	10.8	23
114	07:36:16.7	65:43:45.5	61	8	51.3	25.5	235	1129	63	4.7e+20	0.23	7.5e+08	564.6	11.4	699
115	07:36:17.1	65:43:18.6	56	15	33.6	18.9	108	786	24	5e+20	0.24	2.6e+08	201.5	10.6	463

Table A.1 *Continued*

(1)	(2)	(3)	(4)	(5)	(6)	(7)	(8)	(9)	(10)	(11)	(12)	(13)	(14)	(15)	(16)
116	07:36:36.3	65:40:26.8	71	8	35.1	19.5	120	816	45	8.5e+20	0.41	2.9e+08	380.8	6.7	486
117	07:36:44.4	65:41:29.8	82	8	31.5	23.4	124	847	47	5.8e+20	0.28	3.2e+08	293.8	9.2	360
118	07:36:40.8	65:42:54.8	87	8	36.6	15.9	226	753	42	4.7e+20	0.23	2.2e+08	166.9	11.4	196
119	07:36:42.6	65:37:37.8	82	8	24.9	13.5	114	572	32	6.1e+20	0.30	9.8e+07	93.9	2.3	110
120	07:36:39.1	65:37:25.8	51	15	12.6	12.6	0	393	12	7.1e+20	0.35	3.2e+07	35.8	1.9	79
121	07:36:27.3	65:35:59.7	77	10	9.9	9.9	0	309	14	7.8e+20	0.38	1.5e+07	19.0	3.5	26
122	07:36:29.9	65:36:20.7	71	15	11.7	11.7	0	365	11	5.6e+20	0.27	2.6e+07	22.4	2.7	47
123	07:36:50.7	65:40:49.8	97	15	16.5	16.5	0	515	16	6.8e+20	0.33	7.2e+07	77.0	8.5	174
124	07:36:51.2	65:39:30.8	97	20	7.5	7.5	0	234	5	8.8e+20	0.43	6.7e+06	9.3	6.2	27
125	07:36:41.5	65:39:10.8	77	15	14.4	14.4	0	449	14	9.5e+20	0.46	4.8e+07	71.4	4.9	166
126	07:36:45.9	65:38:19.8	97	10	21.6	12.9	96	521	24	7.9e+20	0.38	7.4e+07	92.1	3.7	134
127	07:36:49.9	65:38:28.8	108	8	11.4	11.4	0	355	20	8.7e+20	0.42	2.4e+07	32.4	4.2	37
128	07:36:52.0	65:37:38.8	102	8	24.9	12.6	229	553	31	6.3e+20	0.31	8.9e+07	87.9	2.9	103
129	07:36:52.2	65:37:15.8	108	8	23.4	12.6	244	536	30	6.1e+20	0.30	8.1e+07	77.2	2.3	90
130	07:36:52.0	65:41:57.8	102	8	24.6	11.4	106	522	29	5e+20	0.24	7.5e+07	59.3	10.7	67
131	07:36:51.2	65:43:14.8	102	10	20.4	8.1	249	401	19	4.3e+20	0.21	3.4e+07	23.1	12.9	30
132	07:36:58.8	65:39:44.8	113	8	24.0	17.4	119	638	35	8.4e+20	0.41	1.4e+08	181.0	7.4	224
133	07:37:04.2	65:41:35.8	113	8	39.6	21.6	203	913	51	4.8e+20	0.23	4e+08	302.0	11.2	365
134	07:36:31.9	65:43:32.7	77	8	15.0	15.0	0	468	26	4.6e+20	0.23	5.4e+07	39.3	11.9	43
135	07:37:13.8	65:40:00.7	128	8	27.9	15.6	143	651	36	5.4e+20	0.26	1.4e+08	123.6	9.5	145
136	07:37:07.0	65:37:29.7	149	8	18.0	15.9	265	528	29	9.1e+20	0.44	7.7e+07	110.7	4.4	135
137	07:37:01.4	65:37:55.8	128	12	25.5	9.6	98	488	18	9.2e+20	0.45	6.1e+07	88.7	4.4	168
138	07:37:10.1	65:37:59.7	139	5	12.9	12.9	0	402	38	8.8e+20	0.43	3.4e+07	47.5	5.6	30
139	07:37:22.6	65:39:30.6	133	8	21.0	14.1	173	537	30	5.3e+20	0.26	8.1e+07	67.4	9.7	77
140	07:37:28.5	65:38:49.5	144	8	24.9	15.6	105	615	34	5.6e+20	0.27	1.2e+08	107.6	9.3	126
141	07:37:29.3	65:41:01.5	128	8	29.1	24.6	113	835	46	4.3e+20	0.21	3.1e+08	207.7	13.0	245
142	07:37:32.2	65:37:46.4	154	15	18.6	18.6	0	580	18	7e+20	0.34	1e+08	113.8	8.2	263
143	07:37:45.8	65:37:38.2	175	7	27.3	17.4	216	680	42	5.2e+20	0.25	1.6e+08	134.8	9.8	139
144	07:37:25.8	65:37:13.5	175	20	15.0	8.1	135	344	8	8.6e+20	0.42	2.1e+07	29.0	6.5	89

(1)	(2)	(3)	(4)	(5)	(6)	(7)	(8)	(9)	(10)	(11)	(12)	(13)	(14)	(15)	(16)
145	07:37:20.6	65:36:50.6	169	10	9.0	9.0	0	280	13	8.9e+20	0.43	1.2e+07	16.3	5.2	22
146	07:37:02.3	65:35:28.8	200	10	16.5	7.8	137	354	16	7.3e+20	0.35	2.3e+07	26.6	1.3	36
147	07:36:52.2	65:36:09.8	118	15	20.1	13.5	250	514	16	4.9e+20	0.24	7.1e+07	55.4	0.3	120
148	07:36:44.2	65:36:47.8	66	8	15.9	8.7	243	367	20	7.7e+20	0.37	2.6e+07	31.4	1.1	36
149	07:36:40.1	65:36:10.8	87	8	23.4	12.9	166	542	30	6.8e+20	0.33	8.4e+07	90.1	1.4	106
150	07:37:38.9	65:35:27.3	200	8	33.0	18.0	103	760	42	8.8e+20	0.43	2.3e+08	319.0	6.2	405
151	07:37:28.2	65:36:32.5	185	20	18.0	11.7	235	453	10	8.9e+20	0.43	4.9e+07	68.5	5.9	219
152	07:37:31.2	65:36:12.5	195	15	22.2	16.5	259	597	18	8.9e+20	0.43	1.1e+08	156.7	5.9	374
153	07:37:33.5	65:35:48.4	195	8	13.2	9.9	247	356	20	8.9e+20	0.44	2.4e+07	33.6	5.8	39
154	07:37:55.1	65:37:04.9	180	8	18.0	18.0	0	561	31	5.1e+20	0.25	9.3e+07	74.7	10.4	85
155	07:37:27.0	65:35:12.5	216	15	28.2	9.3	205	505	15	9e+20	0.44	6.8e+07	95.9	4.3	224
156	07:37:45.4	65:34:19.2	226	8	26.4	10.5	246	519	29	8.7e+20	0.43	7.4e+07	101.3	6.3	123
157	07:37:57.3	65:34:57.9	211	8	21.3	16.8	107	590	33	6.9e+20	0.33	1.1e+08	116.8	8.4	140
158	07:37:50.5	65:33:54.0	226	15	20.4	9.3	174	430	13	8.4e+20	0.41	4.2e+07	55.2	6.8	125
159	07:38:21.7	65:31:58.1	237	15	34.5	19.5	165	809	25	5.1e+20	0.25	2.8e+08	224.3	10.1	519
160	07:38:31.9	65:33:02.7	226	8	36.6	17.1	149	781	43	4.6e+20	0.23	2.5e+08	182.5	11.8	215
161	07:38:04.2	65:34:59.7	216	8	12.0	12.0	0	374	21	5.5e+20	0.27	2.8e+07	23.7	9.4	26
162	07:38:01.9	65:35:47.7	206	15	18.0	18.0	0	561	17	5.2e+20	0.25	9.3e+07	76.0	9.8	168
163	07:37:44.1	65:39:19.2	149	8	19.8	19.8	0	618	34	4.6e+20	0.22	1.2e+08	89.9	12.1	103
164	07:38:05.8	65:39:52.6	154	8	73.8	27.0	107	1393	78	4e+20	0.20	1.4e+09	905.2	15.9	1128
165	07:38:02.9	65:37:54.7	164	8	35.7	15.0	255	722	40	4.4e+20	0.21	2e+08	137.2	12.6	159
166	07:38:31.4	65:35:31.7	195	8	43.5	14.7	268	789	44	4.2e+20	0.20	2.6e+08	169.8	13.7	198
167	07:39:01.9	65:25:54.2	257	8	55.5	34.8	199	1372	77	4e+20	0.20	1.4e+09	862.2	15.9	1072
168	07:38:22.5	65:26:32.0	242	8	42.9	21.9	25	957	53	4.2e+20	0.21	4.6e+08	307.2	13.5	368
169	07:38:05.0	65:26:26.6	237	8	39.3	16.5	98	795	44	4.3e+20	0.21	2.6e+08	177.0	13.4	207
170	07:36:40.7	65:30:24.8	159	15	21.9	13.5	114	536	16	4.9e+20	0.24	8.1e+07	62.2	11.1	136
171	07:36:18.5	65:32:27.6	128	5	35.7	14.1	169	700	66	5.1e+20	0.25	1.8e+08	146.0	10.0	95
172	07:36:07.0	65:35:15.4	82	8	21.0	15.0	116	554	31	8.5e+20	0.41	8.9e+07	119.3	7.3	145

Table A.2   Hole Properties for Holmberg II

Hole No.	α^h	δ^h	V^h_{hel}	V^h_{exp}	a^h	b^h	θ^h	d^h	t^h	$N_{\mathrm{H\,I}}^h$	$n_{\mathrm{H\,I}}^h$	V^h	$M_{\mathrm{H\,I}}^h$	R^h	E^h
	J2000.0	J2000.0	km s^{-1}	km s^{-1}	''	''	°	pc	Myrs	cm^{-2}	cm^{-3}	pc^3	$10^4 M_\odot$	kpc	10^{50} ergs
(1)	(2)	(3)	(4)	(5)	(6)	(7)	(8)	(9)	(10)	(11)	(12)	(13)	(14)	(15)	(16)
1	08:18:17.8	70:42:47.9	159	4	23.1	15.5	5	621	74	7.7e+20	0.24	1.3e+08	97.7	5.1	47
2	08:18:24.0	70:44:32.5	148	9	41.1	27.6	155	1107	56	7.6e+20	0.24	7.1e+08	544.9	4.6	755
3	08:18:24.9	70:43:41.5	151	9	36.4	13.2	106	719	36	7.6e+20	0.24	2e+08	150.0	4.3	197
4	08:18:26.4	70:47:10.4	138	4	31.9	28.6	158	992	118	7.3e+20	0.23	5.1e+08	377.9	5.6	195
5	08:18:28.6	70:41:58.2	164	8	41.8	34.2	43	1242	68	7.9e+20	0.25	1e+09	798.5	4.1	1034
7	08:18:37.9	70:44:45.7	143	9	11.0	9.8	6	341	17	8.4e+20	0.26	2.1e+07	17.6	3.3	21
9	08:18:41.0	70:45:39.5	140	9	37.3	23.0	5	962	49	8.5e+20	0.26	4.7e+08	397.8	3.5	549
10	08:18:42.4	70:41:21.4	159	9	38.8	32.5	122	1168	59	8.6e+20	0.27	8.3e+08	725.5	3.1	1028
11	08:18:45.3	70:47:34.3	130	9	17.5	14.2	0	518	26	7.5e+20	0.23	7.3e+07	54.8	4.7	69
13	08:18:54.9	70:38:32.6	177	9	61.1	36.4	43	1551	78	7.7e+20	0.24	2e+09	1506.8	4.8	2177
14	08:18:56.6	70:43:27.6	138	3	13.3	12.2	99	419	52	1.3e+21	0.39	3.9e+07	48.8	0.9	22
15	08:18:58.3	70:48:03.5	128	2	18.0	10.8	38	458	112	7.5e+20	0.23	5e+07	38.2	4.8	7
16	08:18:59.6	70:43:51.4	153	1	6.6	5.5	9	198	96	1.3e+21	0.40	4.1e+06	5.2	0.8	0
17	08:18:59.9	70:45:32.4	140	9	27.3	20.8	90	784	39	9.1e+20	0.28	2.5e+08	230.6	2.3	313
18	08:18:59.9	70:46:00.4	135	9	16.4	16.4	176	539	27	8.9e+20	0.28	8.2e+07	73.5	2.8	95
19	08:19:00.8	70:44:57.3	135	9	20.9	17.0	43	619	31	1.1e+21	0.33	1.2e+08	131.8	1.8	177
21	08:19:04.2	70:41:16.1	171	9	56.9	53.6	0	1814	92	9.9e+20	0.31	3.1e+09	3128.8	1.9	4753
22	08:19:06.5	70:43:09.0	164	6	18.6	12.8	118	506	38	1.9e+21	0.58	6.8e+07	128.1	0.2	115
25	08:19:09.9	70:45:50.8	125	3	23.0	19.8	3	701	100	8.8e+20	0.28	1.8e+08	161.3	2.7	66
26	08:19:11.9	70:46:13.6	138	3	9.0	5.6	14	233	36	8.5e+20	0.26	6.6e+06	5.7	3.1	1
27	08:19:12.7	70:38:09.6	184	9	37.3	24.0	40	982	50	7.6e+20	0.24	5e+08	381.9	5.0	522
28	08:19:13.5	70:43:31.5	148	7	10.9	7.7	0	300	20	1.3e+21	0.39	1.4e+07	18.1	1.0	16
29	08:19:14.3	70:42:21.5	179	9	19.6	10.3	153	466	23	1.2e+21	0.37	5.3e+07	63.2	1.3	83
30	08:19:14.6	70:44:20.5	143	9	33.9	31.8	90	1079	54	1.1e+21	0.34	6.6e+08	729.3	1.5	1053
32	08:19:16.2	70:41:49.4	179	9	24.5	12.8	153	580	29	1e+21	0.32	1e+08	107.9	1.8	143
33	08:19:17.7	70:44:56.3	133	3	15.3	9.0	176	386	54	9.1e+20	0.28	3e+07	27.8	2.2	11
34	08:19:18.8	70:46:13.2	153	5	16.6	14.2	82	504	43	8.4e+20	0.26	6.7e+07	57.2	3.4	40
35	08:19:18.9	70:46:49.2	148	10	20.6	18.6	122	643	29	8.2e+20	0.26	1.4e+08	115.7	3.9	168

(1)	(2)	(3)	(4)	(5)	(6)	(7)	(8)	(9)	(10)	(11)	(12)	(13)	(14)	(15)	(16)
36	08:19:19.4	70:43:14.2	143	8	22.1	13.9	123	577	33	1.1e+21	0.35	1e+08	112.5	1.6	127
37	08:19:20.7	70:45:17.1	133	11	12.2	7.3	153	311	12	9e+20	0.28	1.6e+07	14.3	2.7	22
38	08:19:21.1	70:48:02.1	135	9	31.8	25.2	86	930	47	7.7e+20	0.24	4.2e+08	325.2	5.1	442
39	08:19:23.6	70:44:42.9	135	3	12.0	9.8	0	357	49	8.9e+20	0.28	2.4e+07	21.3	2.5	8
43	08:19:27.2	70:42:06.7	164	4	7.7	7.7	45	254	25	8.9e+20	0.28	8.6e+06	7.7	2.6	4
44	08:19:27.4	70:43:31.7	161	9	26.6	19.6	71	750	38	9e+20	0.28	2.2e+08	199.8	2.4	269
45	08:19:27.6	70:45:19.7	153	6	18.6	12.2	135	494	36	8.4e+20	0.26	6.3e+07	53.8	3.3	44
46	08:19:28.0	70:40:54.6	164	9	9.8	5.5	27	240	12	8.4e+20	0.26	7.3e+06	6.2	3.3	7
47	08:19:31.8	70:39:50.4	174	9	45.0	40.5	131	1402	71	7.8e+20	0.24	1.4e+09	1130.9	4.3	1617
48	08:19:36.5	70:44:54.1	143	9	27.0	21.0	122	783	39	8.3e+20	0.26	2.5e+08	210.5	3.8	282
49	08:19:36.7	70:46:06.1	148	9	44.2	38.3	132	1351	68	7.7e+20	0.24	1.3e+09	1000.5	4.5	1423
50	08:19:45.1	70:42:48.6	151	9	25.0	21.0	23	753	38	7.6e+20	0.24	2.2e+08	172.4	4.3	228
51	08:19:45.5	70:45:36.6	148	9	46.0	40.4	142	1415	72	7.6e+20	0.24	1.5e+09	1132.9	5.0	1617
52	08:19:02.9	70:43:32.7	159	9	16.0	16.0	0	525	26	1.6e+21	0.48	7.6e+07	119.5	0.4	165
53	08:19:23.5	70:41:25.2	177	10	12.0	12.0	0	394	18	8.9e+20	0.28	3.2e+07	28.9	2.6	39
54	08:18:40.4	70:46:04.0	138	9	25.0	10.0	-70	519	26	8.4e+20	0.26	7.4e+07	62.1	3.8	79
55	08:18:42.8	70:46:40.0	135	9	12.0	12.0	0	394	20	7.9e+20	0.25	3.2e+07	25.5	4.1	31
56	08:18:48.9	70:43:40.1	158	7	20.0	20.0	0	657	41	1e+21	0.33	1.5e+08	157.3	1.8	166
57	08:18:59.5	70:42:50.7	161	2	7.5	7.5	0	246	46	1.3e+21	0.40	7.8e+06	10.1	0.7	2
58	08:18:50.8	70:42:44.6	171	2	10.5	7.0	74	281	53	1.1e+21	0.34	1.2e+07	13.1	1.6	3
59	08:18:41.1	70:42:58.0	164	5	12.0	12.0	0	394	37	8.9e+20	0.28	3.2e+07	28.9	2.6	17
60	08:18:34.8	70:40:32.4	164	10	12.0	12.0	0	394	18	7.7e+20	0.24	3.2e+07	25.0	4.2	33
61	08:19:35.2	70:41:31.2	169	9	21.5	21.5	0	706	35	8.5e+20	0.26	1.8e+08	157.5	3.6	209
62	08:20:02.6	70:44:15.9	158	9	33.0	33.0	0	1084	55	6e+20	0.19	6.7e+08	406.2	6.3	546
63	08:20:00.1	70:42:29.4	148	9	36.0	36.0	0	1183	60	6.8e+20	0.21	8.7e+08	593.5	6.0	818
64	08:19:47.4	70:44:01.1	151	7	8.0	8.0	0	262	16	7.4e+20	0.23	9.5e+06	7.1	4.7	6
65	08:19:58.1	70:45:14.5	140	10	8.5	8.5	0	279	13	6.6e+20	0.20	1.1e+07	7.6	6.1	9
66	08:19:48.7	70:47:43.1	146	9	17.5	17.5	0	575	29	5.5e+20	0.17	1e+08	55.0	6.6	67
67	08:19:01.6	70:47:23.7	128	5	16.5	16.5	0	542	51	7.9e+20	0.25	8.4e+07	66.3	4.1	41

(1)	(2)	(3)	(4)	(5)	(6)	(7)	(8)	(9)	(10)	(11)	(12)	(13)	(14)	(15)	(16)
68	08:19:17.7	70:39:43.2	177	7	10.0	10.0	0	328	20	8.6e+20	0.27	1.9e+07	16.1	3.7	15
69	08:18:48.6	70:45:35.6	135	2	18.0	13.0	13	502	95	8.8e+20	0.27	6.7e+07	58.8	2.9	16
70	08:19:01.3	70:46:34.2	128	9	16.5	16.5	0	542	27	8.4e+20	0.26	8.4e+07	70.9	3.3	91
71	08:18:49.5	70:46:44.6	135	7	14.1	14.1	0	463	29	8.4e+20	0.26	5.2e+07	44.0	3.8	43

Table A.3 Hole Properties for IC 2574

| Hole No. | α^h | δ^h | V^h_{hel} | V^h_{exp} | a^h | b^h | θ^h | d^h | t^h | $N_{\rm H\,I}{}^h$ | $n_{\rm H\,I}{}^h$ | V^h | $M_{\rm H\,I}{}^h$ | R^h | E^h |
| | J2000.0 | J2000.0 | km s^{-1} | km s^{-1} | $''$ | $''$ | $\circ$ | pc | Myrs | cm^{-2} | cm^{-3} | pc^3 | $10^4 M_\odot$ | kpc | 10^{50} ergs |
(1)	(2)	(3)	(4)	(5)	(6)	(7)	(8)	(9)	(10)	(11)	(12)	(13)	(14)	(15)	(16)
2	10:27:22.1	68:21:30.2	-3	5	12.4	12.4	0	481	45	7e+20	0.18	5.9e+07	33.7	8.2	20
3	10:27:29.5	68:21:40.0	5	17	31.5	31.5	0	1226	35	6.5e+20	0.17	9.7e+08	517.8	7.4	1336
4	10:27:34.9	68:24:42.2	17	15	31.5	16.4	30	886	28	6.3e+20	0.16	3.7e+08	189.5	6.9	420
7	10:27:43.9	68:21:31.5	2	9	37.5	37.5	0	1459	74	6.8e+20	0.17	1.6e+09	910.7	6.3	1257
8	10:27:46.1	68:24:38.5	33	15	12.0	12.0	0	467	15	7.1e+20	0.18	5.3e+07	31.3	5.4	63
9	10:27:46.9	68:22:40.4	17	7	13.5	13.5	0	525	36	7e+20	0.18	7.6e+07	43.9	5.2	37
10	10:27:47.8	68:21:21.4	7	9	13.5	13.5	0	525	26	6.9e+20	0.18	7.6e+07	43.2	6.2	52
11	10:27:55.1	68:27:18.3	43	8	29.0	20.2	-141	944	57	6.4e+20	0.16	4.4e+08	231.4	7.2	244
12	10:27:58.2	68:21:51.4	15	9	19.5	10.1	101	546	27	7e+20	0.18	8.5e+07	49.2	5.1	60
13	10:27:56.4	68:23:54.2	25	9	61.9	61.9	0	2414	122	6.9e+20	0.18	7.4e+09	4187.7	3.8	6152
15	10:28:06.3	68:22:03.1	25	6	25.3	15.1	-75	762	62	6.7e+20	0.17	2.3e+08	128.4	4.6	95
16	10:28:07.7	68:22:37.8	25	8	10.5	10.5	0	408	24	7e+20	0.18	3.6e+07	20.6	3.8	19
17	10:28:08.0	68:28:13.8	53	13	15.0	15.0	0	584	21	6.3e+20	0.16	1e+08	54.5	7.3	94
18	10:28:09.2	68:23:23.8	28	11	14.0	14.0	0	545	24	7.1e+20	0.18	8.5e+07	49.8	2.8	71
19	10:28:14.0	68:27:43.0	36	8	7.8	5.4	24	253	15	7.3e+20	0.19	8.5e+06	5.1	5.9	4
20	10:28:14.7	68:25:28.5	33	9	27.0	27.0	0	1051	53	6.8e+20	0.17	6.1e+08	340.3	2.3	451
21	10:28:16.2	68:24:28.6	38	18	19.5	19.5	0	758	20	7.4e+20	0.19	2.3e+08	139.8	1.4	369
22	10:28:21.6	68:24:15.4	38	13	31.5	17.9	78	925	34	8.1e+20	0.21	4.1e+08	276.5	1.2	521
23	10:28:22.3	68:27:15.4	46	9	50.0	50.0	0	1947	99	6.9e+20	0.17	3.9e+09	2185.2	4.4	3126
24	10:28:24.6	68:25:02.2	43	9	15.9	15.9	0	620	31	9.4e+20	0.24	1.2e+08	96.6	0.5	125
25	10:28:24.9	68:20:37.3	25	13	25.0	25.0	0	973	36	6.6e+20	0.17	4.8e+08	260.5	7.5	481
26	10:28:31.7	68:22:03.3	35	9	48.7	35.7	16	1625	82	7.1e+20	0.18	2.3e+09	1312.2	5.4	1844
27	10:28:28.7	68:25:51.9	48	9	32.1	20.8	257	1008	51	7.2e+20	0.18	5.4e+08	318.3	1.5	423
29	10:28:33.7	68:28:02.1	56	10	11.5	11.5	0	447	21	7e+20	0.18	4.7e+07	26.9	5.0	33
30	10:28:37.0	68:24:39.0	53	9	35.0	35.0	0	1363	69	7.1e+20	0.18	1.3e+09	777.2	1.6	1070
31	10:28:38.1	68:27:59.0	66	20	6.0	6.0	0	233	5	6.8e+20	0.17	6.7e+06	3.8	4.8	10
32	10:28:41.5	68:26:22.8	61	9	19.5	19.5	0	758	38	6.8e+20	0.17	2.3e+08	127.9	2.3	163
33	10:28:42.6	68:27:28.8	66	15	24.0	24.0	0	934	29	6.8e+20	0.17	4.3e+08	240.8	3.9	543

(1)	(2)	(3)	(4)	(5)	(6)	(7)	(8)	(9)	(10)	(11)	(12)	(13)	(14)	(15)	(16)
34	10:28:43.5	68:27:05.8	48	9	7.5	7.5	0	291	15	7.2e+20	0.18	1.3e+07	7.6	3.3	8
35	10:28:44.1	68:28:12.8	64	9	33.0	16.0	74	894	45	7e+20	0.18	3.8e+08	215.7	5.1	281
36	10:28:46.1	68:29:34.7	82	10	13.5	13.5	0	525	25	6.3e+20	0.16	7.6e+07	39.4	7.3	50
37	10:28:46.6	68:28:58.7	77	9	16.5	16.5	0	641	32	6.8e+20	0.17	1.4e+08	77.7	6.3	97
38	10:28:47.4	68:25:07.7	68	10	10.0	10.0	0	389	18	7e+20	0.18	3.1e+07	17.7	2.6	22
39	10:28:48.9	68:26:18.7	64	9	22.5	22.5	0	875	44	7.1e+20	0.18	3.5e+08	204.1	2.8	266
40	10:28:52.5	68:28:40.5	77	10	7.5	7.5	0	291	14	7.3e+20	0.19	1.3e+07	7.8	5.8	9
41	10:28:50.1	68:23:33.2	58	9	36.8	36.8	0	1435	73	6.8e+20	0.17	1.5e+09	868.7	4.7	1197
43	10:28:55.6	68:22:36.4	56	7	22.5	13.5	80	678	47	6.4e+20	0.16	1.6e+08	85.4	6.7	74
44	10:28:57.1	68:22:32.4	56	8	6.0	6.0	0	233	14	6.2e+20	0.16	6.7e+06	3.4	7.0	3
45	10:29:00.1	68:25:58.7	87	7	13.6	9.1	24	432	30	6.9e+20	0.18	4.3e+07	24.1	3.9	20
46	10:29:02.6	68:26:36.2	87	4	5.0	5.0	0	194	23	6.5e+20	0.17	3.9e+06	2.1	4.3	0
48	10:29:14.7	68:27:32.9	92	8	13.0	6.0	80	343	21	7.3e+20	0.18	2.1e+07	12.7	5.9	12
49	10:28:02.5	68:21:16.8	17	10	19.5	16.3	-202	694	32	7.2e+20	0.18	1.8e+08	104.4	5.8	144
50	10:28:35.9	68:27:05.3	56	7	22.0	22.0	0	857	54	7.1e+20	0.18	3.3e+08	194.0	3.3	197
51	10:28:40.8	68:29:41.4	79	9	30.0	30.0	0	1169	59	6.7e+20	0.17	8.4e+08	458.7	7.6	615
52	10:29:10.3	68:29:34.9	97	9	19.5	13.7	180	635	32	6.6e+20	0.17	1.3e+08	73.0	7.5	90
53	10:29:20.4	68:29:10.2	115	7	19.0	19.0	0	740	46	6.7e+20	0.17	2.1e+08	116.7	7.6	115
54	10:29:28.9	68:27:29.2	102	9	14.9	10.4	66	486	24	6.5e+20	0.16	6e+07	32.0	7.4	38
55	10:29:08.0	68:26:29.0	92	7	19.9	9.8	-67	544	38	6.9e+20	0.18	8.4e+07	47.9	4.9	41
56	10:29:00.3	68:25:04.6	82	18	30.0	30.0	0	1169	31	6.7e+20	0.17	8.4e+08	463.8	4.3	1278
57	10:28:07.3	68:28:46.0	58	2	8.0	8.0	0	311	59	7e+20	0.18	1.6e+07	9.2	8.2	2
58	10:27:57.3	68:26:03.5	40	9	42.5	22.6	73	1209	61	7.1e+20	0.18	9.3e+08	538.8	5.2	730
59	10:27:23.8	68:23:15.7	12	12	8.0	8.0	0	311	11	6.9e+20	0.18	1.6e+07	9.0	7.8	14
60	10:27:29.7	68:23:23.8	7	10	14.4	10.0	138	469	22	6.2e+20	0.16	5.4e+07	27.8	7.0	35
61	10:28:00.6	68:20:18.3	12	5	23.0	15.4	45	733	69	6.4e+20	0.16	2.1e+08	108.8	7.3	67
62	10:28:47.5	68:22:15.5	48	7	10.9	9.1	-27	389	24	6.6e+20	0.17	3.1e+07	16.9	6.4	15
63	10:28:22.3	68:22:44.0	30	10	22.6	12.7	17	659	31	7.1e+20	0.18	1.5e+08	87.3	3.7	119
64	10:28:58.1	68:27:55.7	94	10	12.0	12.0	0	467	22	6.9e+20	0.18	5.4e+07	30.6	4.9	40

(1)	(2)	(3)	(4)	(5)	(6)	(7)	(8)	(9)	(10)	(11)	(12)	(13)	(14)	(15)	(16)
65	10:29:06.5	68:27:04.7	86	15	14.4	12.3	170	517	16	6.9e+20	0.18	7.3e+07	41.2	4.9	86
66	10:29:17.3	68:28:10.3	97	10	13.6	9.8	133	449	21	6.6e+20	0.17	4.8e+07	25.7	6.5	33
67	10:28:55.4	68:26:38.1	84	10	14.0	14.0	0	545	25	7.1e+20	0.18	8.5e+07	49.9	3.6	66
68	10:28:37.7	68:23:21.7	53	9	43.0	17.0	280	1053	53	7e+20	0.18	6.1e+08	352.5	3.6	469
69	10:27:43.5	68:20:15.3	1	9	34.7	23.7	75	1118	56	6.7e+20	0.17	7.3e+08	405.6	7.7	541
70	10:29:19.3	68:24:53.8	89	9	61.5	45.0	202	2050	104	6.6e+20	0.17	4.5e+09	2451.0	7.0	3512
71	10:29:21.3	68:23:50.5	81	9	17.0	17.0	0	662	33	7e+20	0.18	1.5e+08	87.8	8.3	110
72	10:29:25.8	68:26:17.1	92	15	35.5	30.0	-73	1272	40	6.4e+20	0.16	1.1e+09	570.2	7.1	1325
73	10:29:37.0	68:27:27.9	99	9	21.5	21.5	0	838	42	7e+20	0.18	3.1e+08	176.9	8.4	229
74	10:29:32.3	68:28:37.4	112	9	18.0	18.0	0	701	35	7e+20	0.18	1.8e+08	103.9	8.2	131
77	10:28:15.1	68:21:04.0	27	9	24.9	24.9	0	970	49	6.8e+20	0.17	4.8e+08	269.3	6.3	354
78	10:28:31.7	68:28:29.1	74	7	24.0	24.0	0	935	59	7.1e+20	0.18	4.3e+08	251.6	5.9	258
79	10:28:59.2	68:31:09.8	81	9	60.8	42.7	-106	1987	101	6.5e+20	0.16	4.1e+09	2187.9	9.7	3116